DEVELOPMENT OF POLYMER DERIVED SIALCN CERAMIC AND ITS APPLICATIONS FOR HIGH-TEMPERATURE SENSORS

by

GANG SHAO

B.S. Zhengzhou University, China, 2006
M.S. Zhengzhou University, China, 2009

A dissertation submitted in partial fulfillment of the requirements
for the degree of Doctor of Philosophy
in the Department of Materials Science and Engineering
in the College of Engineering and Computer Science
at the University of Central Florida,
Orlando, Florida

Summer Term
2013

Major Professor: Linan An

ABSTRACT

Polymer-derived ceramic (PDC) is the name for a class of materials synthesized by thermal decomposition of polymeric precursors which excellent thermomechanical properties, such as high thermal stability, high oxidation/corrosion resistance and high temperature multifunctionalities. Direct polymer-to-ceramic processing routes of PDCs allow easier fabrication into various components/devices with complex shapes/structures. Due to these unique properties, PDCs are considered as promising candidates for making high-temperature sensors for harsh environment applications, including high temperatures, high stress, corrosive species and/or radiation.

The SiAlCN ceramics were synthesized using the liquid precursor of polysilazane (HTT1800) and aluminum-sec-tri-butoxide (ASB) as starting materials and dicumyl peroxide (DP) as thermal initiator. The as-received SiAlCN ceramics have very good thermal-mechanical properties and no detectable weight loss and large scale crystallization. Solid-state NMR indicates that SiAlCN ceramics have the SiN_4, SiO_4, $SiCN_3$, and AlN_5/AlN_6 units. Raman spectra reveals that SiAlCN ceramics contain “free carbon” phase with two specific Raman peaks of “D” band and “G” band at 1350 cm^{-1} and 1600 cm^{-1}, respectively. The “free carbon” becomes more and more ordered with increasing the pyrolysis temperature. EPR results show that the defects in SiAlCN ceramics are carbon-related with a g-factor of 2.0016 ± 0.0006. Meanwhile, the defect concentration decreases with increasing sintered temperature, which is consistent with the results obtained from Raman spectra.

Electric and dielectric properties of SiAlCN ceramics were characterized. The D.C. conductivity of SiAlCN ceramics increases with increasing sintered temperature and the activation energy is about 5.1 eV which higher than that of SiCN ceramics due to the presence of oxygen. The temperature dependent conductivity indicates that the conducting mechanism is a semiconducting band-gap model and follows the Arrhenius equation with two different sections of activation energy of 0.57 eVand 0.23 eV, respectively. The temperature dependent conductivity makes SiAlCN ceramics suit able for high temperature sensor applications. The dielectric properties were carried out by the Agilent 4298A LRC meter. The results reveal an increase in both dielectric constant and loss with increasing temperature (both pyrolysis and tested). Dielectric loss is dominated by the increasing of conductivity of SiAlCN ceramics at high sintered temperatures.

SiAlCN ceramic sensors were fabricated by using the micro-machining method. High temperature wire bonding issues were solved by the integrity embedded method (IEM). It's found that the micro-machining method is a promising and cost-effective way to fabricate PDC high temperature sensors. Moreover IEM is a good method to solve the high temperature wire bonding problems with clear bonding interface between the SiAlCN sensor head and Pt wires. The Wheatstone bridge circuit is well designed by considering the resistance relationship between the matching resistor and the SiAlCN sensor resistor. It was found that the maximum sensitivity can be achieved when the resistance of matching resistor is equal to that of the SiAlCN

sensor. The as-received SiAlCN ceramic sensor was tested up to 600 °C with the relative output voltage changing from -3.932 V to 1.153 V. The results indicate that the relationship between output voltage and test temperature is nonlinear. The tested sensor output voltage agrees well with the simulated results. The durability test was carried out at 510 °C for more than two hours. It was found that the output voltage remained constant for the first 30 min and then decreased gradually afterward by 0.02, 0.04 and 0.07 V for 1, 1.5 and 2 hours.

ACKNOWLEDGMENTS

I would like to express my great gratitude to my advisor, Professor Linan An, for his continuous encouragement and thoughtful guidance during my study at University of Central Florida.

I would like to thank Professor Lee Chow, Professor Jiyu Fang, Professor Chengying Xu, and Professor Weiwei Deng to contribute their time as my committee members and all the valuable advices.

I would like to express my thank to Dr. Nina Orlovskaya, Dr. Yi Liao, Dr. Chengying Xu, Dr. Lei Zhai, Dr. Zhongyang Chen for their help with the facilities and results analysis.

I would like to thank Dr. Likai Song, Dr. Zhehong Gan and Mr. Lu Yu for EPR and NMR test and analysis at National High Field Magentic Lab at Florida State University.

I would like to acknowledge to Ms. Lujiao Yang, Dr. Yaohan Chen, Dr. Hongyu Gong, Dr. Hongliang Xu, Dr. Wenge Li, Dr. Jianhua Zou, Ms. Xueping Yang, Mr. Jinling Liu, Mr. Renan Gongora, Mr. Zhilin Xie, Ms. Zhen Shi, Dr. Feng Gao, Mr. Douglas Freese, Mr. Anthony Spagnola for the help with my experiments and data analysis.

I would like to give my specific thank to my families, my wife, Jingjing Wang, my mother, Quanzhi Wang, my father, Yudong Shao, my sister, Xiuli Shao and my brother, Feng Shao, for their encouragement and support all the time.

TABLE OF CONTENTS

LIST OF FIGURES

LIST OF TABLES

LIST OF ACRONYMS/ABBREVIATIONS

ASB	Aluminum tri-sec-butoxide
CVD	Chemical vapor deposition
DP	Dicumyl peroxide
EELS	Electron Energy Loss Spectroscopy
FIB	Focused iron beam
IEM	Integrity embed method
MEMS	Micro-electro-mechanical systems
NMR	Nuclear magnetic resonance
PDC	Polymer Derived Ceramics
SAXS	Small Angle X-ray Scattering
SEM	Scanning electron microscopy
TEM	Transformation Electron Microscopic
TGA	Thermogravimetric analysis
XRD	X-ray diffraction

CHAPTER ONE: INTRODUCTION

1.1 Motivation

Temperatures must be monitored to prevent damage of devices and improve their performance in high temperature and harsh environments, such as gas turbines, nuclear reactors, high speed vehicles and automotives. Therefore, robust sensors are highly desired in the harsh environment of high temperature, high pressure, oxidation, radiation and corrosive species. Sensors that can be applied in these hostile applications must satisfy two features: firstly, the sensor materials must survive at these environments; secondly, the materials must maintain specific properties by means of sensoring. Most of the current available materials are excluded by these two requirements. Currently, several techniques are under development for such applications. However, present electronics technologies are limited to silicon-based technology, which has a limited operating temperature range of a few hundred degrees Celsius and is not suitable for high temperature sensing applications. Another possible option is using the refractory materials, such as silicon carbide and/or silicon nitride. However, these type of sensors are very restricted by limited fabrication methods, high cost, and a limited operation temperature range (typically < 800 °C), especially if the environment involves corrosive atmospheres as well.

Recently, polymer-derived ceramics (PDCs) have been considered as suitable materials for making high-temperature microelectromechanical systems

(MEMS)/micro-sensors, because PDCs exhibit excellent thermomechanical properties, such as high thermal stability, high oxidation/corrosion resistance and high temperature multifunctionalities. In addition, the direct polymer-to-ceramic processing route of PDCs makes it much easier to be fabricated into various components/devices with complex shapes/structures.

The overall objective of this dissertation is to develop a suitable micro-scaled temperature sensor which can fulfill the requirements of operating in high temperature and harsh environment for online, real-time temperature measuring and health monitoring.

1.2 Outline of dissertation

The dissertation is organized by the following parts:

Chapter 2 is the literature review of the background of polymer derived ceramics and their unique properties suitable for high temperature application. The fabrication and characterization of SiAlCN ceramics is discussed in Chapter 3. Chapter 4 focuses on the electric and dielectric properties of SiAlCN ceramics. Chapter 5 includes the SiAlCN ceramic sensor fabrication and characterization. Chapter 6 contains the general conclusions of this dissertation. Additionally, Appendix I and Appendix II illustrated the nanofabrication capability of SiAlCN ceramics by using focused iron beam (FIB) and the application of SiAlCN ceramics in forming carbon nanofiber reinforced ceramic nanocomposites.

CHAPTER TWO: LITERATURE REVIEW

This chapter is separated into two main sections (1) background information of polymer-derived ceramics (PDCs) and (2) high temperature sensors. The first part includes preceramic precursors, fabrication and processing techniques, microstructures and properties of PDCs. The second part discusses different high temperature sensors, materials/devices, including resistance temperature detectors, thermistors and PDCs sensors.

2.1 Polymer-derived ceramics

Polymer-derived ceramics (PDCs) are a class of materials synthesized by thermal decomposition of polymeric precursors. The basic processing of PDCs is illustrated in Figure 2.1, including the following steps: (i) synthesis of precursors from starting chemicals, (ii) crosslinkage of the precursor into an infusible preceramic network, and (iii) pyrolysis of the preceramic network into ceramics. PDCs provide advantages, such as, flexible fabrication capability, low sintering temperature and excellent oxidation and creep resistance compared to the traditional powder route ceramics. After pyrolysis, the ceramics are predominately amorphous and this structure can be retained even up to high temperatures. Further increasing temperature may lead to crystallization of the amorphous structure to form polycrystalline ceramics. The majority of researches on PDCs have been focused on amorphous state.

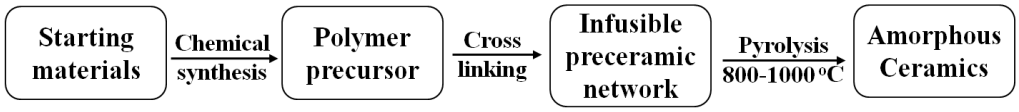

Figure 2.1 Basic fabrication processing of PDCs.

2.1.1 Polymeric precursors

PDCs have attracted great attention in these last few decades due to their promising high temperature harsh environment applications. Many types of PDCs have been discovered and can be classified into three main types, based on the number of the components in the system, (1) binary systems of SiC, and Si_3N_4, (2) ternary systems of SiCN, SiCO and BCN as well as (3) quaternary and multinary systems of SiAlCN, SiCNO, SiBCN and SiAlBCN, SiBCNO and so on.

One key issue for developing polymer-derived ceramics (PDCs) is to synthesize precursors, the starting material, to obtain PDCs. Composition, microstructure and the properties of PDCs are all influenced by the starting material used. In the 1960's, the first publications that use the fabrication of polymer-derived ceramics were reported by Ainger[1] and Chantrell[2]. After that several research groups worked on synthesis PDCs. However, PDCs were not fully recognized until Yajima[3] and Fritz[4] synthesized SiC and Si_3N_4 ceramic fibers, crucial in the fields of aerospace, military and energy propulsion.

Organosilicon polymers are the most widely used stating materials due to their well know chemistry, reaction-controlled thermolysis and polymerized function sites including the following functional groups: Si-H, Si-Cl, Si-C=C. The synthesis of preceramic percursors are commonly utilizes chlorosilanes $RxSiCl_{4-x}$ (x=0-3) for use

as starting materials. Normally through two kinds of methods of ammonolysis reactions with ammonia or aminolysis with different amines[5] we can obtain the desired chlorosilane, as illustrated in Figure 2.2. Various types of precursors were synthesized by using silicon-based polymers, such as, polysilanes, polysilazanes, polysiloxanes, polycarbosilanes, polyborosilazanes and polyaluminasilazanes.

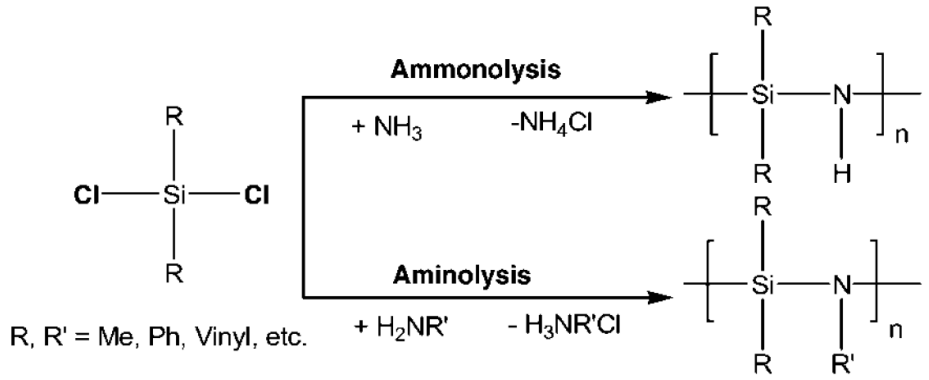

Figure 2.2 Synthesis methods for polycarbosilazanes by using chlorosilanes as starting materials[5].

Most recently, Colombo and his co-workers summarized a simplified general formula of Si-based precursor as shown in Figure 2.3[6]. As we can see there are two important parameters of this general formula: the backbone group X and the functional group R^1 and R^2. The type of Si-based polymeric precursor is determined by the backbone group X, for example, if X = Si then we obtain poly(organosilanes); if X = O then we obtain poly(organosiloxanes); if X = B then we obtain poly (organoborosilazanes); if X = CH_2 then we obtain poly(organocarosilanes) and if X= NH then we obtain poly(organosilazanes). More and more combinations are illustrated in Figure 2.4[6]. The functional group R^1 and R^2 (either hydrogen, aliphatic or aromatic side groups) are highly related to composition, microstructure and

properties of the final ceramic products. For instance, variation of each R group from hydrogen, aliphatic and aromatic groups will directly manipulate composition, microstructure, thermal and chemical stability, electric and dielectric properties, as well as the solubility and rheological properties of the ceramic.

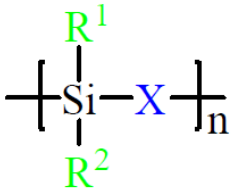

Figure 2.3 Simplified general formula of the molecular structure of the Si-based preceramic precursors[6].

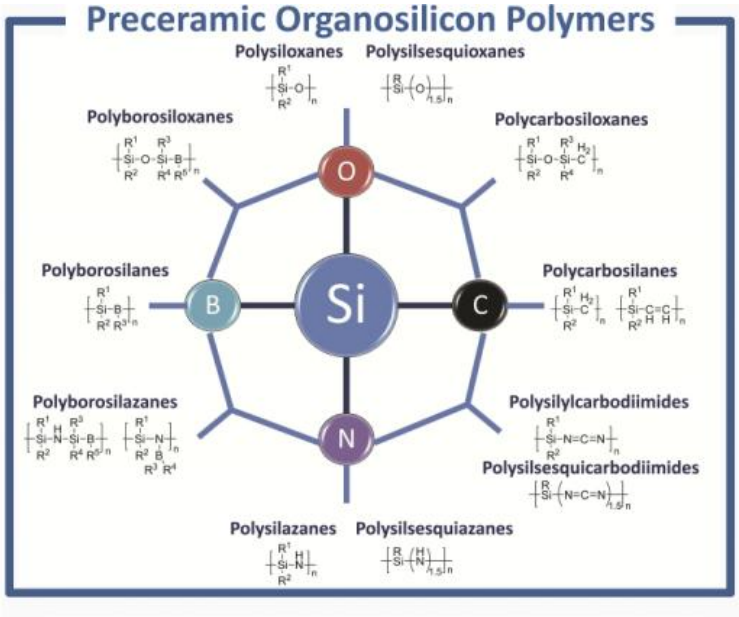

Figure 2.4 Main classes of preceramic polymer precursors for the fabrication of Si-based PDCs[6].

Among the huge amount of polymer precursors, the synthsis of SiAlCN precursor will be discussed only here for the research purpose of this dissertation.

Polymer derived SiAlCN ceramics are considered to be promising candidates for high temperature and harsh environment applications due to excellent thermal-mechanical properties of this sort of material, such as high oxidation and corrosion

resistance, high temperature stability and multifunctionality. Several SiAlCN precursors were reported such as, $\{[(Me_3Si)_2N]_2AlNH_2\}_2$[7], $(Et_2AlNH_2)_3$[8], $(CH_3)_2AlNH_2$[9] and $(Al(OCH(CH_3)_2)_3$[10]. The high yield SiAlCN precursor was synthesized by reacting the polysilazane $[CH_3HNH]_n$ either with $(CH_3)_3Al$ or $(CH_3)_2AlNH_2$ reported by Seyferth and co-workers[9] as shown in Figure 2.5. With respect to synthesis, they also found that the $(CH_3)_2AlNH_2$ is a better choice than $(CH_3)_3Al$ due to the lower alkylating activity and presence of crosslinkable Al-NH_2 groups. Berger[11] prepared polyaluminasilazanes from polysilazanes and polysilylcarbodiimides by means of hydroalumination of vinyl substituents at Si and subsequent dehydrocoupling of N-H reactive sites, as demonstrated in Figure 2.6. The detailed polymer-to-ceramic evolution during the pyrolysis was investigated by Dhamne and co-workers[12].

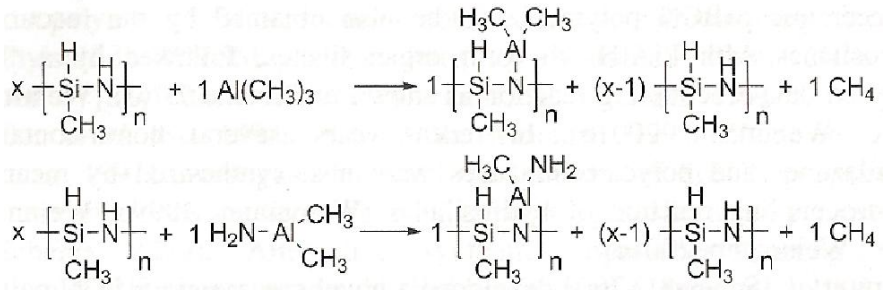

Figure 2.5 Synthesis routes of polyaluminasilazanes starting from $(CH_3)_3Al$ and $(CH_3)_2AlNH_2$[11].

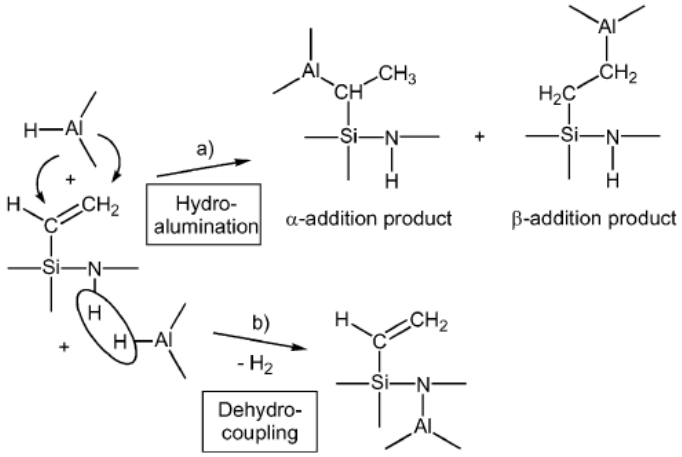

Figure 2.6 Synthesis of polyaluminasilazanes by means of hydroalumination and dehydrocoupling reactions[12].

2.1.2 Fabrication capability of polymer-derived ceramics

One unique advantage of PDCs is its flexible processing capability for making ceramic components/devices with complex and inconvenient shapes due to the intermediate state of the liquid polymer, which the traditional ceramic-powder route cannot. A variety of ceramic component/devices, such as high-temperature ceramic fibers, ceramic matrix composites, micro-electro-mechanical systems (MEMS) and micro-sensors, have been fabricated by using PDC processing. These components/devices are particularly important for applications in harsh environments with high temperature and corrosion.

The as-synthesized liquid polymeric precursor can be easily shaped into various complex structures/components. These shaping techniques could be casting (micro/nano casting[13-15], tape casting[16] and freeze casting[17]), machining[18], lithography (soft lithography[19-21] and microstereolithography[22]), coating (spraying coating[23], dip coating[24,25], spin coating[26] and chemical vapor deposition[27]), fiber drawing[28,29] and

direct writing[30] as well as fabrication of composites[31-33]. A schematic drawing of the fabrication techniques was included in Figure 2.7.

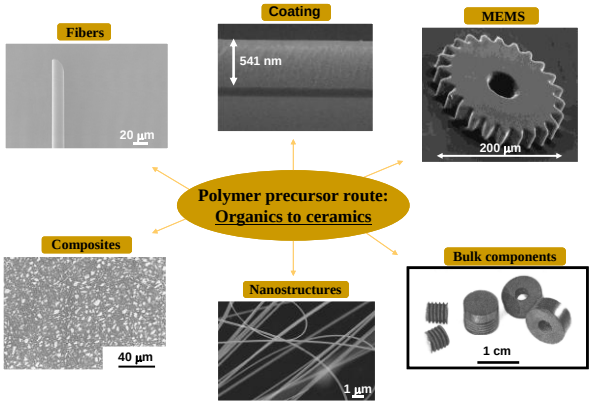

Figure 2.7 Fabrication methods of polymer-derived ceramics.

Pham and co-workers[34] fabricated 3-D SiCN ceramic nanostructures with a resolution of 210nm, and found the addition of Si-nanoparticle fillers may greatly reduce shrinkage to get integrated features as shown in Figure 2.8.

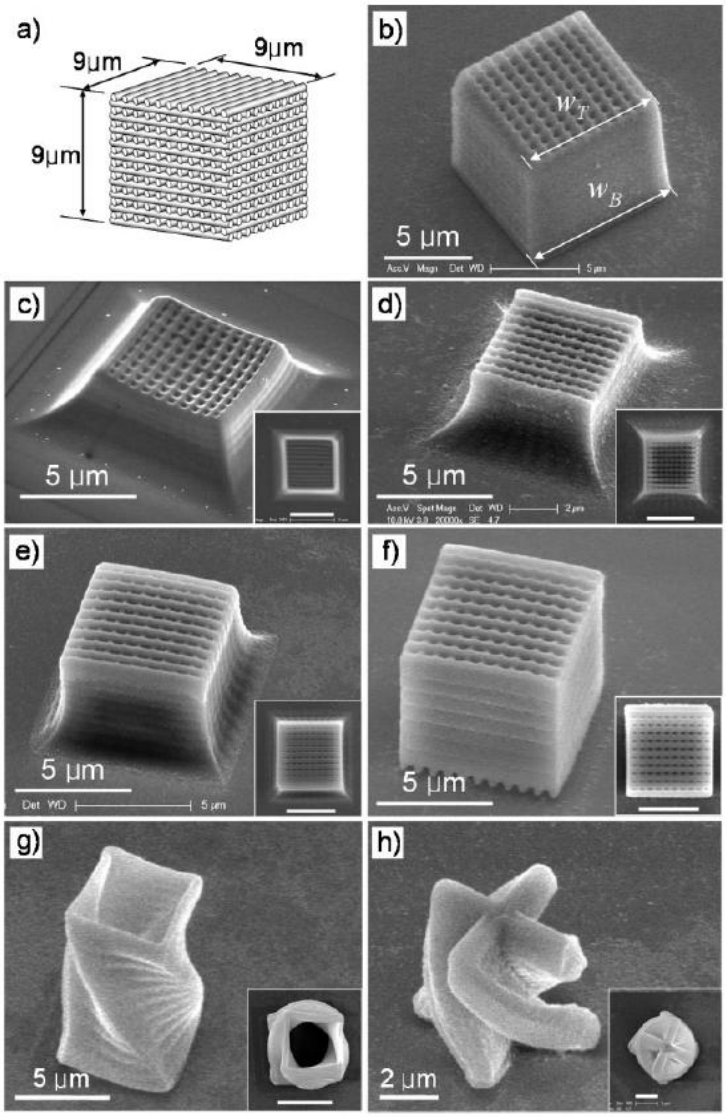

Figure 2.8 3-D SiCN ceramic microstructures fabricated by nanostereolithography; (a) schematically designed woodpile structure (b) polymeric structure without filler (c) ceramic structure without filler & (d) ceramic structure with 20 wt% Si filler (e) ceramic structure with 30 wt% Si filler (f) ceramic structure with 40 wt% Si filler, and other 3-D microstructrues with 40wt% Si filler, (g) micro tube (h) microcruciform. (Each inset is the top-view of the structure) [34].

The flexibility of fabrication of micro-electro-mechanical systems (MEMS) and micro sensor/actuator/transducer of PDCs has allowed increased investigations by other research groups. Liew and co-workers [15,35-38] at the University of Colorado at Boulder USA, fabricated a series of SiCON MEMS devices by using preceramic

polymers and photolithography methods. They prepared a vertical electrostatic actuator which consisted a four-flexured SiCN structure mounted onto a alumina substrate with metal pads and wiring shown in Figure 2.9. The thickness of SiCN was 40 μm and suspended 3μm above the electrode and a deflection of 370nm was detected coresponding to the input voltage of 200V.

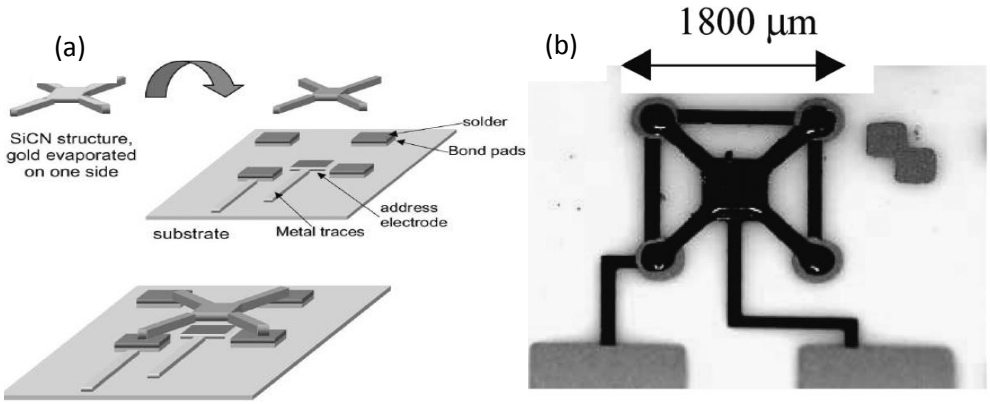

Figure 2.9 SiCN electrostatic actuator; (a) schematic drawn (b) assembled on a alumina substrate[15].

2.1.3 Microstructure of polymer-derived ceramics

Amorphous PDCs possess very complex structures different from conventional crystalline and amorphous structures. While the exactly structures of PDCs are not known very well which depends on the composition of the precursor, pyrolysis conditions and annealing temperatures. As stated earlier, PDCs are composed of an amorphous matrix made of SiC_xN_{4-x} (x can be 0, 1, 2, 3 and 4) units and free carbon phase which forms nano-sized clusters. In addition, the materials contain a fairly large amount of carbon dangling bonds, which are either in the matrix or on the surface of the carbon nanoclusters. The schematic structure model of PDCs

is illustrated in Figure2.10. Two distinguished characteristics of PDC materials are the (1) free carbon nanocluster and (2) dangling carbon bonds and both are key factors for determining their properties. A better understating of the structure-relationship of PDCs is required not only to generate new fundamental knowledge, but also to lead to potential widespread applications of the material.

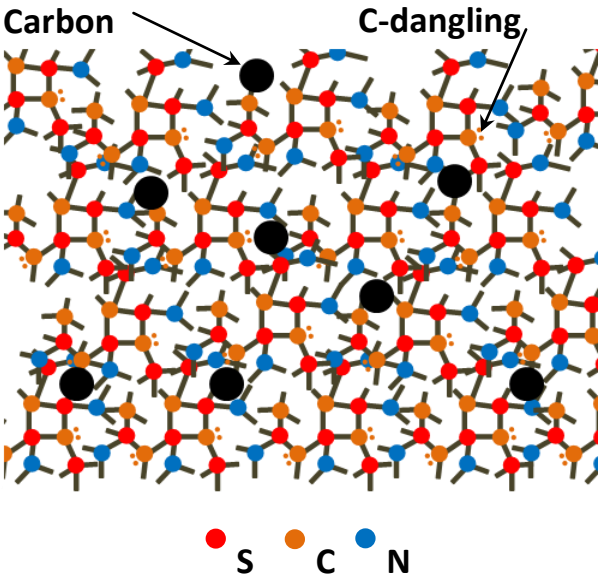

Figure 2.10 Schematic structure model of PDCs.

Several characterization technologies have been implemented in the study of microstructure and structural evolution of PDCs. Such instrumental methods include, Magic Angle Spin-Nuclear Magnetic Resonance (MAS-NMR)[39,40], Small Angle X-ray Scattering(SAXS)[41,42], Fourier Transform Infrared Spectroscopy (FT-IR) [40], X-ray Diffraction (XRD)[43] and Raman Spectroscopy[44] for internal information characterization; Transformation Electron Microscopic (TEM)[45], and Electron Energy Loss Spectroscopy (EELS)[46] for local information characterization.

As mentioned above, the microstructure of PDCs includes two main parts, the amorphous matrix and free carbon cluster, therefore, the structural characterization and evolution of PDCs will be discussed in this section with respect to these two parts.

Raman spectroscopy is a powerful and nondestructive tool for the initial examination of carbon materials. As of today, the Raman spectroscopy is widely used to characterization the structure evolution of free carbon in PDCs[47-50]. Two major Raman peaks of free carbon are observed in PDCs; the first peak corresponding to the D bond at approximately 1350 cm^{-1} and the second peak corresponding to the G bond at approximately 1582 cm^{-1} as well as the D'- and G' bonds located at ~ 1620 cm^{-1} and 2700 cm^{-1}, respectively[50]. The G bond is caused by in-plane bond stretching of sp^2 carbon, which is very important for the electric properties of PDC. Another important parameter that needs to be considered is the intensity ratio between D bond and G bond (I_D/I_G). This ratio can be used to calculate the free carbon cluster size.

Due to the crucial role that free carbon plays in the determination of the properties of PDCs quantitative measurement must be done in order to reveal the concentration of free carbon. This quantitative analysis of free carbon content in SiCN system can be revealed by Raman spectroscopy reported by Jiang and co-workers[44]. They used silicon powder as an external reference, as shown in Figure 2.11 (a). A linear relationship between the volume ratio of silicon powder, SiCN powder (V_{Si}/V_{SiCN}) and normalized intensity ratio of (I_{Si}/I_{CK}) was found. Therefore, the free carbon concentration was achieved as the slope of the plot of V_{Si}/V_{SiCN} versus $I_{Si}/I_{CK,}$

as shown in Figure 2.11 (b).

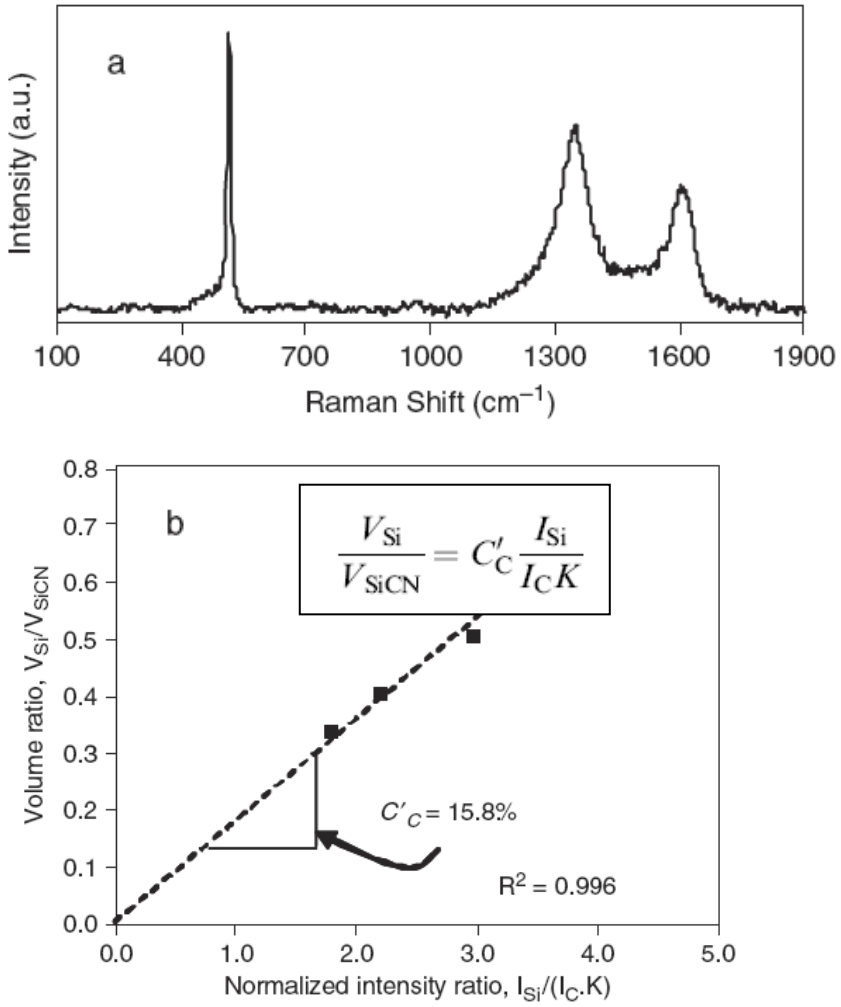

Figure 2.11 Raman spectroscopy of Si-SiCN mixture with the volume ratio of 1:1 (a). (b) Plot of V_{Si}/V_{SiCN} as a function of normalized I_{Si}/I_{CK}[44].

Another important technique for investigating the structure of PDCs is multinuclear magic angle spin-nuclear magnetic resonance (MAS-NMR), one of the most accurate and useful methods to explore bonding conditions (the coordination of elements) of PDCs[39,40,51,52]. Seitz[39] et al. investigated the structure of polysilazane (NCP 200) and polyvinylsilazane (VT 50) by solid state NMR. It was observed that NCP 200 contained mixed Si sites of SiN_4, $SiCN_3$, SiC_2N_2 but only SiN_4 for VT 50 and ^{13}C NMR revealed that sp^2 amount in VT 50 was much higher than that of NCP

200. Widgeon[52] and colleges used high-resolution NMR to reveal the structure of SiCO-PDC which consisted of a SiCxO4-x network and a sp^2 hybrid free carbon nanodomain. At the same time, the oxygen-rich SiCxO4-x units were expected to be more concentrated in the interior of this network while the carbon-rich units were expected to be localized at the interface of free carbon nanodomains.

Electron paramagnetic resonance (EPR) is yet another widely used technique to characterize the structure of PDC. EPR was used to determine the type of defects and their concentration in PDCs[40,53-55]. Sergey[54] and co-workers found that the EPR signals of SiCN ceramics corresponded to dangling sp^2 hybridized carbon within the temperature range of 4 to 300K with g factor of 2.0027. Decreasing line width was noticed with increasing pyrolysis temperature. Yee[55] et al. characterized the SiBN and SiBCN system using EPR spectrum and revealed that the EPR signals of SiBN were very weak and in contrast, that of SiBCN were much stronger. They believed that because the later one introduced carbon in the network. The trend of intensity of EPR according to pyrolysis temperatures varied case by case due to precursor differences[53,55].

2.1.4 Properties of polymer-derived ceramics

Numerous publications reported about different properties of PDCs, such as mechanical properties[56-59], electric properties[60-62], thermal-mechanical properties[63-66], optical[67,68] and magnetic properties[69,70]. In this section, only the thermal-mechanical,

electric and dielectric properties will be discussed for high temperature sensor applications.

2.1.4.1 Thermal-mechanical properties of PDCs

PDCs possess excellent thermal-mechanical properties of high oxidation/corrosion resistance, high temperature stability, high creep resistance. These excellent high temperature properties make PDCs promising candidates for the high temperature harsh environment applications. Ralf[71] and co-workers developed a SiBCN ceramic with very high temperature stability. They did not find any serious thermal decomposition up to 2000^{o}C which high than that of SiCN and Si_3N_4 ceramics and suggested application exceed to 1500^{o}C, as shown in Figure 2.12. The materials did not show large-scale crystallization up to 1600-1700^{o}C. Long time durability is another important feature for high temperature applications. The high temperature experiment had been carried out on polymer derived ceramics[72-74] and the results revealed that the SiBCN ceramics had a negligible strain rate at the temperature as high as 1500^{o}C (Figure 2.13).

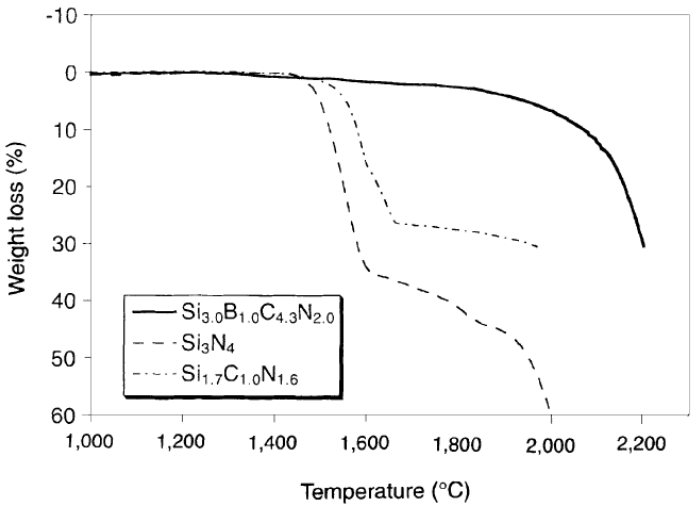

Figure 2.12 Thermal gravimetric analysis (TGA) of polymer-derived SiCN, SiBCN and silicon nitride[71].

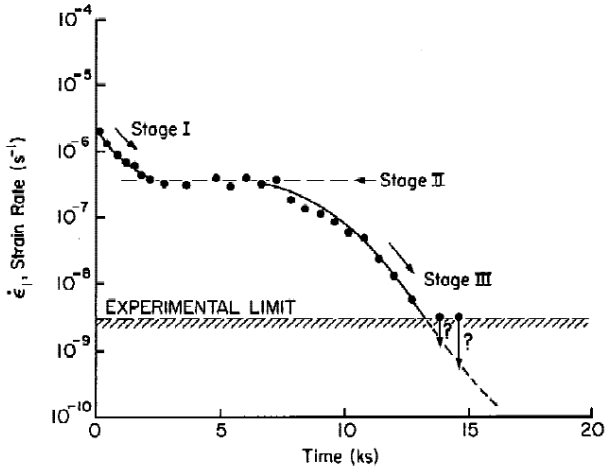

Figure 2.13 Changes in the strain rate of SiBCN ceramic with time in three stage. At 1500°C and 75MPa[72].

Oxidation/corrosion resistance is one of the critical parameters to determine the ability of harsh environment application. Bahloul and Delverdier worked on the oxidation behavior of SiCN and SiCO system at 1992 and 1993, respectively which were considered as primary research on the oxidation topic of PDC[75,76]. Each of their results suggests that the oxidation rate of these PDCs were close to or a little bit higher than that of SiC and Si_3N_4[63,77,78]. Similar results were observed by recent

researchers[64,79] and even for the B-doped PDC[80]. Most recently, Wang and An revealed that the Al-doped SiCN ceramics had a higher oxidation resistance than that of the above mentioned ceramics[66,81-85]. They found that the oxidation thickness of SiAlCN was much smaller than that of SiCN at the same oxidation time with the tested temperature of 1200^{o}C. And after 100 hours the oxidation thickness of SiAlCN tended to achieve steady state, in contrast, that of SiCN kept increasing, as shown in Figure 1.14. It was reported that SiAlCN ceramics had excellent corrosion resistance than SiCN ceramics which were comparable with SiC and Si_3N_4[83], as illustrated of the SEM images in Figure 2.15. The properties of polymer derived ceramics and other high-temperature materials are compared in Table 2.1. It shows that polymer derived ceramics have much better oxidation resistance than others. The oxidation/corrosion is one of the most important problems to limit the high temperature applications of materials. Due to the high oxidation/corrosion resistant of SiAlCN ceramics, they are good candidates for high temperature and harsh environment applications.

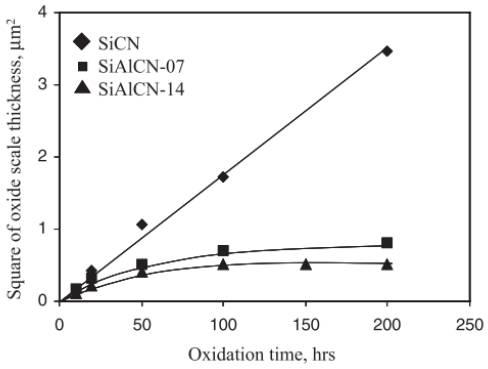

Figure 2.14 A plot of the square of the oxide scale thickness as a function of annealing time for both SiCN and SiAlCN at 1200°C in dry air.[42]

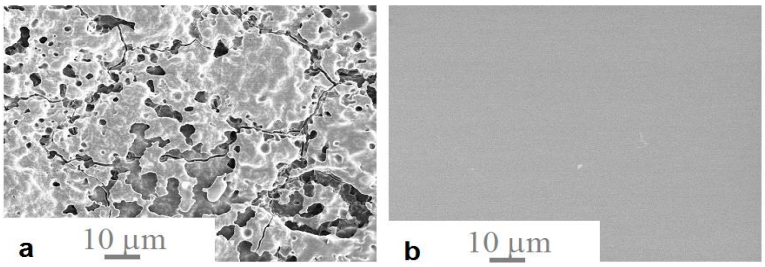

Figure 2.15 SEM micrograph of the surface of (a) SiCN, (b) SiAlCN at 1400°C for 300h in 50%H_2O-50%O_2 environment[83].

Table 2.1 Properties of polymer derived SiCN and other high-temperature materials.

	SiCN	SiC	Si_3N_4
Density (g/cm^3) (annealed @ 1000°C)	2.2	3.17	3.19
Young's modulus (GPa)	92	400	320
Poisson's ratio	0.18	0.14	0.24
CTE ($\times10^6$/K)	3	3.8	2.5
Strength (MPa)	~500-1000	~400	~700
Hardness (GPa)	15-20	30	28
Fracture toughness (MPa·m$^{1/2}$)	2-3.5	4-6	5-8
Thermal shock FOM*	1800-3600	350	880
Oxidation rate ($\times10^{-18}$m^2/s, @ 1400°C)	0.47	16.4[77#]	6.2[78#]
Corrosion rate ($\times10^{-6}$g/cm^{2}hr, @ 1400°C in water vapor)	0.98	6.4[86#]	6.2[18#]

* Thermal shock FOM = strength/(E.CTE)

\# The lowest values reported for SiC and Si_3N_4 tested at the same conditions.

2.1.4.2 Electric properties of PDCs

Previous studies have shown that polymer derived ceramics are one kind of amorphous semiconductors and their electric conductivities can be tailored within a large range up to 15 orders of magnitude (typically from ~10^{-10} to ~1 (ohm*cm)$^{-1}$) by varying the polymeric precursor, pyrolysis temperature and atmosphere as well as the annealing temperature and time[36,60,87-90]. For example, PDCs behave more like a

insulator at low pyrolysis temperature < 600°C, and semiconductor at middle temperatures < 1200~1400°C, when goes to high sintered temperature > 1400°C， they are can be described as metal semiconductors. Researchers also found that free carbon plays an important role to determine the electric properties of PDCs[47,89]. The free carbon will form a continuous network and contribute the overall conductivity of the PDCs when increasing the pyrolysis temperature. However, these formation temperatures were altered case by case. Take the case shows in Figure 2.16 for example[91], the free carbon formed continuous network at 800°C for polysiloxanzes $[RSiO_{1.5}]_n$ with R=C_6H_5 (PPS) and 1400°C for R-CH_3 (PMS).

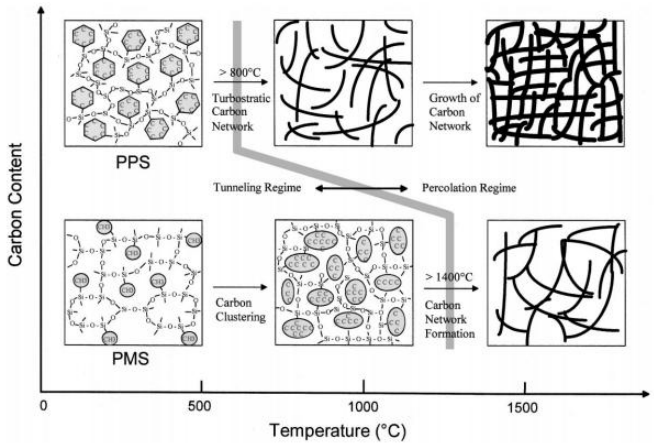

Figure 2.16 Model of carbon redistribution and continuous network formation of PPS and PMS[91].

The influence of pyrolysis temperature of the electric conductivity of PDC was studied by Haluschka and colleges[60]. They found the electric conductivity evolution of SiCN ceramics could be classified into three temperature regimes, demonstrated in Figure 2.17. First, the increase of conductivity of SiCN ceramics from 1000-1300°C due to an enhanced sp^2/sp^3 ratio of loss of residual hydrogen of carbon atoms; second, the increase of conductivity of SiCN caused by the formation of SiC and loss of

nitrogen of amorphous matrix between 1300 and 1600°C; third, the electric conductivity was contributed by nitrogen doped SiC.

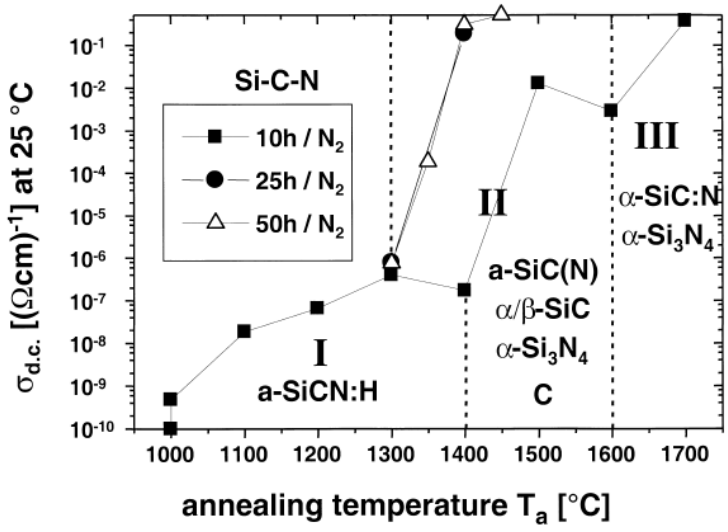

Figure 2.17 Electric conductivity of SiCN ceramic depending on the annealing temperature and time[60].

Researchers tested the temperature dependence conductivity properties in order to understand the conduction mechanism of amorphous PDCs [60,88,92]. The mechanisms were found and is probable that three dimension variable range hopping (Mott's law) with a linear relationship between the conductivity of $T^{1/4}$ (Equation 2.1, T is testing temperature), band-gap semiconducting mechanism which follows Arrhenius law with a linear relationship of conductivity and inverse test temperature (Equation 2.2) as well as the band tail hopping mechanism. Most recently, Ryu and colleges[93] found the semiconducting behavior of SiCNO ceramics are able to sustain temperatures up to 1300°C which is the highest one among all reported ceramic materials. The conducting mechanism of these materials was variable range hopping and the electric conductivity was highly depending on the O/N ratio, as shown in Figure 2.18 and Figure 2.19.

$$\sigma = \sigma_0 \exp\left[-\left(\frac{T_0}{T}\right)^{1/4}\right] \qquad \text{Eq. (2-1)}$$

$$\sigma = \sigma_0 \exp\left[-\frac{\Delta E}{kT}\right] \qquad \text{Eq. (2-2)}$$

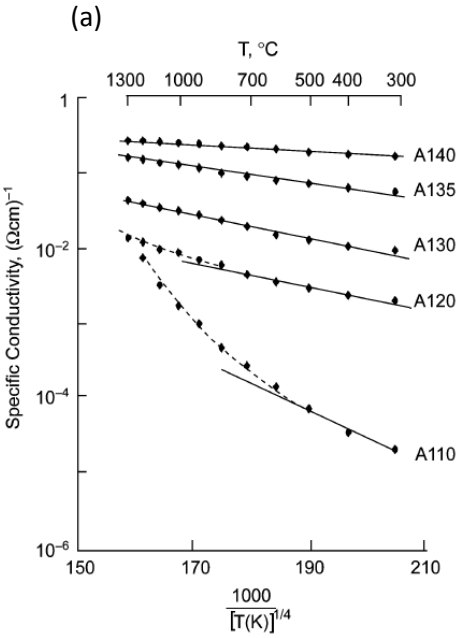

Figure 2.18 Temperature dependent conductivity of SiCNO ceramic up to 1300°C[93].

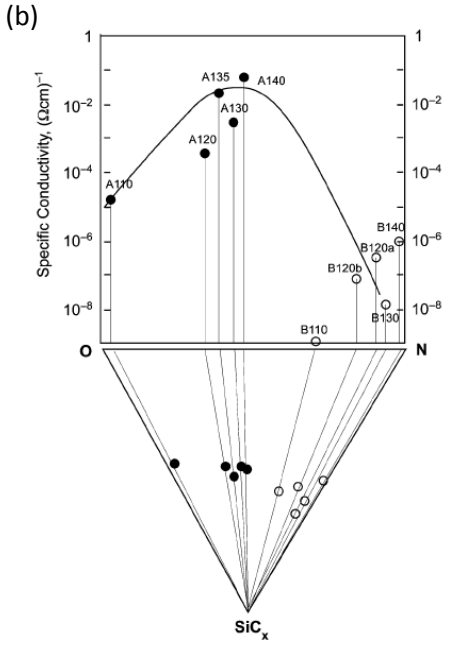

Figure 2.19 Electric conductivity of SiCNO ceramic varied with O/N ratio at room temperature[93].

Currently, Zhang et al. discovered a super high piezoresistivity effect of SiCN ceramic with a gauge factor as high as 1000~4000[94] which is much higher than that of any existing ceramics (Figure 2.20 (a)). The mechanism was due to the formation of tunneling percolation effect of free carbon as shown in Figure 2.20 (b)[95].

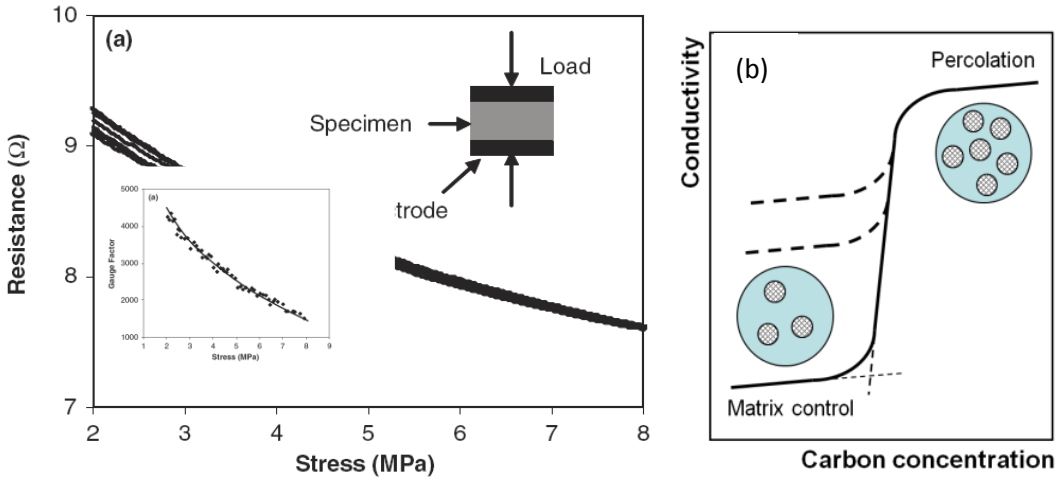

Figure 2.20 The piezoresistive effect of SiCN ceramics (a) resistance change versus test pressures (b) schematic drawing of conduction mechanism [95]. Insert figure is the plot of guager factor versus tested pressure.

2.1.4.3 Dielectric properties of PDCs

A brief summary of the background of dielectric theory will first be addressed because it is not as mature as classical theories of electricity and mechanics.

Dielectrics are a class of materials that can respond to an external electric stimulation with a polarization and have been widely used in industries as capacitors, resonators and energy storage devices. The polarization **P** is proportional to the electric field **E**.

$$P = \chi \varepsilon_0 E \qquad \text{Eq. (2-3)}$$

where χ is a constant, named dielectric susceptibility and ε_o is the dielectric constant in vacuum (8.85×10^{-12} F/m).

The dielectric constant is a measure of the polarization capability of a material. The definition of complex dielectric constant is

$$\varepsilon^{*} = \varepsilon_r - \mathrm{j}\varepsilon_r^{'} \qquad \text{Eq.(2-4)}$$

where j is the image unit; ε_r and ε' are the real part and image part of the dielectric constant, respectively. Meanwhile, the dielectric loss is defined as

$$\tan\delta = \frac{\varepsilon_r^{'}}{\varepsilon_r} \qquad \text{Eq. (2-5)}$$

where δ is loss angle.

Polarization is one of the most important parameters to understand in dielectrics. Generally, there are five polarization mechanisms for a dielectric material, as shown in Figure2.21[96].

1) Electronic polarization: electric field induced displacement of the outer electron cloud with respect to the inner positive nuclei. The response time is usually ~10^{-14}-10^{-16} s.
2) Atomic or ionic polarization: The distance between the positive charged atoms and negative charged atoms can be changed by an electric field. The response time is ~10^{-12}-10^{-13}s.
3) Orientational polarization: If there are dipoles in a material, the electric field generates a torque on each dipole, which causes dipoles aligned along the electric field direction. The response time is ~10^{0}-10^{-9}s (which highly dependents on temperature).

4) Hopping polarization: localized charges (ions and vacancies, or electrons and holes) can hop from one site to the neighboring site under an electric field. The response time is ~10^{-2}-10^{-5} s (which highly dependents on temperature).

5) Space charge polarization: The mobile or trapped charges (positive and negative charged) can be separated by an electric field. The response time is ~10^{2}-10^{-1}s. (highly dependents on temperature).

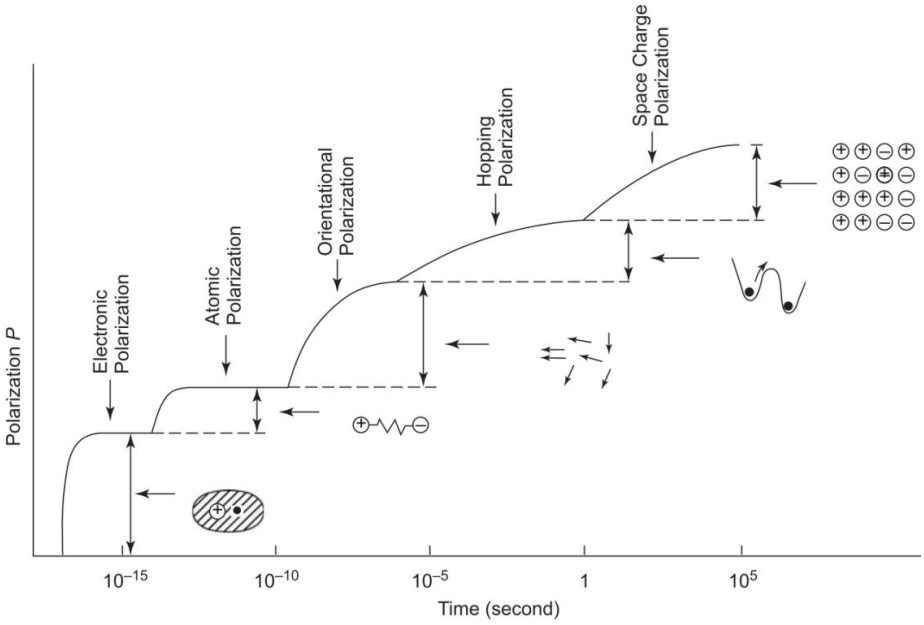

Figure 2.21 Polarization mechanisms in dielectric materials[96].

The Debye theroy is the most well-known and useful theroy for understanding dielectric phenoment of materials. The Debye equation is described as following and the schematic drawn is illustrited in Figure 2.22.

$$\varepsilon^{*} = \varepsilon_r - \mathrm{j}\varepsilon_r^{'} = \varepsilon_{r\infty} + \frac{\varepsilon_{rs}}{1+\mathrm{j}\omega\tau_0} \qquad \text{Eq. (2-6) (1)}$$

$$\varepsilon_r = \varepsilon_{r\infty} + \frac{\varepsilon_{rs}+\varepsilon_{r\infty}}{1+\mathrm{j}\omega^2\tau_0^2} \qquad \text{Eq. (2-6) (2)}$$

$$\varepsilon_r^{'} = \frac{\left(\varepsilon_{rs} - \varepsilon_{r\infty}\right)\omega\tau_0}{1 + \mathrm{j}\omega^2\tau_0^2} \qquad \text{Eq. (2-6) (3)}$$

And

$$\tan\delta = \frac{\varepsilon_r^{'}}{\varepsilon_r} = \frac{\left(\varepsilon_{rs} - \varepsilon_{r\infty}\right)\omega\tau_0}{\varepsilon_{rs} + \varepsilon_{r\infty}\omega^2\tau_0^2} \qquad \text{Eq. (2-7)}$$

Where ε_{rs} is the static dielectric constant, $\varepsilon_{r\infty}$ the dielectric constant at high frequency limit, ω is the angle frequency $\omega=2\pi f$, τ_o is the relaxation time.

By considering the real part ε_r and image part ε_r' without $\omega\tau_o$, we obtain:

$$\left(\varepsilon_r - \frac{\varepsilon_{rs} + \varepsilon_{r\infty}}{2}\right)^2 + \varepsilon_r^{'2} = \left(\frac{\varepsilon_{rs} - \varepsilon_{r\infty}}{2}\right)^2 \qquad \text{Eq. (2-8)}$$

The relationship between ε_r and ε_r' is shown in Figure 2.23 and the maximum value of ε_r' is reached at $\omega\tau_o=1$.

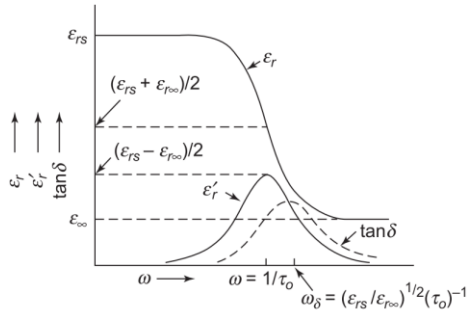

Figure 2.22 ε_r, ε_r' and tanδ as a function of ω for cases with negligible contribution of s due to carrier migration[96].

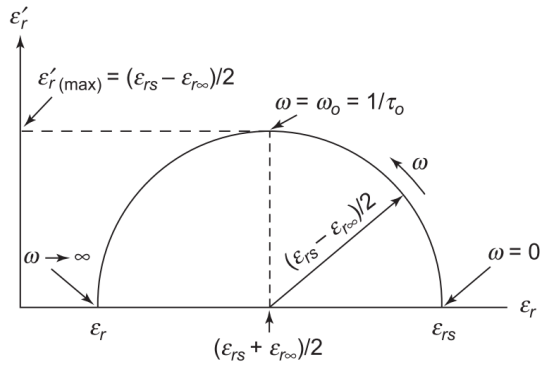

Figure 2.23 Schematic diagram of ε_r-ε_r' relation for cases with only one relaxation time τ_o[96].

The state of art of dielectric properties of polymer derived ceramics.

The studies of dielectric properties of PDCs are very limited. Jiang[97] characterized the dielectric constant and loss of SiCN ceramics and found that the SiCN owned a very high dielectric constant and loss due to the high defect concentration and free carbon content. Similar results were also found by Yu[98] and Li[99] in SiCTi and SiBCN system, respectively. Recently, Ren and colleges[100,101] used a dielectric resonator cavity method measured the dielectric properties of SiBCN ceramic at microwave frequency and high temperature. The dielectric constant and loss increased with increasing test temperature.

Due to the unique properties of flexible near net sharp fabrication capability, high oxidation/corrosion resistance, high temperature stability and multifunction properties, polymer derived ceramics are considered promising candidates for high temperature and harsh environment applications.

2.2 Background of high temperature sensors

Turbine engines can be found in power generation systems, aerospace propulsion, and automotives and are important to the functionality of such systems. The working condition of turbine engine system is very hostile include high temperatures (500-1400°C), high pressures (200-600 psi), and corrosive environments (oxidizing conditions, gaseous alkali, and water vapors). Online, real-time temperature and pressure monitoring of the inert environment of turbine engines can further improve the performance and reliability, reduce the pollution and improve the turbine engines design. Robust sensors are highly desired to measure and monitor the temperature and pressure in these harsh environments. However, fabrication of such sensors presents a huge technical challenge. The major hurdle is that the sensors must survive harsh environments, including high temperatures, high stress, corrosive species and/or radiation. In addition, the sensor materials must maintain specific properties at high temperatures in order to provide means for sensing; and they must do so in an easy-to-microfabricate way in order to lower costs.

Currently, several techniques are under development for such applications. High temperature metal based resistance temperature detector (RTD), such as Pt. This kind of sensor is very expensive and plagued with problems of self heating, long response time and bad oxidation/corrosion resistance as well as limited working temperature $<550^{o}C$ for most applications. Optical-based non-contact technology is a popular method in determining these parameters. However, it has been shown to lack

the necessary accuracy for good measurement and typically break down over time[102,103]. Another promising technique to measure these parameters without disturbing the work environment is using miniature sensors. Silicon carbide (SiC) and silicon nitride (Si_3N_4)-based ceramic microsensors are being investigated for high-temperature and harsh environment applications[104-108]. However, these sensors are very restricted by limited fabrication methods, high cost, and a limited operation temperature range (typically < 800^oC).

Most recently, polymer derived ceramics have attracted a great deal of attention for making high temperature sensors due to their excellent high temperature properties. Leo and colleges[109] proposed a hybrid SiCN high temperature pressure sensor by embedding piezoresistive chromium strain gauge between two thin SiCN membranes. Seo and co-workers[110] demonstrated a fabrication method of PDCs thin films for high temperature heat flux sensor application. However, these "PDC sensors" are all at a early stages of development and are currently at the conceptual level; no real sensors have been fabricated and characterized at the current moment.

References:

1. Herbert, F. W. A. a. J. M. 168-182 (Academic press, New York, 1960).
2. Popper, P. G. C. a. P. (ed P. Popper) 87-103 (Academic Press, New York, 1965).
3. Yajima, S., Hasegawa, Y., Okamura, K. & Matsuzawa, T. Development of high tensile strength silicon carbide fibre using an organosilicon polymer precursor. Nature **273**, 525-527 (1978).
4. Fritz, G. & Raabe, B. Bildung siliciumorganischer Verbindungen. V. Die Thermische Zersetzung von Si(CH3)4 und Si(C2H5)4. Zeitschrift für anorganische und allgemeine Chemie **286**, 149-167 (1956).
5. Seyferth, D. a. W., G. H. 354 (Wiley Interscience. New York, 1986).
6. Colombo, P., Mera, G., Riedel, R. & Soraru, G. D. Polymer-Derived Ceramics: 40 Years of Research and Innovation in Advanced Ceramics. Journal of the American Ceramic Society **93**, 1805-1837 (2010).
7. Paciorek, K. J. L. et al. Reactions of tris[bis(trimethylsilyl)amino]aluminum with ammonia and pyrolysis studies. Chemistry of Materials **3**, 82-87 (1991).
8. Czekaj, C. L. et al. Preparation of Silicon Carbide/Aluminum Nitride Ceramics Using Organometallic Precursors. Journal of the American Ceramic Society **73**, 352-357 (1990).
9. Boury, B. & Seyferth, D. Preparation of Si/C/Al/N ceramics by pyrolysis of polyaluminasilazanes. Applied Organometallic Chemistry **13**, 431-440 (1999).

10. Dhamne, A. et al. Polymer-ceramic conversion of liquid polyaluminasilazanes for SiAlCN ceramics. Journal of the American Ceramic Society **88**, 2415-2419 (2005).

11. Berger, F., Weinmann, M., Aldinger, F. & Muller, K. Solid-state NMR studies of the preparation of Si-Al-C-N ceramics from aluminum-modified polysilazanes and polysilylcarbodiimides. Chemistry of Materials **16**, 919-929 (2004).

12. Dhamne, A. et al. Polymer–Ceramic Conversion of Liquid Polyaluminasilazanes for SiAlCN Ceramics. Journal of the American Ceramic Society **88**, 2415-2419 (2005).

13. Melcher, R., Cromme, P., Scheffler, M. & Greil, P. Centrifugal Casting of Thin-Walled Ceramic Tubes from Preceramic Polymers. Journal of the American Ceramic Society **86**, 1211-1213 (2003).

14. Liu, X., Li, Y.-L. & Hou, F. Fabrication of SiOC Ceramic Microparts and Patterned Structures from Polysiloxanes via Liquid Cast and Pyrolysis. Journal of the American Ceramic Society **92**, 49-53 (2009).

15. Liu, Y. et al. Application of microforging to SiCN MEMS fabrication. Sensors and Actuators A: Physical **95**, 143-151 (2002).

16. Cromme, P., Scheffler, M. & Greil, P. Ceramic Tapes from Preceramic Polymers. Advanced Engineering Materials **4**, 873-877 (2002).

17. Yoon, B.-H., Lee, E.-J., Kim, H.-E. & Koh, Y.-H. Highly Aligned Porous Silicon Carbide Ceramics by Freezing Polycarbosilane/Camphene Solution. Journal of the American Ceramic Society **90**, 1753-1759 (2007).

18. Rocha, R. M. d., Greil, P., Bressiani, J. C. & Bressiani, A. H. d. A. Complex-shaped ceramic composites obtained by machining compact polymer-filler mixtures. Materials Research **8**, 191-196 (2005).

19. Lee, H.-J., Yoon, T.-H. & Kim, D.-P. Nano-sized patterns derived from a SiCN preceramic polymer: Fabrication and their characterization. Journal of Physics and Chemistry of Solids **69**, 2131-2136 (2008).

20. Yang, H., Deschatelets, P., Brittain, S. T. & Whitesides, G. M. Fabrication of High Performance Ceramic Microstructures from a Polymeric Precursor Using Soft Lithography. Advanced Materials **13**, 54-58 (2001).

21. Liew, L. A. et al. Fabrication of SiCN MEMS by photopolymerization of pre-ceramic polymer. Sensors and Actuators a-Physical **95**, 120-134 (2002).

22. Bertsch, A., Lorenz, H. & Renaud, P. 3D microfabrication by combining microstereolithography and thick resist UV lithography. Sensors and Actuators A: Physical **73**, 14-23 (1999).

23. Goerke, O., Feike, E., Heine, T., Trampert, A. & Schubert, H. Ceramic coatings processed by spraying of siloxane precursors (polymer-spraying). Journal of the European Ceramic Society **24**, 2141-2147 (2004).

24. Günthner, M. et al. Advanced coatings on the basis of Si(C)N precursors for protection of steel against oxidation. Journal of the European Ceramic Society **29**, 2061-2068 (2009).

25. Wang, Y. M. et al. Preparation, characterization and infrared emissivity properties of polymer derived coating formed on 304 steel. Surface and Coatings Technology **206**, 3772-3776 (2012).

26. Colombo, P., Paulson, T. E. & Pantano, C. G. Synthesis of Silicon Carbide Thin Films with Polycarbosilane (PCS). Journal of the American Ceramic Society **80**, 2333-2340 (1997).

27. Smirnova, T. P. et al. SiCN alloys obtained by remote plasma chemical vapour deposition from novel precursors. Thin Solid Films **429**, 144-151 (2003).

28. Bunsell, A. R. & Piant, A. A review of the development of three generations of small diameter silicon carbide fibres. J Mater Sci **41**, 823-839 (2006).

29. Okamura, K., Shimoo, T., Suzuya, K. & Suzuki, K. SiC-Based Ceramic Fibers Prepared via Organic-to-Inorganic Conversion Process-A Review. Journal of the Ceramic Society of Japan **114**, 445-454 (2006).

30. Hongxu, D. et al. Near-Field Electrospray Microprinting of Polymer-Derived Ceramics. Microelectromechanical Systems, Journal of **22**, 1-3 (2013).

31. An, L. et al. Carbon-Nanotube-Reinforced Polymer-Derived Ceramic Composites. Advanced Materials **16**, 2036-2040 (2004).

32. Shao, G., Zhao, G., Yang, F., Xu, C. & An, L. Ceramic nanocomposites reinforced with a high volume fraction of carbon nanofibers. Materials Letters **68**, 108-111 (2012).

33. Jones, R., Szweda, A. & Petrak, D. Polymer derived ceramic matrix composites. Composites Part A: Applied Science and Manufacturing **30**, 569-575 (1999).

34. Pham, T. A. et al. Three-Dimensional SiCN Ceramic Microstructures via Nano-Stereolithography of Inorganic Polymer Photoresists. Advanced Functional Materials **16**, 1235-1241 (2006).

35. Liew, L. A. et al. Fabrication of SiCN ceramic MEMS using injectable polymer-precursor technique. Sensors and Actuators a-Physical **89**, 64-70 (2001).

36. Liew, L. A. et al. Processing and characterization of silicon carbon-nitride ceramics: application of electrical properties towards MEMS thermal actuators. Sensors and Actuators a-Physical **103**, 171-181 (2003).

37. Liew, L. A. et al. Ceramic MEMS - New materials, innovative processing and future applications. American Ceramic Society Bulletin **80**, 25-30 (2001).

38. Liew, L.-A. et al. Fabrication of SiCN MEMS by photopolymerization of pre-ceramic polymer. Sensors and Actuators A: Physical **95**, 120-134 (2002).

39. Seitz, J., Bill, J., Egger, N. & Aldinger, F. Structural investigations of Si/C/N-ceramics from polysilazane precursors by nuclear magnetic resonance. Journal of the European Ceramic Society **16**, 885-891 (1996).

40. Trassl, S., Suttor, D., Motz, G., Rossler, E. & Ziegler, G. Structural characterisation of silicon carbonitride ceramics derived from polymeric precursors. Journal of the European Ceramic Society **20**, 215-225 (2000).

41. S. Schempp, J. D., P. Lamparter, J. Bill, F. Aldinger. Study of the Atomic Structure and Phase Separation in Amorphous Si-C-N Ceramics by X-Ray and Neutron Diffraction. Zeitschrift für Naturforschung A **53a**, 127-133 (1998).

42. Dürr, J., Lamparter, P., Bill, J., Steeb, S. & Aldinger, F. An X-ray and neutron scattering investigation of precursor derived Si24C43N33 ceramics. Journal of Non-Crystalline Solids **232**, 155-161 (1998).

43. Dasgupta, K. & Sathiyamoorthy, D. Disordered carbon - its preparation, structure, and characterisation. Materials Science and Technology **19**, 995-1002 (2003).

44. Jiang, T., Wang, Y. S., Wang, Y. G., Orlovskaya, N. & An, L. N. Quantitative Raman Analysis of Free Carbon in Polymer-Derived Ceramics. Journal of the American Ceramic Society **92**, 2455-2458 (2009).

45. Stormer, H., Kleebe, H. J. & Ziegler, G. Metastable SiCN glass matrices studied by energy-filtered electron diffraction pattern analysis. Journal of Non-Crystalline Solids **353**, 2867-2877 (2007).

46. Gregori, G., Kleebe, H. J., Brequel, H., Enzo, S. & Ziegler, G. Microstructure evolution of precursors-derived SiCN ceramics upon thermal treatment between 1000 and 1400 degrees C. Journal of Non-Crystalline Solids **351**, 1393-1402 (2005).

47. Trassl, S., Motz, G., Rössler, E. & Ziegler, G. Characterization of the Free-Carbon Phase in Precursor-Derived Si-C-N Ceramics: I, Spectroscopic Methods. Journal of the American Ceramic Society **85**, 239-244 (2002).

48. Saha, A., Raj, R., Williamson, D. L. & Kleebe, H. J. Characterization of Nanodomains in Polymer-Derived SiCN Ceramics Employing Multiple Techniques. Journal of the American Ceramic Society **88**, 232-234 (2005).

49. Ferrari, A. C. et al. Raman Spectrum of Graphene and Graphene Layers. Physical Review Letters **97**, 187401 (2006).

50. Mera, G., Tamayo, A., Nguyen, H., Sen, S. & Riedel, R. Nanodomain Structure of Carbon-Rich Silicon Carbonitride Polymer-Derived Ceramics. Journal of the American Ceramic Society **93**, 1169-1175 (2010).

51. Trimmel, G. et al. Solid State NMR and TG/MS Study on the Transformation of Methyl Groups During Pyrolysis of Preceramic Precursors to SiOC Glasses. Journal of Sol-Gel Science and Technology **26**, 279-283 (2003).

52. Widgeon, S. J. et al. 29Si and 13C Solid-State NMR Spectroscopic Study of Nanometer-Scale Structure and Mass Fractal Characteristics of Amorphous

Polymer Derived Silicon Oxycarbide Ceramics. Chemistry of Materials **22**, 6221-6228 (2010).

53. Berger, F., Müller, A., Aldinger, F. & Müller, K. Solid-state NMR Investigations on Si-B-C-N Ceramics derived from Boron-Modified Poly(allylmethylsilazane). Zeitschrift für anorganische und allgemeine Chemie **631**, 355-363 (2005).

54. Andronenko, S. I., Stiharu, I. & Misra, S. K. Synthesis and characterization of polyureasilazane derived SiCN ceramics. Journal of Applied Physics **99**, 113907-113905 (2006).

55. Sehlleier, Y. H., Akdogan, Y., Verhoeven, A., Roduner, E. & Jansen, M. EPR Studies of SiBNC Preceramic Polymers and Ceramic Employing Isotope Labeling. Chemistry of Materials **20**, 7563-7569 (2008).

56. Sorarù, G. D., Mercadini, M., Maschio, R. D., Taulelle, F. & Babonneau, F. Si-Al-O-N Fibers from Polymeric Precursor: Synthesis, Structural, and Mechanical Characterization. Journal of the American Ceramic Society **76**, 2595-2600 (1993).

57. Galusek, D., Riley, F. L. & Riedel, R. Nanoindentation of a Polymer-Derived Amorphous Silicon Carbonitride Ceramic. Journal of the American Ceramic Society **84**, 1164-1166 (2001).

58. Moysan, C., Riedel, R., Harshe, R., Rouxel, T. & Augereau, F. Mechanical characterization of a polysiloxane-derived SiOC glass. Journal of the European Ceramic Society **27**, 397-403 (2007).

59. Moraes, K. V. & Interrante, L. V. Processing, Fracture Toughness, and Vickers Hardness of Allylhydridopolycarbosilane-Derived Silicon Carbide. Journal of the American Ceramic Society **86**, 342-346 (2003).

60. Haluschka, C., Engel, C. & Riedel, R. Silicon carbonitride ceramics derived from polysilazanes Part II. Investigation of electrical properties. Journal of the European Ceramic Society **20**, 1365-1374 (2000).

61. Galusek, D. et al. In-situ carbon content adjustment in polysilazane derived amorphous SiCN bulk ceramics. Journal of the European Ceramic Society **19**, 1911-1921 (1999).

62. Ramakrishnan, P. A. et al. Silicoboron-carbonitride ceramics: A class of high-temperature, dopable electronic materials. Applied Physics Letters **78**, 3076-3078 (2001).

63. Chollon, G. Oxidation behaviour of ceramic fibres from the Si–C–N–O system and related sub-systems. Journal of the European Ceramic Society **20**, 1959-1974 (2000).

64. Modena, S., Soraru, G. D., Blum, Y. & Raj, R. Passive Oxidation of an Effluent System: The Case of Polymer-Derived SiCO. Journal of the American Ceramic Society **88**, 339-345 (2005).

65. Baldus, P., Jansen, M. & Sporn, D. Ceramic Fibers for Matrix Composites in High-Temperature Engine Applications. Science **285**, 699-703, doi:10.1126/science.285.5428.699 (1999).

66. Wang, Y. et al. Silicoaluminum carbonitride ceramic resist to oxidation/corrosion in water vapor. Journal of Materials Research **21**, 1625-1628 (2006).

67. Zhang, Y., Quaranta, A. & Domenico Soraru, G. Synthesis and luminescent properties of novel Eu2+-doped silicon oxycarbide glasses. Optical Materials **24**, 601-605 (2004).

68. Pivin, J. C., Jimenez De Castro, M. & Sendova-Vassileva, M. Optical activation of Er ions by Si nanocrystals in films synthesized by sol–gel chemistry and ion implantation. Journal of Materials Science: Materials in Electronics **14**, 661-664 (2003).

69. Haubler, M. et al. Hyperbranched Poly(ferrocenylene)s Containing Groups 14 and 15 Elements: Syntheses, Optical and Thermal Properties, and Pyrolytic Transformations into Nanostructured Magnetoceramics. J Inorg Organomet Polym **15**, 67-81 (2005).

70. Sun, Q. et al. Nanocluster-Containing Mesoporous Magnetoceramics from Hyperbranched Organometallic Polymer Precursors†. Chemistry of Materials **12**, 2617-2624 (2000).

71. Riedel, R. et al. A silicoboron carbonitride ceramic stable to 2,000^{o}C. Nature **382**, 796-798 (1996).

72. Riedel, R., Ruwisch, L., An, L. & Raj, R. Amorphous silicoboron carbonitride ceramics with anomalously high resistance to creep. J. Am. Ceram. Soc **81**, 3341-3344 (1998).

73. Riedel, R., Ruswisch, L. M., An, L. N. & Raj, R. Amorphous silicoboron carbonitride ceramic with very high viscosity at temperatures above 1500 degrees C. Journal of the American Ceramic Society **81**, 3341-3344 (1998).

74. An, L. A., Riedel, R., Konetschny, C., Kleebe, H. J. & Raj, R. Newtonian viscosity of amorphous silicon carbonitride at high temperature. Journal of the American Ceramic Society **81**, 1349-1352 (1998).

75. Bahloul, D., Pereira, M. & Goursat, P. Silicon Carbonitride Derived from an Organometallic Precursor - Influence of the Microstructure on the Oxidation Behavior. Ceramics International **18**, 1-9 (1992).

76. Delverdier, O., Monthioux, M., Mocaer, D. & Pailler, R. Thermal behavior of polymer-derived ceramics. I. Si-C and Si-C-O systems from both commercial and new polycarbosilane (PCS) precursors. Journal of the European Ceramic Society **12**, 27-41 (1993).

77. Jacobson, N. S. Corrosion of Silicon-Based Ceramics in Combustion Environments. Journal of the American Ceramic Society **76**, 3-28 (1993).

78. Tressler, R. E. in Corrosion of Advanced Ceramics Vol. 267 NATO Science Series E: (closed) (ed KlausG Nickel) Ch. 1, 3-23 (Springer Netherlands, 1994).

79. Varga, T. et al. Thermodynamically Stable SixOyCz Polymer-Like Amorphous Ceramics. Journal of the American Ceramic Society **90**, 3213-3219 (2007).

80. Butchereit, E., Nickel, K. G. & Müller, A. Precursor-Derived Si-B-C-N Ceramics: Oxidation Kinetics. Journal of the American Ceramic Society **84**, 2184-2188 (2001).

81. An, L. et al. Silicoaluminum Carbonitride with Anomalously High Resistance to Oxidation and Hot Corrosion. Advanced Engineering Materials **6**, 337-340 (2004).

82. An, L. N. et al. Silicoaluminum carbonitride with anomalously high resistance to oxidation and hot corrosion. Advanced Engineering Materials **6**, 337-340 (2004).

83. Wang, Y., Fei, W. & An, L. Oxidation/Corrosion of Polymer-Derived SiAlCN Ceramics in Water Vapor. Journal of the American Ceramic Society **89**, 1079-1082 (2006).

84. Wang, Y. G. et al. Oxidation of polymer-derived SiAlCN ceramics. Journal of the American Ceramic Society **88**, 3075-3080 (2005).

85. Wang, Y. G., Fan, Y., Zhang, L. G., Zhang, W. G. & An, L. A. Polymer-derived SiAlCN ceramics resist oxidation at 1400 degrees C. Scripta Materialia **55**, 295-297 (2006).

86. Greil, P. Polymer derived engineering ceramics. Advanced Engineering Materials **2**, 339-348 (2000).

87. Cordelair, J. & Greil, P. Electrical conductivity measurements as a microprobe for structure transitions in polysiloxane derived Si-O-C ceramics. Journal of the European Ceramic Society **20**, 1947-1957 (2000).

88. Hermann, A. M. et al. Structure and electronic transport properties of Si-(B)-C-N ceramics. Journal of the American Ceramic Society **84**, 2260-2264 (2001).

89. Trassl, S., Puchinger, M., Rossler, E. & Ziegler, G. Electrical properties of amorphous SiCxNyHz-ceramics derived from polyvinylsilazane. Journal of the European Ceramic Society **23**, 781-789 (2003).

90. Wang, Y. S. et al. Effect of Thermal Initiator Concentration on the Electrical Behavior of Polymer-Derived Amorphous Silicon Carbonitrides. Journal of the American Ceramic Society **91**, 3971-3975 (2008).

91. Cordelair, J. & Greil, P. Electrical conductivity measurements as a microprobe for structure transitions in polysiloxane derived Si–O–C ceramics. Journal of the European Ceramic Society **20**, 1947-1957 (2000).

92. Wang, Y., Jiang, T., Zhang, L. & An, L. Electron Transport in Polymer-Derived Amorphous Silicon Oxycarbonitride Ceramics. Journal of the American Ceramic Society **92**, 1603-1606 (2009).

93. Ryu, H.-Y., Wang, Q. & Raj, R. Ultrahigh-Temperature Semiconductors Made from Polymer-Derived Ceramics. Journal of the American Ceramic Society **93**, 1668-1676 (2010).

94. Zhang, L. et al. A Silicon Carbonitride Ceramic with Anomalously High Piezoresistivity. Journal of the American Ceramic Society **91**, 1346-1349 (2008).

95. Wang, Y. et al. Effect of Thermal Initiator Concentration on the Electrical Behavior of Polymer-Derived Amorphous Silicon Carbonitrides. Journal of the American Ceramic Society **91**, 3971-3975 (2008).

96. Kao, K. C. Dielectric phenomena in solids. (Elsevier Academic Press, 2004).

97 Jiang, T. Electric properties and microstructures of amorphous SiCN ceramics derived from polymer precursors. Ph.D dissertation, University of Central Florida (2009).

98. Yu, Z., Min, H., Zhan, J. & Yang, L. Preparation and dielectric properties of polymer-derived SiCTi ceramics. Ceramics International **39**, 3999-4007 (2013).

99. Li, X., Zhang, L., Yin, X. & Yu, Z. Mechanical and dielectric properties of porous Si3N4–SiC(BN) ceramic. Journal of Alloys and Compounds **490**, 40-43 (2010).

100. Xinhua, R., Tao, J., Yiguang, W., An, L. & Xun, G. in Wireless and Microwave Technology Conference, 2009. WAMICON '09. IEEE 10th Annual. 1-4.

101. Xinhua, R., Ebadi, S., Yaohan, C., Linan, A. & Xun, G. Characterization of SiCN Ceramic Material Dielectric Properties at High Temperatures for Harsh Environment Sensing Applications. Microwave Theory and Techniques, IEEE Transactions on **61**, 960-971 (2013).

102. BHATTACHARYA et al. Characterization of Yb_2O_3 based optical temperature sensor for high temperature applications. Vol. 134 (Elsevier, 2007).

103. Lutz, S. S. et al. Remote temperature-measurement instrumentation for a heated rotating turbine disk. (1988).

104. Batha, H. & Carroll, P. Unicrystalline Silicon Carbide Thermistor. Component Parts, IEEE Transactions on **11**, 129-134 (1964).

105. Casady, J. B., Dillard, W. C., Johnson, R. W. & Rao, U. A hybrid 6H-SiC temperature sensor operational from 25°C to 500°C. Components, Packaging, and Manufacturing Technology, Part A, IEEE Transactions on **19**, 416-422 (1996).

106. de Vasconcelos, E. A., Khan, S. A., Zhang, W. Y., Uchida, H. & Katsube, T. Highly sensitive thermistors based on high-purity polycrystalline cubic silicon carbide. Sensors and Actuators A: Physical **83**, 167-171 (2000).

107. Yang, J. A Silicon Carbide Wireless Temperature Sensing System for High Temperature Applications. Sensors **13**, 1884-1901 (2013).

108. Smietana, M., Bock, W. J. & Mikulic, P. Temperature sensitivity of silicon nitride nanocoated long-period gratings working in various surrounding media. Measurement Science and Technology **22**, 115203 (2011).

109. Leo, A., Andronenko, S., Stiharu, I. & Bhat, R. B. Characterization of Thick and Thin Film SiCN for Pressure Sensing at High Temperatures. Sensors **10**, 1338-1354 (2010).

110. Seo, D. et al. Fabrication and electrical properties of polymer-derived ceramic (PDC) thin films for high-temperature heat flux sensors. Sensors and Actuators A: Physical **165**, 250-255 (2011).

CHAPTER THREE: SiAlCN CERAMICS PREPARATION AND CHARACTERIZATION

In this chapter, the process for fabricating polymer-derived SiAlCN ceramics is described. The as-received ceramics are characterized by using the XRD, EPR, Raman and NMR spectroscopy methods in order to get better understanding of the structure-property relationships. It is found that SiAlCN ceramics are no detectable weight loss and large scale crystallization after heat treatment at 1500 °C. A significant number of defects were observed in amorphous ceramics, which were carbon related defects. With increasing pyrolysis temperature, the concentration of defects increased until a maximum number was obtained at 1000 °C. After this temperature a decrease of defects was observed. Raman spectra revealed that "free carbon" became more ordered with increasing pyrolysis temperature. NMR results indicated that the main units were SiN_4 and $SiCN_3$; presence of SiO_4 and the Al coordination complexess of AlN_5 and AlN_6. These results are helpful to understand the electric and dielectric properties of SiAlCN ceramics.

3.1 SiAlCN ceramics preparation

3.1.1 Raw materials

Commercially available liquid polysilazane (HTT1800, KiON Corp, Columbus, OH) was used as main precursor and the Aluminum-tri-sec-butoxide (ASB, Sigma-Aldrich, USA) as the Al source. Dicumyl Peroxide (DP, Sigma-Aldrich, USA) was used as the thermal initiator. HTT1800 as received is a clear and dilute liquid, ASB is

a clear and sticky liquid and DP is a white solid crystal. The molecular formulas of HTT1800, ASB and DP are shown in Fig 3.1, Figure 3.2 and Figure 3.3, respectively.

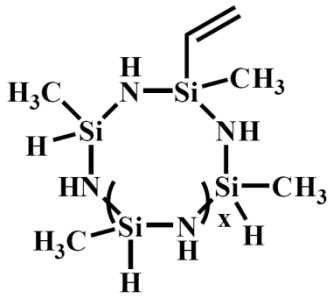

Figure 3.1 The molecular formula of HTT1800.

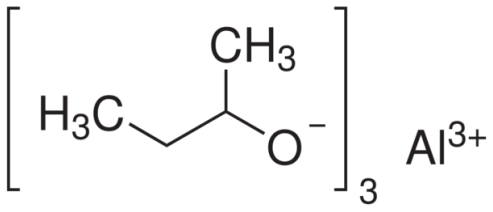

Figure 3.2 The molecular formula of ASB.

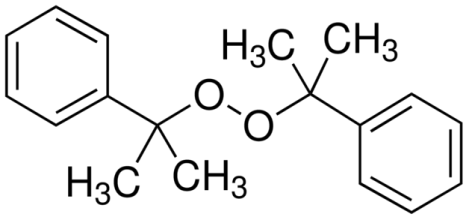

Figure 3.3 The molecular formula of DP.

3.1.2 Experimental procedure

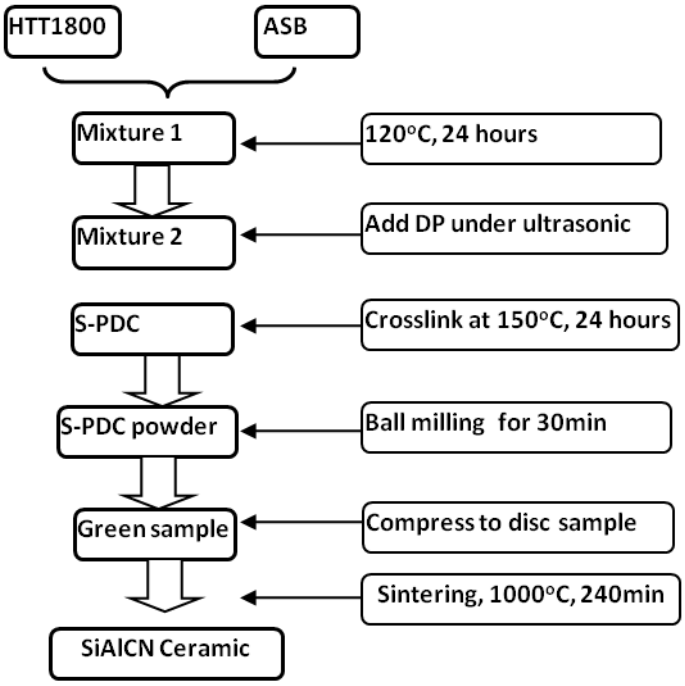

Figure 3.4 Preparation procedure of SiAlCN ceramics.

The detail experimental procedure chart is shown in Figure3.4 and described as following (10ASB, 2DP sample was used as an example):

(1) A mixture of HTT1800 and ASB was heated at 120 °C for 24 hours with magnetic stirring.

(2) The mixture in step (1) was cooled to room temperature, at which point 2 wt% DP was added under ultrasonic untill the solid all dissolved.

(3) The mixture in step (2) was allowed to crosslink by heating at a temperature of150 °C for 24 hours with the protection of N_2.

(4) Cross-linked solid obtained from step (3) was ground to a fine powder using a high energy ball milling method for 30min.

(5) The powder obtained from step (4) was compressed into thin discs (Φ12.5 mm×4~6 mm) using a hydraulic laboratory press (4 tons for 4 min).

(6) The thin discs obtained in step (5) were pyrolyzed at 1000°C for 4 hours with the procedure shown in Figure 3.5.

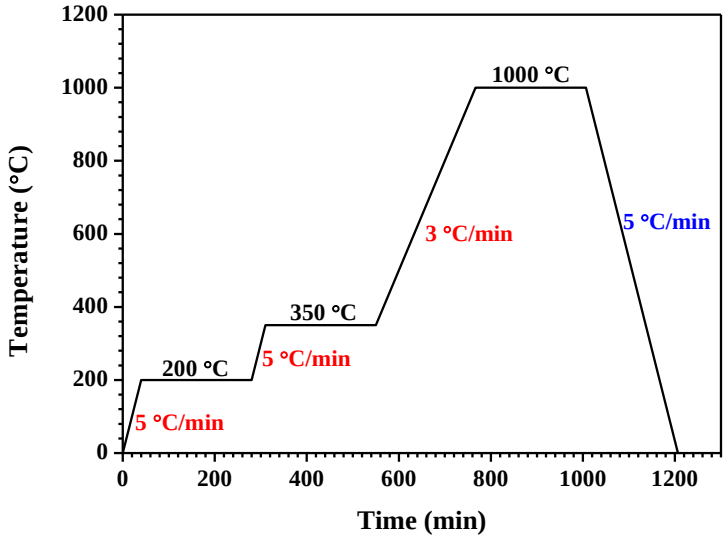

Figure 3.5 A schematic drawing of the sintering procedure of SiAlCN ceramics.

SiAlCN ceramics were heat treated at high temperature of 1100, 1200, 1300, 1400 and 1500 °C By using the same sintering procedure shown in Figure3.5. The other two compositions of 5ASB2DP and 1ASB2DP were prepared for comparison and the composition design is listed in Table 3.1.

Table 3.1 Composition design of SiAlCN ceramics

	HTT1800 (wt%)	ASB (wt%)	DP (wt%)
10ASB2DP	88	10	2
5ASB2DP	93	5	2
1ASB2DP	97	1	2

3.2 SiAlCN ceramics characterization, results and discussion

3.2.1 Solid-state NMR

Solid-state nuclear magnetic resonance spectroscopy has been demonstrated be one of the most powerful and accurate techniques that can be used to investigate the local environment and atomic coordination of polymer-derived ceramics.

In this study, ^{27}Al and ^{29}Si solid state magic angle spinning (MAS) NMR experiments were carried out on a Chemagnetics 300 MHz Infinity spectrometer at Larmor frequencies of 78.2 and 59.6 MHz for ^{27}Al and ^{29}Si, respectively. A standard CP/MAS probe with a 7.5 mm pencil rotor system was used. The sample spin rate of 10 kHz was used for both ^{29}Si and ^{27}Al. All ^{27}Al and ^{29}Si spectra acquired utilized a standard single pulse sequence with a tip angle of about 45 degrees and a recycle delay time of 0.5s ^{27}Al and 10s (^{29}Si) with accumulation numbers varying between several hundred to 30,000 scans. The ^{27}Al chemical shifts were referenced to $Al(H_2O)_6^{3+}$ (1M Aluminum nitrate) and the ^{29}Si chemical shifts were referenced to tetrakis(trimethylsilyl)silane (TTMS).

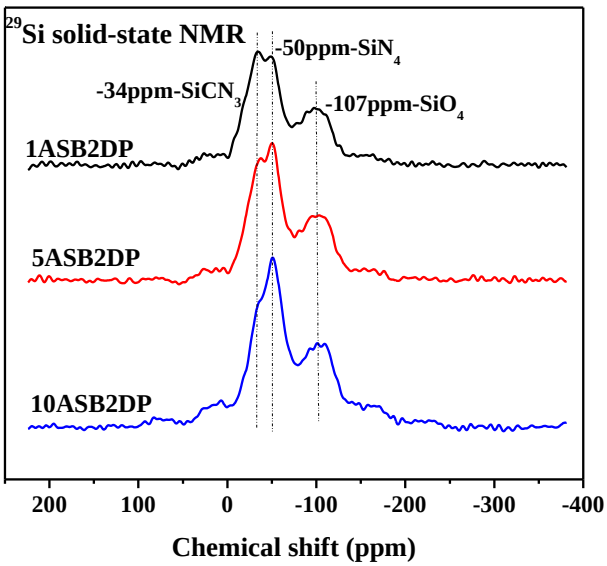

Figure 3.6 ^{29}Si solid-state NMR of SiAlCN ceramics sintered at 1000 °C with different ASB concentrations of 1, 5 and 10 wt% .

Figure 3.6 shows the ^{29}Si solid-state NMR spectra of SiAlCN ceramics sintered at 1000 °C with different ASB concentration of 1, 5 and 10 wt%. As can be seen from this figure, three main peaks were found at about –107, –50 and –34 ppm for all these three compositions, corresponding to SiO_4, SiN_4 and $SiCN_3$, respectively[1-4]. The presence of fairly large amount of SiO_4 units should be caused by our processing of high energy ball milling. In this step, oxygen was imported into our sample for lacking of effective protection. The $SiCN_3$ and SiN_4 units should be formed from the SiC_2N_2 and $SiCHN_2$ with the reaction of N-H and Si-H group, as shown in Eq. (3-1), Eq. (3-2) and Eq. (3-3)[5-7].

$$CH_3 + NSiC_2N \rightarrow Si_3N + NH_3 \ (\uparrow) \qquad \text{Eq. (3-1)}$$

$$Si\text{-}CH_3 + N\text{-}H \rightarrow Si\text{-}N + CH_4 \uparrow \qquad \text{Eq. (3-2)}$$

$$N\text{-}H + Si\text{-}H \rightarrow Si\text{-}N + H_2 \uparrow \qquad \text{Eq. (3-3)}$$

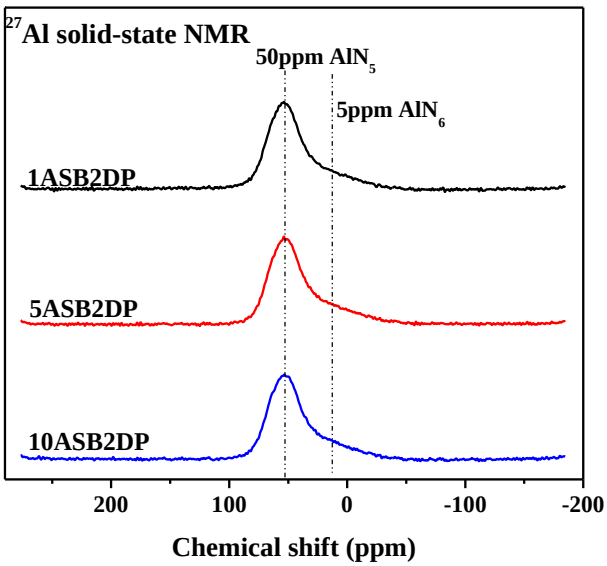

Figure 3.7 ^{27}Al solid-state NMR of SiAlCN ceramics sintered at 1000 °C with different ASB concentration of 1, 5 and 10 wt% .

The ^{27}Al solid-state NMR of SiAlCN ceramics sintered at 1000 °C with different ASB concentration of 1, 5 and 10 wt% are shown in Figure 3.7. It was found that there is only one main peak at 51 ppm for aluminum with 5-coodinates (AlN_5). However, at the same time a small shoulder at high field is caused by the aluminum with 6-coordinates (AlN_6) at about 5 ppm. The Al-N was formed by the reaction of Al-O bands in ASB with N-H bonds in HTT1800, as shown in Eq. (3-4), which has been demonstrated a favorable reaction[8-10].

$$\text{N-H (in HTT1800)} + \text{Al-O (in ASB)} \longrightarrow \text{Al-N} \qquad \text{Eq. (3-4)}$$

It is found that the relative peak intensity of $SiCN_3$ (–34 ppm) and SiN_4 (–50 ppm) decreased with increasing ASB concentration from 1 wt% to 10 wt% in Figure 3.6. That is to say that more ASB concentration contributes to formation of Al-N shown in Eq. (3-4). It means that the ASB hold N well in the final ceramic.

3.2.2 X-ray diffraction (XRD)

X-ray scattering techniques are a family of non-destructive analytical techniques which reveal information about the crystal structure, chemical composition, and physical properties of materials and thin films. In this study, XRD was applied to characterize the crystallization behavior of SiAlCN ceramics by Rigaku D/MAX X-ray Diffractometer (XRD Rigaku, Tokyo, Japan) with a monochromatic Cu-Kα radiation and a wavelength of 0.154 nm.

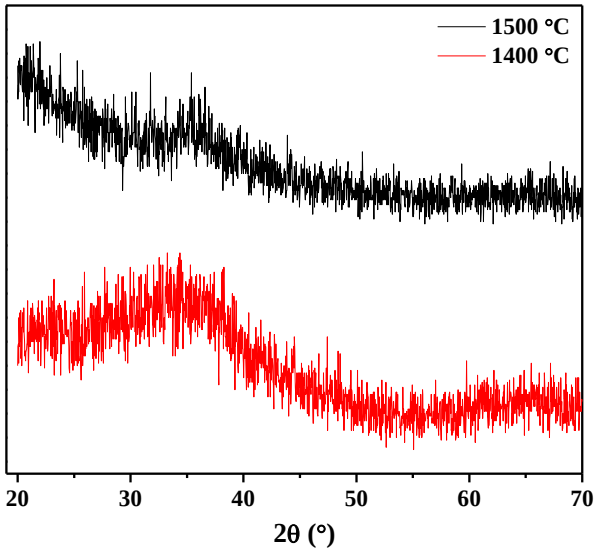

Figure 3.8 XRD pattern of 10ASB2DP-SiAlCN ceramics sintered at 1400, 1500 °C.

Figure 3.8 shows the XRD pattern of 10ASB2DP SiAlCN ceramics sintered at 1400 and 1500 °C. It can be seen that the majority phase is amorphous for both samples sintered temperature of 1400 and 1500 °C. Slightly crystallization of β-SiC was found for the sample sintered at 1500^{o}C. That maybe due to the carbothermal

reaction between silicon nitride and carbon with the production of silicon carbide and nitrogen, as shown in Eq. (3-5).

$$Si_3N_4\ (s)+3C\ (s) \rightarrow 3SiC\ (s)+2N_2\ (g) \qquad \text{Eq. (3-5)}$$

The SiAlCN ceramics was mainly amorphous at the temperature 1500 °C which is higher than that of without Al doping PDC, due to the presence of the Al. Researchers believe that Al will dissolve into the silicon nitride and cause higher crystallization temperature of SiAlCN ceramics.

3.2.3 Electron paramagnetic resonance spectroscopy (EPR)

The electron paramagnetic resonance spectroscopy is a powerful tool to determine the unpaired electron spins or named dangling bonds in materials by knowing their defect concentration and status of distribution. This technique is usually applied to indentify the defect species and concentration of PDCs. The X-band (9.7 GHz) EPR spectra of the various SiAlCN ceramics at room temperatures were recorded on a Bruker ESP 300E (Bruker, Germany) spectrometer equipped with a Bruker ER 035 M NMR gaussmeter and a Hewlett-Packard HP 5350B microwave frequency counter at the National High Magnetic Field Laboratory (NHMFL) in Tallahassee.

The X-band EPR spectra of SiAlCN ceramics sintered at 1000 °C was obtained for samples that contained with different ASB concentrations (1, 5 and 10 wt%). SiAlCN ceramics (10 wt.% ASB) sintered at different temperatures from 1000 ℃ to

1500 ℃ with an internal of 100 ℃ are shown in Figure 9 and Figure 10, respectively. The g-factor of 2.0016±0.0006 could be seen from the center position of first integrity of the spectra for all samples. This result indicates that the defects in SiAlCN ceramics are carbon-related unpaired electrons, so called "carbon dangling bonds" and these are the only unpaired electrons in our system not originating from silicon (g = 2.005) nor carbon in matrix phase (g = 2.0032). As we can see from Figure 3.11, the spin concentration of 10wt% ASB SiAlCN ceramics first increased from 600 °C to 1000 °C to achieve the maximum value and then continually decreased afterward. It reveals that the free carbon gradually formed by increasing the pyrolysis temperature and totally formed at 1000 °C and with continually increasing temperature the free carbon tends to become order and order. These results were confirmed by the Raman spectra analysis later on.

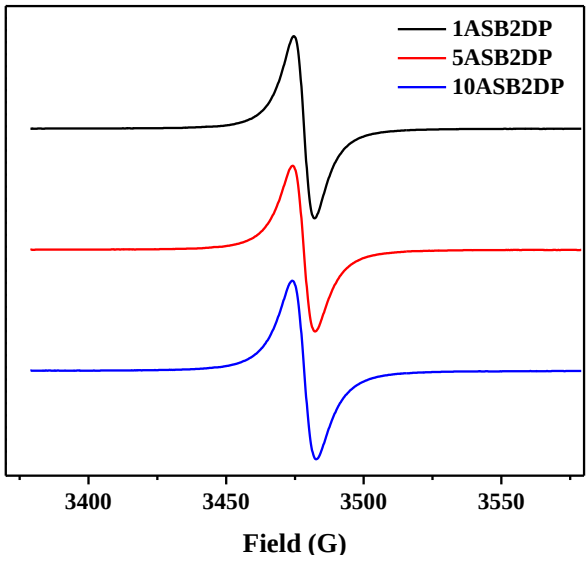

Figure 3.9 EPR spectra of SiAlCN ceramics sintered at 1000 °C with different ASB concentration of 1, 5 and 10wt%.

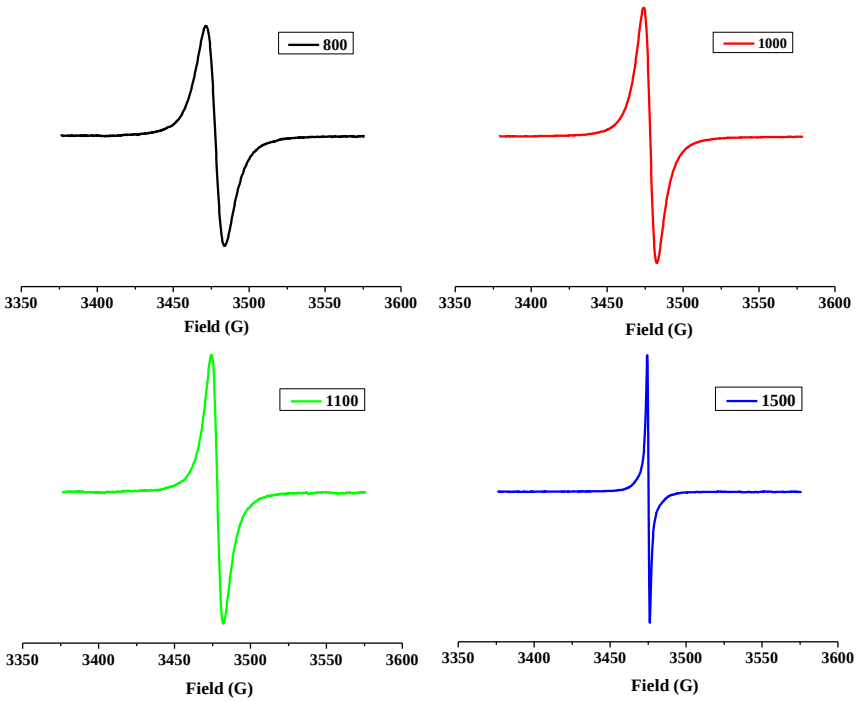

Figure 3.10 EPR spectra of 10ASB2DP SiAlCN ceramics sintered at different temperatures.

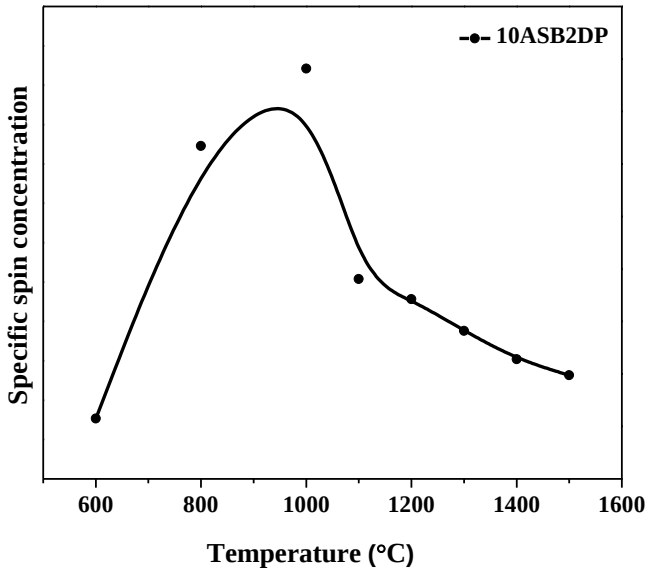

Figure 3.11 Spin concentration of 10ASB2DP SiAlCN ceramics sintered at various temperatures.

3.2.4 Raman Spectroscopy

Raman spectroscopy is a useful tool to obtain the structure-properties information of molecular non-destructively, by considering their vibrational transitions. Raman spectroscopy is widely used in detecting the free carbon structure of PDCs, recently. In this study, the Renishaw inVia Raman microscopy was used (Renishaw Inc., Gloucestershire, UK), with a 532 nm line of silicon-solid laser excitation source and a ×50 objective lens. Twenty-five Raman spectra were obtained for each sample by a 10 μm×10 μm mapping acquisition for minimizing the measuring error.

Researchers that work on the field of PDCs conclude that the "free carbon" will be formed during the pyrolysis of PDCs and it plays an important role in the determination of properties of PDCs. Such properties include high temperature thermal stability and electric properties[1,6,11,12]. In this study, Raman spectroscopy was used to characterize the "free carbon" in order to help to understand the intrinsic science of electric properties variation within SiAlCN ceramics.

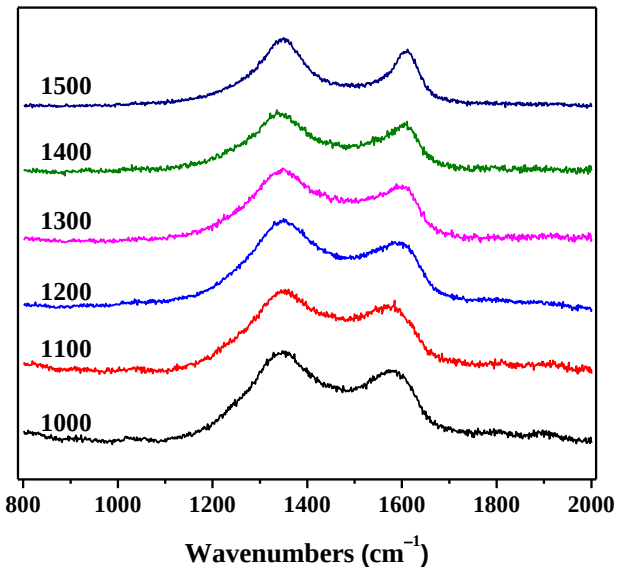

Figure 3.12 Raman spectra of 10ASB-SiAlCN ceramics sintered at different temperatures.

Figure 3.12 contains the Raman spectra of 10ASB-SiAlCN ceramics sintered at different temperatures from 1000~1500 °C with the interval of 100 °C. All the curves show two Reman peaks of D bond at ~1350 cm^{-1} and G band at ~ 1600 cm^{-1}, which are the signs of the presence of "free carbon"[13-16]. The D band is due to the breathing modes of sp^2 atoms in rings and G band is stemmed from in-plane bond stretching of sp^2 carbon.

In order to obtain a accurate quantitative analysis of Raman spectra, the suitable curve fit should be applied. In this study, the Lorentzian function for D peaks and the Breit-Wigner-Fano function for G peaks were used to accomplish the curve fit for all Raman spectra. The Breit–Wigner–Fano function (BWF) obeys the following equation[17]:

$$I(\omega) = \frac{I_0\left[1+2(\omega-\omega_0)/Q\Gamma\right]^2}{1+\left[2(\omega-\omega_0)/\Gamma\right]^2} \qquad \text{Eq. (3-6)}$$

Where I_0 is the peak intensity, ω_0 is the peak position, Γ is assumed as the full width at half maximum (FWHM) and Q^{-1} is the BWF coupling coefficient. The Lorentzian line shape is recovered in the limit $Q^{-1} \rightarrow 0$.

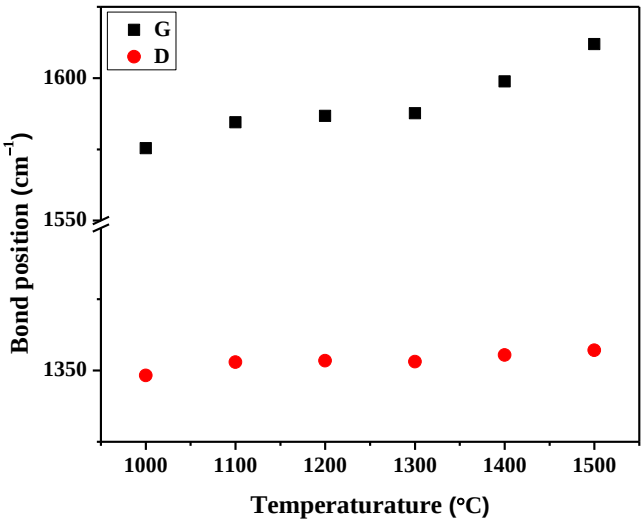

Figure 3.13 D and G peak position of Raman spectra of 10ASB2DP SiAlCN ceramics sintered at different temperatures.

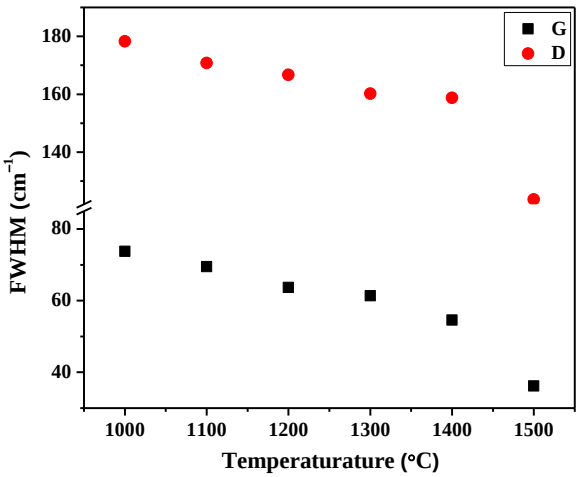

Figure 3.14 FWHM of Raman spectra of 10ASB2DP SiAlCN ceramics sintered at different temperature.

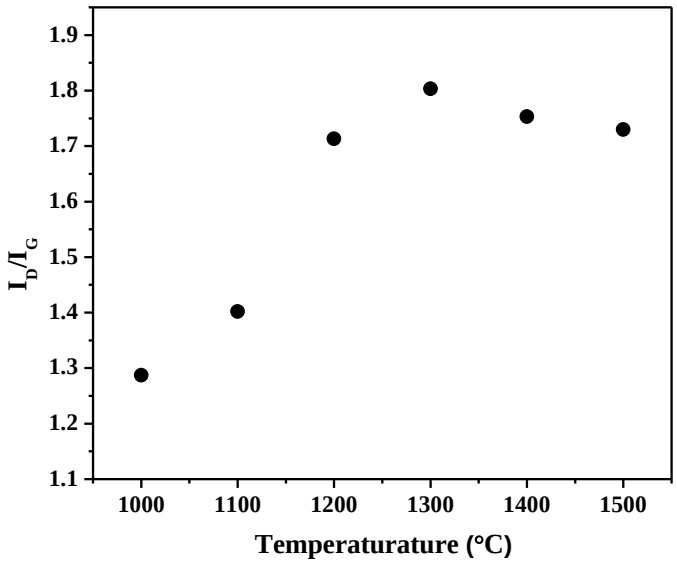

Figure 3.15 Intensity ratio of D and G (I_D/I_G) of Raman spectra of 10ASB2DP SiAlCN ceramics sintered at different temperatures.

The D and G peak position, FWHM and intensity ratio of D and G peak of free carbon are achieved by the abovementioned curve fitting; results are shown in Figure 3.13, Figure 3.14 and Figure 3.15, respectively. The D and G peak position in Figure 3.13 both display an up-shift, from 1348 cm^{-1} to 1357 cm^{-1} for D peak and from 1575 cm^{-1} to 1611 cm^{-1} for G peak with increasing the sintering temperature. The up-shift of D peaks is a sign of increasing of ordered three-fold aromatic rings and the up-shift of G peak is caused by the formation of nanocrystalline carbon. At the same time, the FWHM decreases for both D and G peak with increasing the pyrolysis temperature as shown in Figure 3.14. The up-shift of D and G peak position and reduce of FWHM are all the signs of the free carbon becoming more and more ordered during the post-heat treatment[15,16]. The intensity ratio of D and G peak, I_D/I_G, is shown in Figure 3.15. This ratio of I_D/I_G can be used to calculate the carbon-cluster size, which is well

developed by Tuinstra and Koening (TK)[13] and Ferrari and Robertson (FR)[15] as shown in Eq. (3-7) and Eq. (3-8). In this study, the carbon cluster sizes are calculated by using the FR equation with considering the continuity between TK and FR equation at the critical carbon cluster size of 2 nm[18]. Where $C(\lambda) = C_0 + \lambda C_1$, with $C_0 = -12.6$ nm and $C_1 = 0.033$. The relative data is list in Table 3.2.

$$I_D / I_G = C(\lambda) / L_a \quad \text{Eq. (3-7)}$$

$$I_D / I_G = C'(\lambda) * L_a^2 \quad \text{Eq. (3-8)}$$

From the results in Table 3.2, we can see that the carbon cluster size (La) increases gradually until the sintering temperature of 1300 °C and then slightly decreases. The increase of La was observed because of the grain growth of nanocrystalline with increasing the sintering temperature. Meanwhile the decrease of La at high temperature was observed due to the carbothermal reaction, as described above. The carbon was consumed during this reaction which was the reason for reduction of La.

Table 3.2 Carbon cluster size (La) of 10ASB2DP SiAlCN ceramics sintered at different temperatures

Temperature (°C)	1000	1100	1200	1300	1400	1500
La (nm)	1.441	1.504	1.663	1.706	1.682	1.671

References:

1. Trassl, S., et al., Structural characterisation of silicon carbonitride ceramics derived from polymeric precursors. Journal of the European Ceramic Society, 2000. **20**(2): p. 215-225.
2. Seitz, J., et al., Structural investigations of Si/C/N-ceramics from polysilazane precursors by nuclear magnetic resonance. Journal of the European Ceramic Society, 1996. **16**(8): p. 885-891.
3. Dhamne, A., et al., Polymer-ceramic conversion of liquid polyaluminasilazanes for SiAlCN ceramics. Journal of the American Ceramic Society, 2005. **88**(9): p. 2415-2419.
4. Li, Y.L., et al., Thermal cross-linking and pyrolytic conversion of poly(ureamethylvinyl)silazanes to silicon-based ceramics. Applied Organometallic Chemistry, 2001. **15**(10): p. 820-832.
5. Brodie, N., J.P. Majoral, and J.P. Disson, An Nmr-Study of the Step-by-Step Pyrolysis of a Polysilazane Precursor of Silicon-Nitride. Inorganic Chemistry, 1993. **32**(21): p. 4646-4649.
6. Sarkar, S., et al., Structural Evolution of Polymer-Derived Amorphous SiBCN Ceramics at High Temperature. Journal of Physical Chemistry C, 2011. **115**(50): p. 24993-25000.
7. Chen, Y., et al., Self-assembled carbon-silicon carbonitride nanocomposites: highperformance anode materials for lithium-ion batteries. Journal of Materials Chemistry, 2011. **21**(45): p. 18186-18190.

8. Seyferth, D., G. Brodt, and B. Boury, Polymeric aluminasilazane precursors for aluminosilicon nitride. Journal of Materials Science Letters, 1996. **15**(4): p. 348-349.

9. Boury, B. and D. Seyferth, Preparation of Si/C/Al/N ceramics by pyrolysis of polyaluminasilazanes. Applied Organometallic Chemistry, 1999. **13**(6): p. 431-440.

10. Berger, F., et al., Solid-state NMR studies of the preparation of Si-Al-C-N ceramics from aluminum-modified polysilazanes and polysilylcarbodiimides. Chemistry of Materials, 2004. **16**(5): p. 919-929.

11. Wang, Y.S., et al., Effect of Thermal Initiator Concentration on the Electrical Behavior of Polymer-Derived Amorphous Silicon Carbonitrides. Journal of the American Ceramic Society, 2008. **91**(12): p. 3971-3975.

12. Trassl, S., et al., Electrical properties of amorphous SiCxNyHz-ceramics derived from polyvinylsilazane. Journal of the European Ceramic Society, 2003. **23**(5): p. 781-789.

13. Tuinstra, F. and J.L. Koenig, Raman Spectrum of Graphite. Journal of Chemical Physics, 1970. **53**(3): p. 1126-&.

14. Sadezky, A., et al., Raman micro spectroscopy of soot and related carbonaceous materials: Spectral analysis and structural information. Carbon, 2005. **43**(8): p. 1731-1742.

15. Ferrari, A.C. and J. Robertson, Interpretation of Raman spectra of disordered and amorphous carbon. Physical Review B, 2000. **61**(20): p. 14095-14107.

16. Ferrari, A.C. and J. Robertson, Resonant Raman spectroscopy of disordered, amorphous, and diamondlike carbon. Physical Review B, 2001. **64**(7).

17. Ferreira, E.H.M., et al., Evolution of the Raman spectra from single-, few-, and many-layer graphene with increasing disorder. Physical Review B, 2010. **82**(12).

18. Zickler, G.A., et al., A reconsideration of the relationship between the crystallite size L-a of carbons determined by X-ray diffraction and Raman spectroscopy. Carbon, 2006. **44**(15): p. 3239-3246.

CHAPTER FOUR: ELECTRIC AND DIELECTRIC PROPERTIES OF SiAlCN CERAMICS

The electric properties are considered one of the most important properties of PDCs because they reveal a better and deeper understanding of the intrinsic science of PDC. Previous studies indicate the semiconductor behavior can be sustained to very high temperatures (such as ~1300 °C), which is much higher than that of any existing ceramics (< 800 °C). This unique property makes the PDCs good candidates for high temperature applications. The electric properties of different PDCs systems are reported, such as SiCN, SiOCN and SiBCN, but there are virtually no publications about the electric properties of SiAlCN. The dielectric property is another important function widely used for sensing applications. The dielectric property studies of PDC are very limited and there are no open reports about the dielectric property of SiAlCN ceramics to the best of the author's knowledge.

In this chapter, the electric and dielectric properties of SiAlCN ceramics were characterized and the possible mechanisms were discussed. It was observed that both the conductivity and dielectric constant increased dramatically with increasing temperature (both sintered and test temperature), which indicates that SiAlCN ceramics are well suited for high temperature sensor applications. The "electric field concentration" model was proposed and this model is consistent with the experimental data. The temperature dependent conductivity shows that the conducting mechanism of SiAlCN ceramics follows the Arrhenius equation. The huge dielectric

constant is caused by the space charge effect, which was confirmed by the impendence analysis and the high loss observed from the SiAlCN ceramics exposed to high temperature (both sintered and test temperature), were caused by the increasing of conductivity of the materials.

4.1 Experimental procedure

The cylinder SiAlCN ceramics samples, as received and obtained using the procedure described in Chapter 3, were further heat treated at 800 ℃ for 2 hours in air to remove the carbon deposited on to the surface during pyrolysis. Then, the two surfaces of the SiAlCN ceramics were polished by 15, 9 and 6 μm diamond plate respectively. The polished samples were cleaned by ultrasonic for 5 min in acetone and dried at 120 °C for 1 hour. Finally, the conducting silver paste (SPI) was applied on both sides as the electrode. The D.C. conductivities were calculated from the I-V curves achieved by KEITHLEY 2400. The dielectric properties were characterized by using the Agilent 4298A with the frequency of 20-2 MHz.

4.2 Results and discussion

4.2.1 Electric properties of SiAlCN ceramics

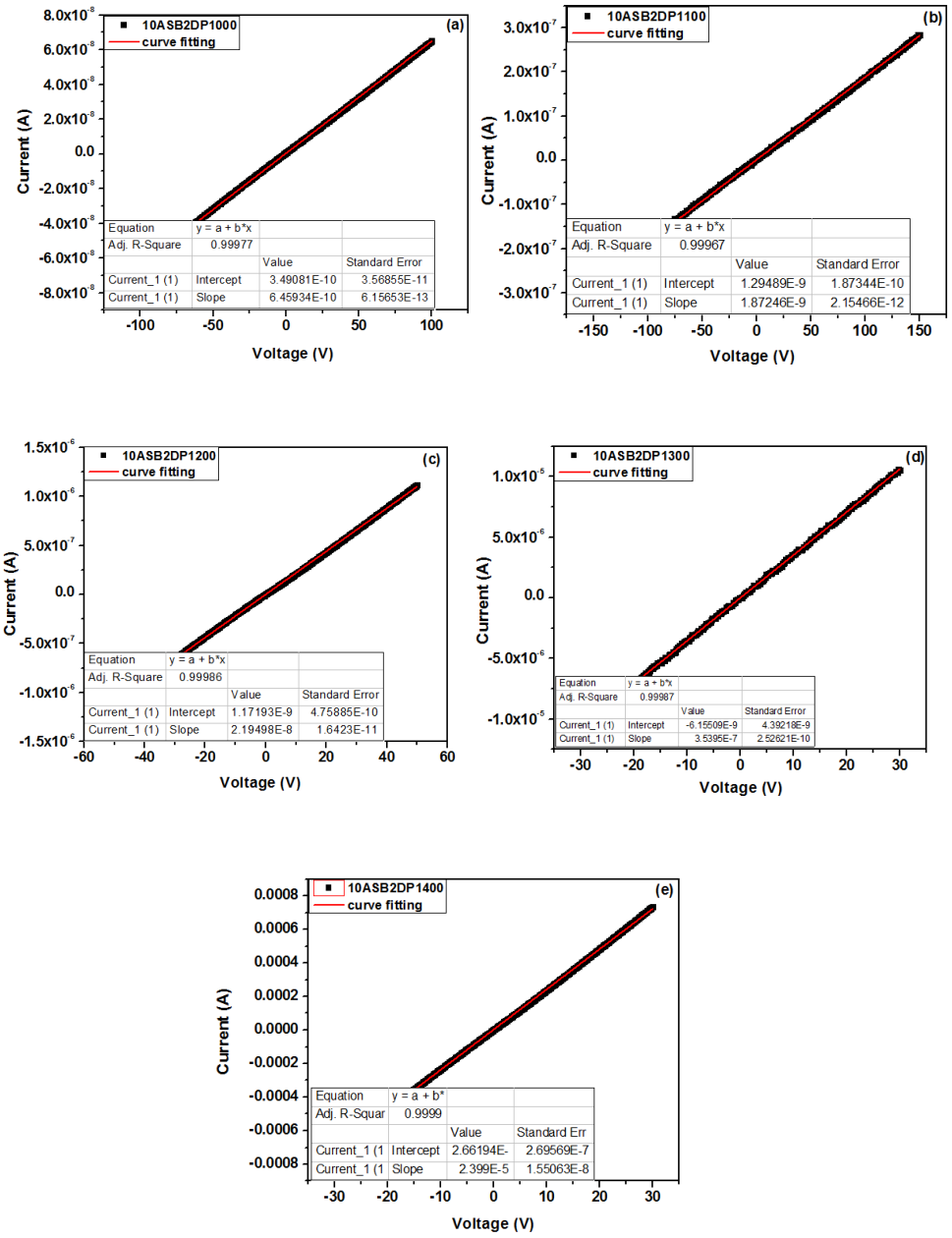

Figure 4.1 I-V curves and the curve fitting of SiAlCN ceramics sintered at different temperature (a) 1000 °C, (b) 1100 °C, (c) 1200 °C, (d) 1300 °C, (e) 1400 °C.

The D.C. conductivity of SiAlCN ceramic samples were calculated by knowing the slop of I-V curve. Figure 4.1 (a)-(e) show the I-V curves and curve fitting results with 10ASB2DP SiAlCN ceramic samples sintered at various temperatures of 1000,

1100, 1200, 1300, and 1400 °C, respectively. From the results in Figure 4.1, we can see that the I-V curves are all in perfect linear relation indicating SiAlCN ceramics follow the Ohm's law. The conductivities of SiAlCN ceramics sintered at various temperatures are listed in Table 4.1 and plotted in Figure 4.2, and the relative data of SiCN are shown and plotted too for comparison.

Table 4.1 Conductivities of SiAlCN and SiCN sintered at various temperatures.

							Activation energy (eV)
SiAlCN	Temperature (° C)	1000	1100	1200	1300	1400	5.1
	Conductivity $(Ohm*cm)^{-1}$	4.14E–10	1.16E–09	1.33E–08	2.03E–07	3.31E–06	
SiCN*	Temperature (° C)	1000	1100	1200	1300	1350	3.41
	Conductivity $(Ohm*cm)^{-1}$	2.06E–09	1.46E–08	1.21E–07	7.69E–07	1.50E–06	

*: Yaohan Chen "STRUCTURE AND PROPERTIES OF POLYMER-DERIVED SiBCN CERAMICS" University of Central Florida, PhD dissertation (2012).

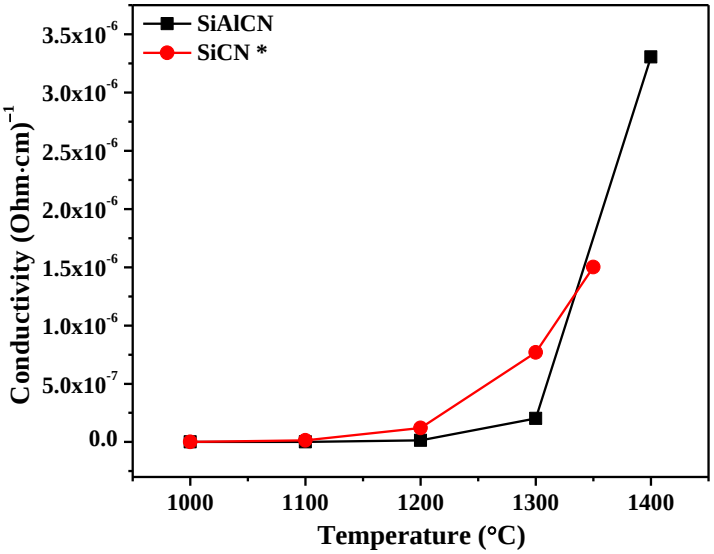

Figure 4.2 Conductivity of SiAlCN ceramics sintered at different temperatures.

The results in Table 4.1 and Figure 4.2 reveal that the conductivity of SiAlCN increases with increasing pyrolysis temperature and the difference is about four orders of magnitude. The observation begs the question; why does the conductivity increase with increasing the pyrolysis temperature dramatically? In order to answer this question, let's take a look at the basic structure of the PDCs. There are mainly two components of the PDC one is amorphous matrix SiC_xN_{1-x} ($0<x<4$), the other is free carbon and the former one is low conductive matrix and the later one is high conductive phase. This structure is similar with the composite with a low conductivity matrix and a high conductivity dispersed particles, first reported by Maxiwell[1]. Most recently, L. Woo and co-works found that the conductivity was improved greatly in the CNT/cement system by the strong field concentration[2]. We believe that in our system the conductivity increase is related to the field concentration. Therefore, we propose the electric field concentration between the conductive free carbon clusters occurs in our SiAlCN system, as illustrated in Figure4.3.

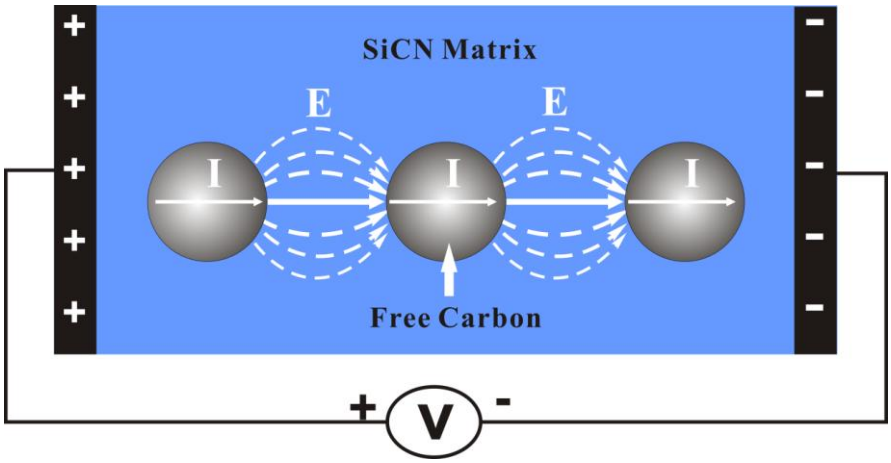

Figure4.3 Schematic illustration of electric field concentration in SiAlCN system.

As can be seen in Figure4.3, the charge carriers (electrons and holes) in the high conductive free carbon clusters will separate to each other and move to the positive and negative electrode, respectively, when the external electric field is applied. The separation of electrons and holes will cause a strong electric field concentration in between two free carbon clusters and hereby the apparent conductivity increased in the overall material. Since the effective electric field is much higher than the external electric field, due to the high electric field concentration, but the electric field used for conductivity calculation is still the external one but not the effective one. As a result, the conductivity is higher than that should be. Meanwhile, the electric field concentration will be enhanced if the conductivity of free carbon increased, for the higher conductivity, the more movable charge carriers. These results are consistent with the structure analysis results described in Chapter 2. In Chapter 2, the Raman spectra shows an up-shift of G-peak position, narrow of the FWHM and EPR spectra shows an reducing of defect concentration with increasing the sintered temperature. These are all the signs of the free carbon becoming order and order with increasing the sintered temperature. The conductivity of free carbon will increase when the free carbon becomes order and order for the increasing of sp^2/sp^3 ratio. In other words, the higher sintered temperature, the higher conductivity of free carbon and therefore, the stronger of the electric field concentration.

Furthermore, if the proposed model is correct, the following facts will be true: there should be only one conducting mechanism before the electric field concentration

was established or when the electric field concentration was neglected; and there should be two conducting mechanisms when the electric field concentration was established. In order to found out the truth, complex impedance of SiAlCN ceramic is investigated, as shown in Figure 4.4. It found that there is only one arc for SiAlCN ceramics sintered at 1000 and 1200 °C, and two semicircles for the sample sintered at 1400 °C. It means that there is only one impedance mechanism for the samples sintered at low temperature (1000 and 1200 °C) and two impedance mechanisms for the high temperature one (1400 °C). For the samples sintered at low temperature (1000 and 1200 °C), the free carbon are not conductive enough (for it is not order enough) to effect the overall impendence, so the material is similar to a single phase material and shows a matrix only conducting mechanism. For the sample sintered at high temperature (1400 °C), the free carbon are highly ordered with a high conductivity and contribute the overall impedance, so the material shows two conducting mechanism (matrix + free carbon in series). The complex impendence results approve that the proposed “electric field concentration” is a right model for the conducting mechanism of our material system.

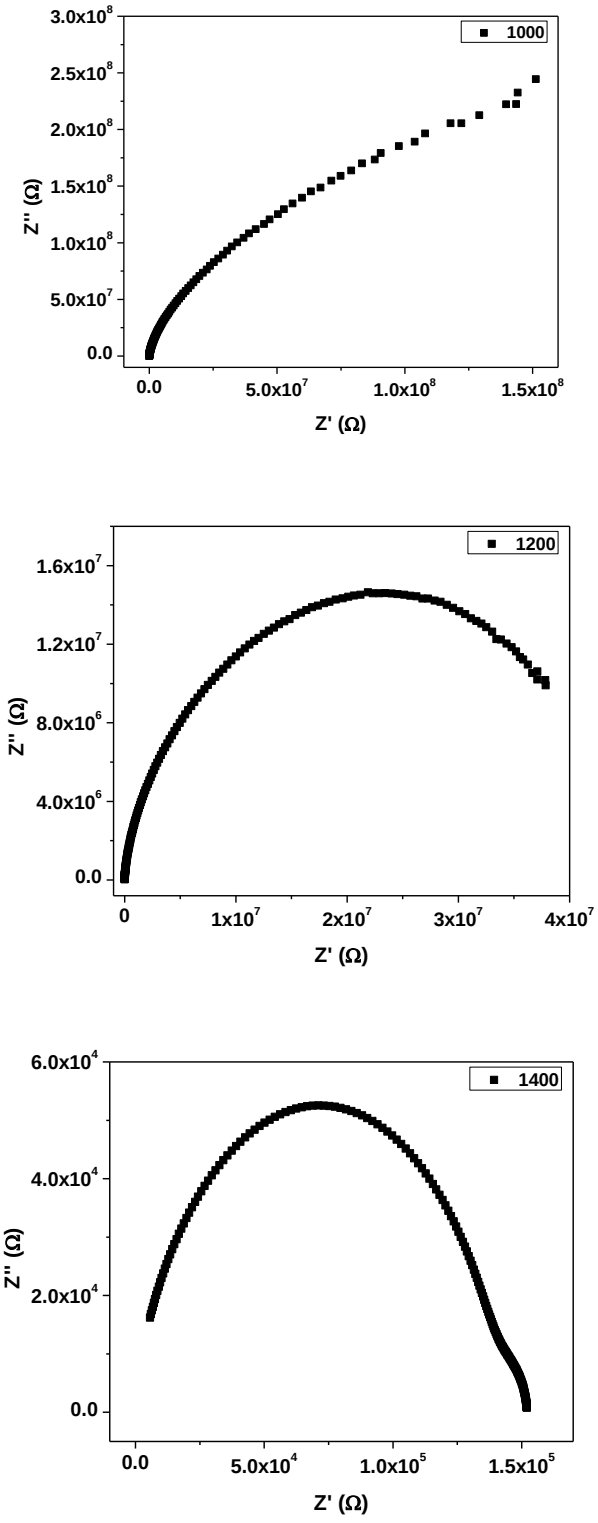

Figure 4.4 Complex impedance analysis of SiAlCN ceramic sintered at different temperatures (a) 1000 °C, (b) 1200 °C and (c) 1400 °C.

The natural logarithm of conductivity with inverse of temperature (in Kelvin) of SiAlCN and SiCN[6] ceramics were plotted in Figure 4.5. It was found that the curves of both SiCN and SiAlCN show a good linear relationship and activation energy can be calculated from the slope listed in Table 4.1 (5.1 eV for SiAlCN and 3.41 eVfor SiCN). In general, the conductivity will increase and activation energy will decrease of the semiconductor, if dopant induced. However, in our case, the conductivity decreased and the activation energy increased with the Al doping, which is opposite with that of normal semiconductors. It means the Al is not the sample doping into the SiCN matrix and not the dominate feature to influence the electric conductivity of SiAlCN ceramics, which is consistent with the above conclusion that free carbon plays an important role in the overall conductivity of SiAlCN ceramics.

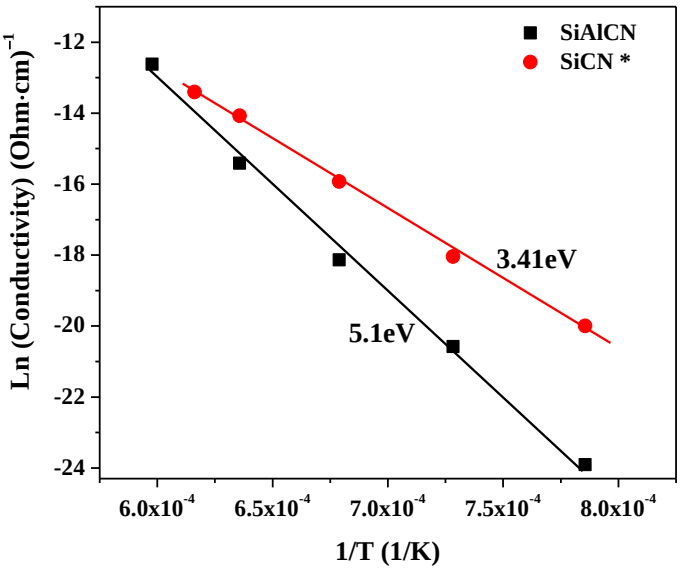

Figure 4.5 Plot of ln (conductivity) VS 1/T of SiAlCN and SiCN ceramics.

As discussed above, the conductivity of free carbon affects the overall conductivity of SiAlCN significantly. At the same time, the conductivity of SiAlCN is highly related to the degree of crystallization of free carbon. Jiang and colleges reported that the activity energy was 7.9 eV for "oxygen rich" SiCN system[7]. The SiAlCN system in our research has a medium of oxygen (observed from the ^{29}Si solid-state NMR results, oxygen is present in SiAlCN ceramics by form of "SiO_4" units) with the activation energy of 5.1 eV and the activation energy of "oxygen free" SiCN system was 3.41eV reported by Chen and co-works. We believe that the presence of oxygen restricts the crystallization (or sp^3-sp^2 transition) of free carbon and, thereby, increases the activation energy. The bonds between C and O were revealed XPS technique shown in Figure 4.6. The C-O-C or O-C (O)-O bands were observed by the superfine structure analysis of carbon XPS, which indicated that the oxygen does have some effect on the free carbon. Unfortunately, how the oxygen effects the conductivity of free carbon is still unknown further investigation is requieed.

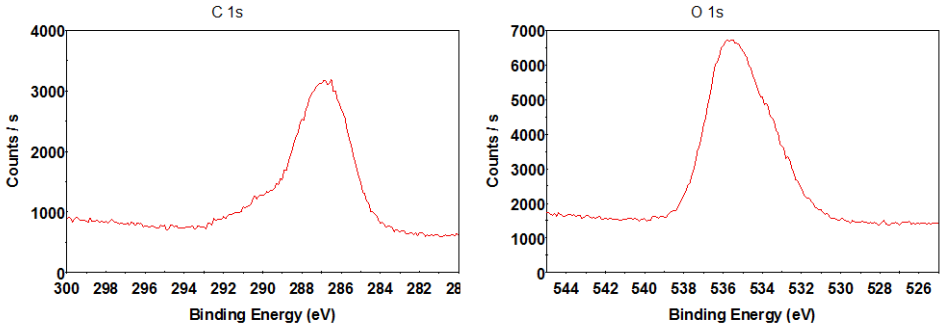

Figure 4.6 XPS results of SiAlCN ceramics sintered at 1000 °C.

The temperature dependence electric conductivity of 10ASB2DP SiAlCN ceramic sintered at 1000 °C was tested within the temperature range starting at room temperature to 500 °C. The high temperature conductivity characterization was carried out at the muffle furnace without any protect atmosphere and the silver paste as electrode.

Figure 4.7 shows the temperature dependent conductivity of 10ASB2DP sintered at 1000 °C SiAlCN ceramic with the test temperature up 500 °C (limited by the stable using temperature of silver electrode). As can be seen in Figure 4.7 the electric conductivity increases continually with increasing temperature. A significant increase, three orders of magnitude, was found from room temperature to 500 °C. This strong temperature dependence resistivity behavior suggests that the SiAlCN materials are promising for use as high temperature sensor.

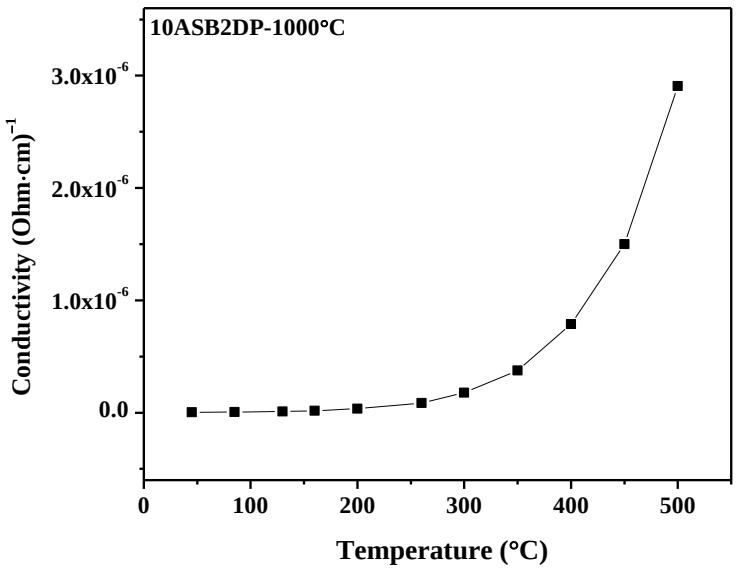

Figure 4.7 Temperature dependent conductivity of SiAlCN and SiCN ceramics.

There are mainly two possible conducting mechanisms: one is the semiconducting band-gap model which follows Arrhenius equation as shown in Eq. (4-1), and the other is called variable range hopping (VRH), which follows Mott's equation as shown in Eq. (4-2).

$$\sigma = \sigma_0 \exp\left[-\left(\frac{\Delta E}{kT}\right)\right] \quad \text{Eq. (4-1)}$$

$$\sigma = \sigma_0 \exp\left[\left(\frac{T_0}{T}\right)^{1/4}\right] \quad \text{Eq. (4-2)}$$

Where σ is conductivity, σ_0 is a pre-exponential factor, ΔE is the activation energy, the gap between the Fermi level and the energy state which the charge carriers are excited, and k is the Boltzmann constant. T_0 is given by:

$$T_0 = \frac{18.1\alpha^3}{kN(E_F)}$$

Where α is inverse of the localization length of the wave function for the excited electron, $N(E_F)$ is the density of the localized states around Fermi level.

In the semiconducting band-gap model, the conductivity is controlled primarily by the concentration of the mobile charge carriers which is a highly temperature dependent processing and determined by the activation energy. In contrast, for the VRH model, the charge carriers will jump back and forth one unoccupied state to another near the Fermi level; conductivity is determined by both hopping distance and activation energy.

The parameter $\frac{\Delta E}{\mathrm{kT}}$ determines the type of conducting mechanisms and thus, it follows that the parameter is very importants. If $\Delta E \gg KT$, then the electric conductivity is controlled by the semiconducting band-gap model, follows the Arrhenius equation; if the $\Delta E \ll KT$ the electric conductivity is followed the Mott's law.

The natural logarithm of conductivity with inverse of test temperatures (in Kelvin) was plotted in Figure 4.8 and the relative activation energies were calculated by curve fitting. It was found that the Arrhenius fit can be accommodated by two different activation energies of 0.57 eV and 0.23 eV for high and low temperature sections, respectively. Considering the values of KT in the testing temperature range, are 0.0026 eV at room temperature and 0.066 eV at 500 °C. Since, $\Delta E \gg KT$ is satisfied then it follows that the semiconducting band-gap conducting mechanism.

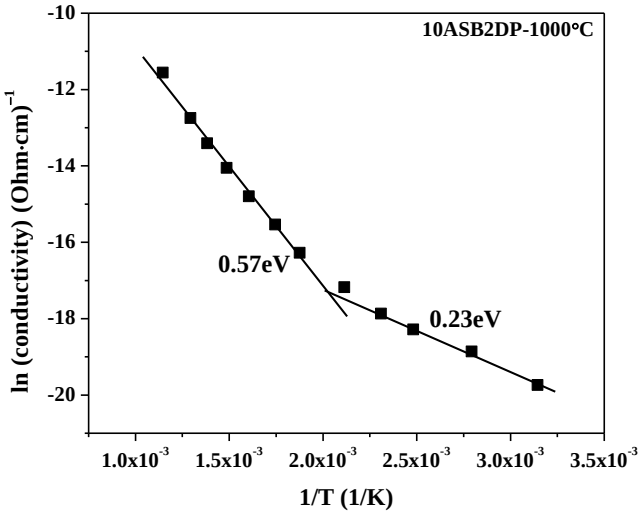

Figure 4.8 Plot of ln (conductivity) VS 1/T of SiAlCN at different test temperatures.

4.2.2 Dielectric properties of SiAlCN ceramics

Both the dielectric constant and loss were characterized for SiAlCN ceramics sintered at various temperatures (1000, 1100, 1200, 1300 and 1400 °C) using the Agilent E4980A within the frequency range between 20 Hz to 2 MHz. The dielectric constant and loss were calculated by the following equations.

$$\varepsilon^* = \frac{C^* d}{A\varepsilon_0} \qquad \text{Eq. (4-3)}$$

$$\tan\delta = \frac{\varepsilon''}{\varepsilon'} \qquad \text{Eq. (4-4)}$$

Where ε^* and C^* are the complex dielectric constant and capacitance, respectively. ε_o is the dielectric constant of free space; A and d are the electrode area and sample thickness. $\tan\delta$ is dielectric loss, ε'' and ε' are the image and real part of dielectric constant, respectively.

The results were plotted in Figure 4.9 and Figure 4.10, respectively. The dielectric constant and loss for SiAlCN ceramics sintered at different temperatures at specific frequencies (1, 10, 100 kHz and 1 MHz) were listed in Table 4.2 and plotted in Figure 4.11 and Figure 4.12. It was found that the dielectric constant and loss decreased with increasing frequency. The dielectric constant was higher at low frequency than that of high frequency because of the polarizations get enough time to response with the electric field at low frequencies; in contrast, the electric field at high frequencies allow only part of the polarizations to catch up with it, so the dielectric constant is smaller at high frequencies. The dielectric loss is caused by the energy

consumed of the motion/vibration of the polar (space charges, dipoles, ionics and electrons) with the electric field. At low frequencies, the motions/vibrations are all energy consuming processing but at high frequency only electronic polarization can catch up with the electric field consuming minimal or no energy. Therefor, the dielectric loss is smaller at high frequencies compared to that of low frequencies.

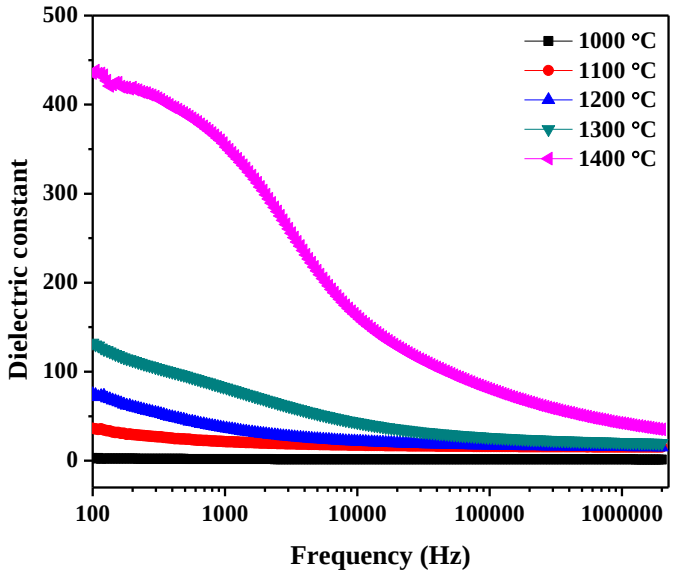

Figure 4.9 Frequency dependence of dielectric constants for SiAlCN ceramics sintered at different temperatures.

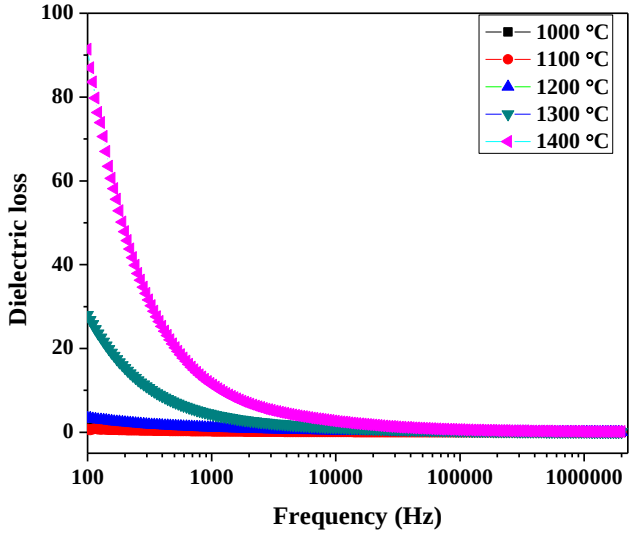

Figure 4.10 Frequency dependence of dielectric loss of SiAlCN ceramics sintered at different temperatures.

Table 4.2 Dielectric constants and loss of SiAlCN ceramics at different sintered temperatures and frequencies.

T(^{o}C)	Dielectric constant				Dielectric loss			
	1kHz	10kHz	100kHz	1MHz	1kHz	10kHz	100kHz	1MHz
1000	1.85	1.58	1.48	1.43	0.25	0.09	0.03	0.01
1100	21.55	17.46	16.06	15.53	0.37	0.12	0.04	0.02
1200	36.99	21.60	17.26	15.68	1.12	0.39	0.13	0.05
1300	82.93	43.23	26.40	20.95	4.44	1.20	0.39	0.14
1400	356.73	161.91	79.66	41.98	11.63	2.62	0.60	0.19

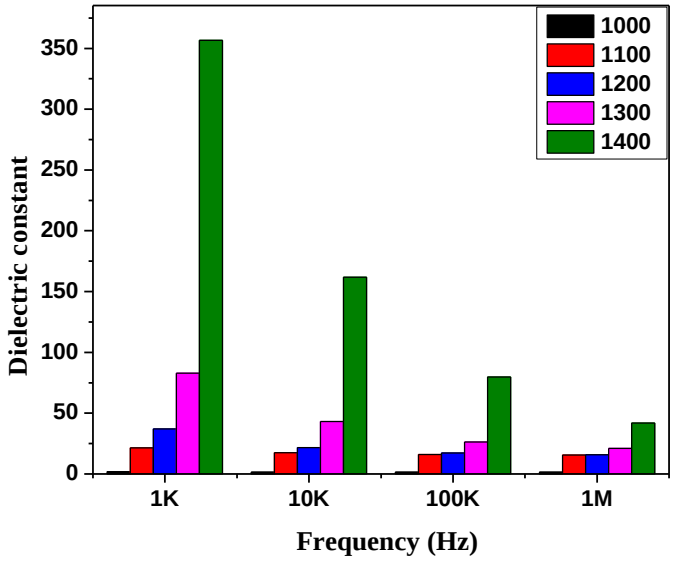

Figure 4.11 Dielectric constants of SiAlCN ceramics at specific frequency and various sintered temperatures.

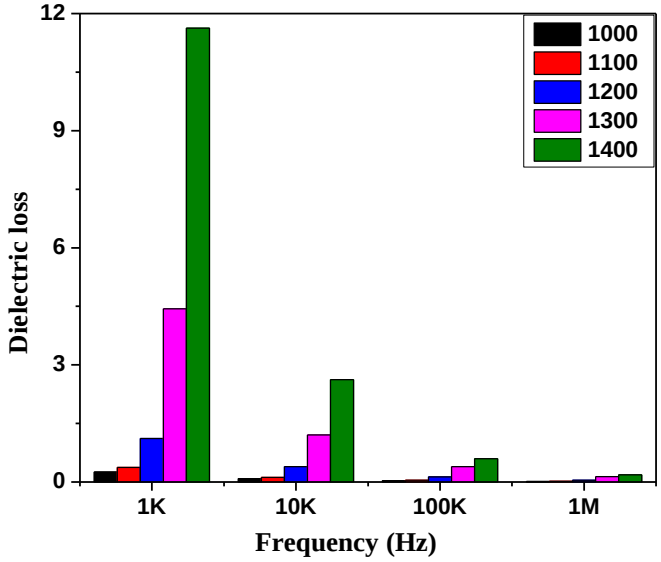

Figure 4.12 Dielectric loss of SiAlCN ceramics at specific frequency and various sintered temperatures.

As can be seen, the dielectric constant of SiAlCN ceramics sintered at 1400 °C is more than 300 times higher than that of the samples sintered at 1000 °C, which is a huge improvement. We believe that this huge improvement is due to the space charge

effect. The space charge is formed at the interface between the SiCN matrix and free carbon, as illustrated in Figure 4.13. The charge carriers disperse uniformly when there is no electric field (Figure 4.13 (a)). In contrast, the charge carriers separate and accumulate at the interface (Figure 4.13 (b)) when the external electric field is applied, the space charge is set up. The formed space charge established an inner electric field, opposite in direction to the external one and causing a dramatic increase in the dielectric constant. It is easy to understand that the more trapped charge carriers the larger of inner electric field and the higher dielectric constant can be observed. The trapped charge carriers within the samples sintered at 1400 °C were higher than that of the samples sintered at 1000. This means that the space charge effect will be stronger for 1400 °C samples than that of the samples sintered at1000 °C. This is the reason the dielectric constant of SiAlCN samples sintered at 1400 °C is observed to be much higher than that of 1000 °C samples at low frequencies.

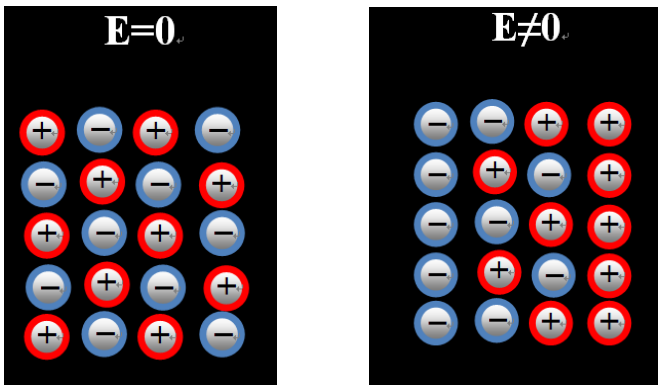

Figure 4.13 Schematic illustration of established space charge within SiAlCN system (a) without electric field (b) with electric field

As can be seen, the dielectric loss increases dramatically with increasing sintered temperature. This observation begs the question; does the dielectric loss truly cause

by the polarization? In order to determine the answer, the relationship between the conductivity and image part of the dielectric constant must be considered, as shown in Eq. (4-5).

$$\varepsilon'' = \frac{\sigma}{\omega\varepsilon_0} \qquad \text{Eq. (4-5)}$$

If we apply the logarithm on both sides of Eq. (4-5), we obtain in Eq. (4-6)

$$\log \varepsilon'' = \log\left(\frac{\sigma}{2\pi f \varepsilon_0}\right) = \log\left(\frac{\sigma}{2\pi\varepsilon_0}\right) - \log f \qquad \text{Eq. (4-6)}$$

Where σ is conductivity, f is frequency.

The logarithm of the imaginary part of the dielectric constant and the logarithm of the frequency should be linearly with a slope of 1, if the conducting behavior dominates to the imaginary part of dielectric constant. The results are plotted in Figure 4.14 and the linear fit results are shown in Figure 4.15. The slopes of the curve fitting results are listed in Table 4.3. The slopes increase from 0.56 to 1 gradually with sintering temperature range between 1000 °C and 1400 °C, indicating that with increasing sintered temperature the conducting behavior becomes more dominate, resulting in high dielectric loss. The results agree with the D.C. conductivity of SiAlCN ceramics very well (the D.C. conductivity increase with increasing the sintered temperature.)

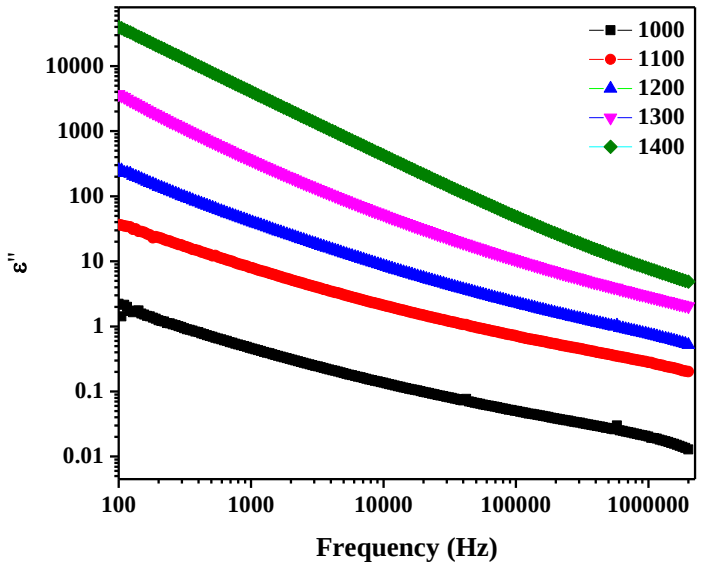

Figure 4.14 Dielectric loss of SiAlCN ceramics at specific frequencies and different sintered temperatures.

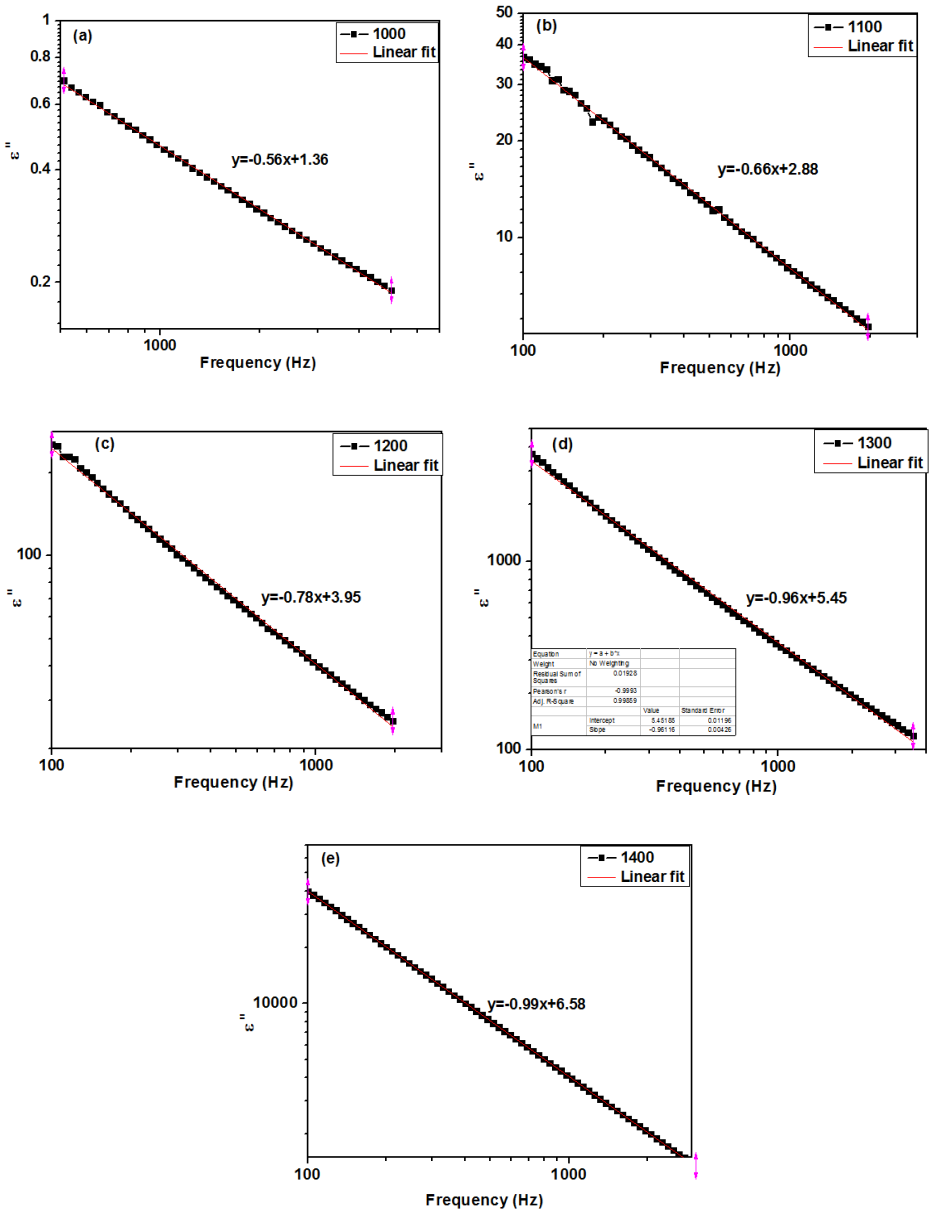

Figure 4.15 Dielectric loss of SiAlCN ceramics at specific frequency and different sintered temperatures.

Table 4.3 Slops of the linear fit of logarithm of the imaginary part of the dielectric constant and the logarithm of frequency of 10ASB2DP-SiAlCN ceramics.

T(°C)	1000	1100	1200	1300	1400
Slop	0.56	0.66	0.78	0.96	0.99

The temperature dependent dielectric constants and loss were measured by using the Agilent 4298A and a muffle furnace for heat up the samples. The frequency and

temperature range were 20 Hz - 2 MHz and room temperature to 450 °C, respectively. The temperature dependent dielectric constant and loss are shown in Figure 4.16 and Figure 4.17. It was found that the dielectric constant and loss both increased with increasing test temperature. The dielectric constant and loss became larger at low frequencies than that of at high frequencies, similar to the frequency dependent properties discussed above. The most polar (ions, atoms and electrons) will gain energy when the temperature increases, which in turn makes them in a high energy state (which means they are easier to move than that in the equilibrium state). These polar with higher energy cause higher polarization, therefore, the dielectric constant and loss increase with increasing temperature. The number of trapped charge carriers increase with increasing temperature, and the strong space charge effect could be observed when there are enough trapped charge carriers present. The impendence analysis of SiAlCN ceramics, tested at different temperature, reveal that the strong space charge effect were observed at the temperature around 400 °C, illustrated in Figure4.18. There was only one arc or semicircle (Figure4.18 (a) and (b)) before 400 °C and there was a small tail for the sample tested at 400 °C caused by the space charge effect.

Table 4.4: Temperature dependent dielectric constant and loss of 10ASB2DP SiAlCN ceramics sintered at 1000 °C.

T(°C)	Dielectric constant			Dielectric loss		
	10kHz	100kHz	1MHz	10kHz	100kHz	1MHz
50	10.52	9.64	9.24	0.13	0.047	0.018
150	13.45	10.63	9.70	0.46	0.138	0.046
250	19.90	12.27	10.22	1.18	0.362	0.106
350	29.16	15.27	11.02	2.71	0.816	0.227
450	35.54	20.61	12.44	8.03	1.693	0.481

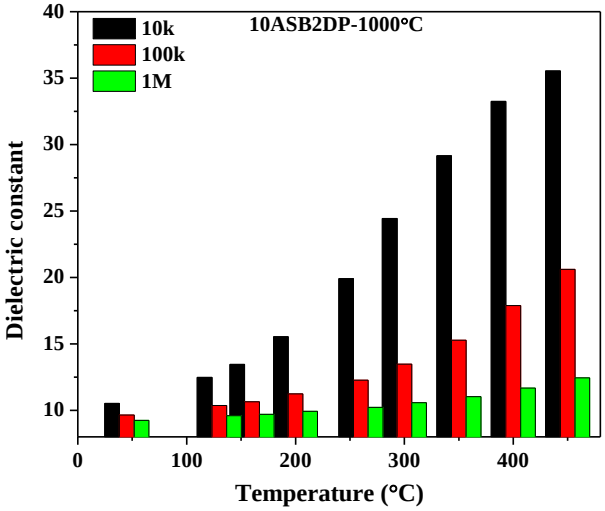

Figure 4.16 Temperature dependent dielectric constant of SiAlCN ceramics sintered at 1000 °C.

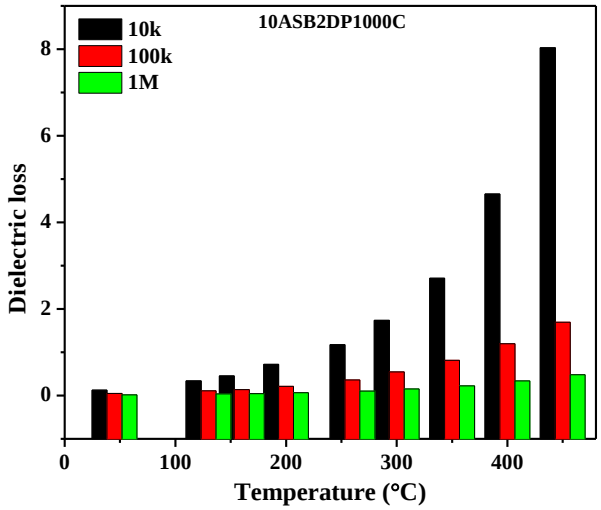

Figure 4.17 Temperature dependent dielectric loss of SiAlCN ceramics sintered at 1000 °C.

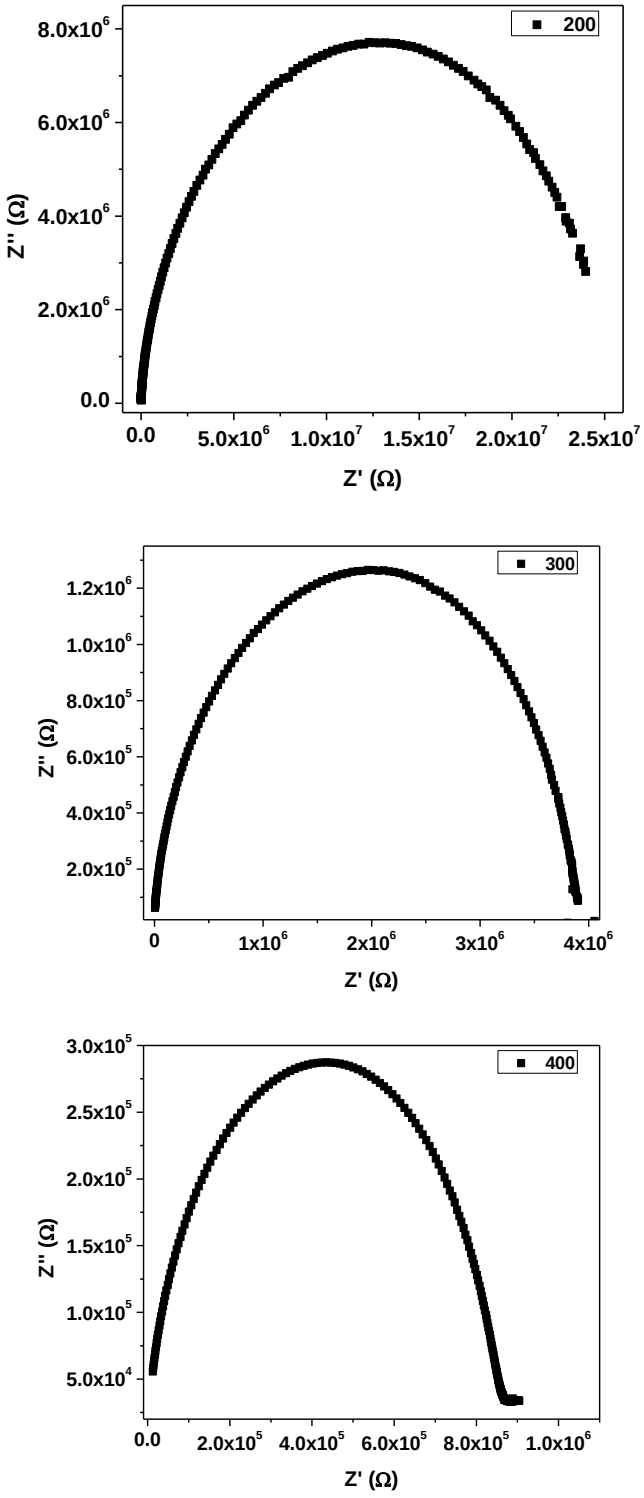

Figure 4.18 Complex impendence analysis of SiAlCN ceramics at different tested temperatures (a) 200 ^{o}C (b) 300 ^{o}C (c) 400 ^{o}C.

References:

1. J.C. Maxwell, A Treatise on Electricity and Magnetism, 2nd edn, Vol. 1, p435, Clarendon Press, Oxford.

2. L. Woo, S. Wansom, A.D. Hixson, M.A. Campo, and T.O. Mason, A universal equialent circuit model for the impedance response of composites, J. Mater. Sci., 38, 2265-2270, (2003).

3. A. C. Ferrari, S. E. Rodil, J. Robertson and W. I. Milne, "Is stress necessary to stabilise sp3 bonding in diamond-like carbon?" Diam. Relat. Mater., 11 [3–6], 994-999 (2002).

4. A. C. Ferrari, B. Kleinsorge, N. A. Morrison, A. Hart, V. Stolojan and J. Robertson, "Stress reduction and bond stability during thermal annealing of tetrahedral amorphous carbon," J. Appl. Phys., 85 [10], 7191-7197 (1999).

5. D. S. Grierson, A. V. Sumant, A. R. Konicek, T. A. Friedmann, J. P. Sullivan, and R. W. Carpick, "Thermal stability and rehybridization of carbon bonding in tetrahedral amorphous carbon," J. Appl. Phys. 107, 033523 (2010).

6. Yaohan Chen "STRUCTURE AND PROPERTIES OF POLYMER-DERIVED SiBCN CERAMICS"' University of Central Florida, PhD dissertation, (2012).

7. Tao Jiang "ELECTRONIC PROPERTIES AND MICROSTRUCTURES OF AMORPHOUS SiCN CERAMICS DERIVED FROM POLYMER PRECURSORS" University of Central Florida, PhD dissertation, (2009).

CHAPER FIVE: HIGH TEMPERATURE SENSOR FABRICATION AND CHARACTERIZATION

Temperature has to be monitored to prevent damage of devices and improve performance in high temperature and harsh environments in many applications, for example, gas turbines, nuclear reactors, high speed vehicles and automotives. However, fabrication of such sensors faces a huge technical challenge. The major hurdle is that the sensors must survive harsh environments, including high temperatures, high stress, corrosive species and/or radiation. In addition, the sensor materials must maintain specific properties at high temperatures in order to provide means for sensing; they must do so in an easy-to-microfabricate manner in order to lower costs. These requirements basically prevent the use of most available sensors[1-7]. Recently, polymer-derived ceramics (PDCs) have been considered suitable materials for making high-temperature microelectromechanical systems (MEMS)/micro-sensors[8]. Previous studies revealed that PDCs, synthesized from the thermal decomposition of polymeric precursors, exhibit excellent thermomechanical properties, such as high thermal stability[9,10], high oxidation/corrosion resistance[11-15] and high temperature multifunctionalities[16,17].

This chapter will discuss the high temperature sensor fabrication, Whetstone bridge circuit design and sensor test by using the SiAlCN ceramics basing on their temperature dependence resistance properties.

5.1 Polymer derived SiAlCN sensor fabrication

The fabrication procedure of polymer derived temperature sensor is demonstrated by using the 10ASB2DP-1000°C SiAlCN sample. The micro-machining technique is for sensor and the basic procedures are shown in Figure 5.1 and illustrated as following:

(1) A hydraulic laboratory press (Automatic 4533, Carver, Inc., Wabash, IN) was used to crosslinked SiAlCN precursor (infusible polymer) to a disk shape (green body) with the dimension of Φ12.5mm in diameter and 4~6 mm in thickness. The green body was heat treated at 200 °C for 24 hours in the oven.

(2) A precision CNC dicing/cutting diamond saw (SYJ-400, Richmond, CA) was used to cut a rectangular SiAlCN sensor head (polymer state) from the green body mentioned in step (1).

(3) Two holes were drilled on top of the sensor head achieved in step (2) with the diameter of ~350 μm and ~1.5 mm in depth by applying the micro machining technique.

(4) Liquid SiAlCN precursor was infiltrated into the two holes under a vacuum.

(5) Pt wires were fed into the manufactured holes and crosslinked at 80 °C for 24 hours in order to to hold the Pt wires.

(6) The as-received sensor head with Pt wires was pyrolyzed at 1000 °C for 4 hours to obtain a SiAlCN ceramic sensor (with Pt wires). The Overall size of the assembled sensor is 3.4mm×2.7mm×1.2mm, shown in Figure 5.1 (b)

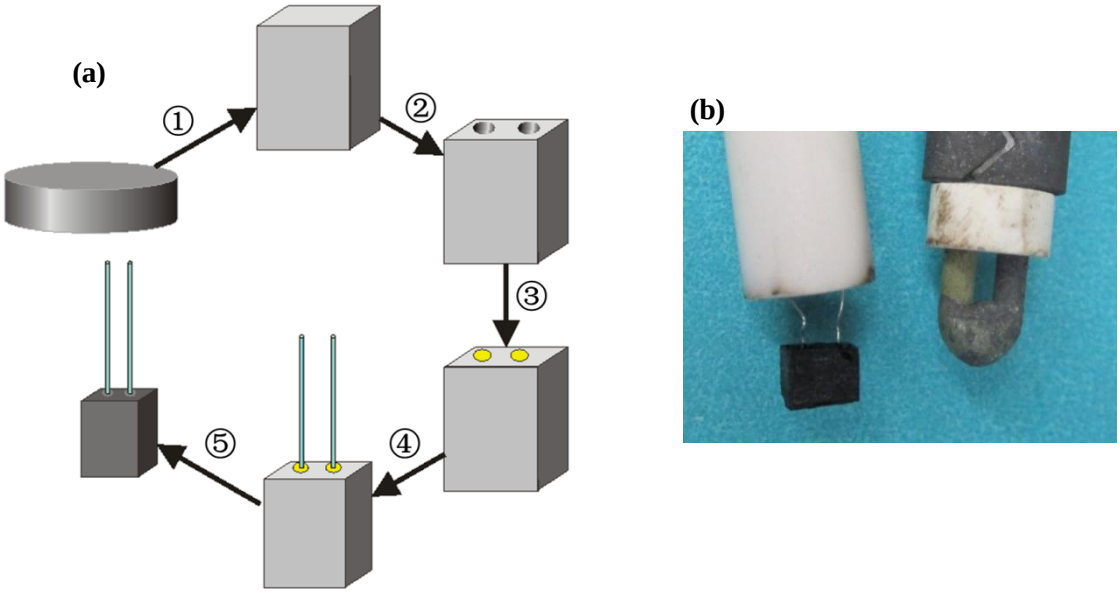

Figure 5.1 (a) SiAlCN ceramic sensor fabrication procedure and (b) optical image of sensor.

There are two key factors that should be mentioned here. First and foremost, the heat treatment process of the green body is required to make it strong enough to sustain micro-machining. Secondly, the size of the hole for the Pt wire needed to be selected carefully; this is due to the natural shrinkage (~22%) of the SiAlCN ceramics during the pyrolysis and inversely. Inversely, the Pt wire will expand at the same time so optimal parameters concerning the hole size must be determined. If the precursor layer in between the Pt wire and sensor head is too thin (the case of small hole), there will not be enough bonding force to hold the Pt wire; as a result the Pt wire will fall off (extreme situation: no precursor layer). If the precursor layer is too thick (the case of big hole), the ceramic sensor will be broken by the tension stress from the expansion of the Pt wire (extreme situation: Pt wire sounded by precursor only). Therefore, the thickness of the precursor (or the size of the hole) should be carefully selected in order to get a good bonding but not break the ceramic sensor. In this case

the hole, with diameter of ~350 μm was proved to be sufficient. Figure 5.2 shows the SEM images of the Pt wire bonding of SiAlCN sensor. As we can see in Figure 5.2 (a) the sensor head cracked due to the tension force from Pt wire and Figure 5.2 (b) indicated a very good bonding between the Pt wire and ceramic sensor head.

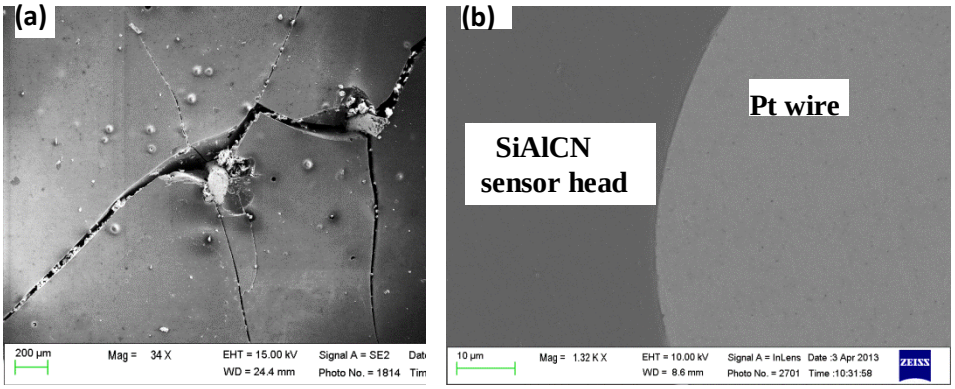

Figure 5.2 SEM images of Pt wire bonding of the ceramic sensor head.

5.2 Wheatstone bridge circuit design and analysis

A Wheatstone bridge is an electrical circuit used to measure an unknown electrical resistance by balancing two legs of a bridge circuit, one leg of which includes the unknown component; invented by Samuel Hunter Christie in 1833 and improved and popularized by Sir Charles Wheatstone in 1843. The principle of the circuit is that if three out of four resistances are known, and current in the cross branch is zero, the fourth resistance could be determined. This experimental setup, the Wheatstone circuit shown in Figure 5.3, was applied for the temperature sensor measurement. Where R_1, R_2 and R_3 are standard resistors and R_x is the SiAlCN ceramic sensor.

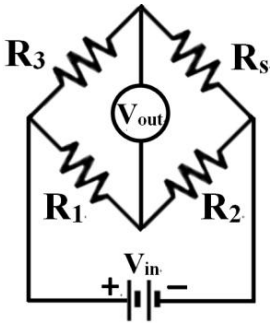

Figure 5.3 A schematic drawing of a typical Wheatstone bridge circuit.

The voltage difference from point B and D is the sensor output, V_{out}, the external voltage, V_{in}, is applied voltage between point A and C. The resistance of the ceramic sensor will be changed when the temperature changed. This resistance change will cause a varied and detectable V_{out}. Therefore, V_{out} can be described by the following Equation.

$$V_{\text{out}} = \left(\frac{R_3}{R_3 + R_x} - \frac{R_1}{R_1 + R_2} \right) V_{\text{in}} \qquad \text{Eq. (5-1)}$$

Normally, the standard resistors of R_1 and R_2 are set to be equal in order to make the circuit simple. Therefore the resistance relationship of matching resistor R_3 and ceramic sensor is quite important. The sensitivity of the sensor can be derived for Eq. (5-1) by taking the first derivation shown in Eq. (5-2).

$$\frac{dV_{\text{out}}}{dT} = \left[\frac{R_3 V_{\text{in}}}{\left(R_3 + R_x \right)^2} \right] \frac{dR_x}{dT} \qquad \text{Eq. (5-2)}$$

It is clear that the sensor sensitivity can be determined by two terms. The first term is related to R_3 and R_x, and the second term is purely related to the sensor

property of temperature dependent resistivity. In order to get good sensitivity, these two parts must to be considered. First, the second part of Eq. (5-2) will be discussed.

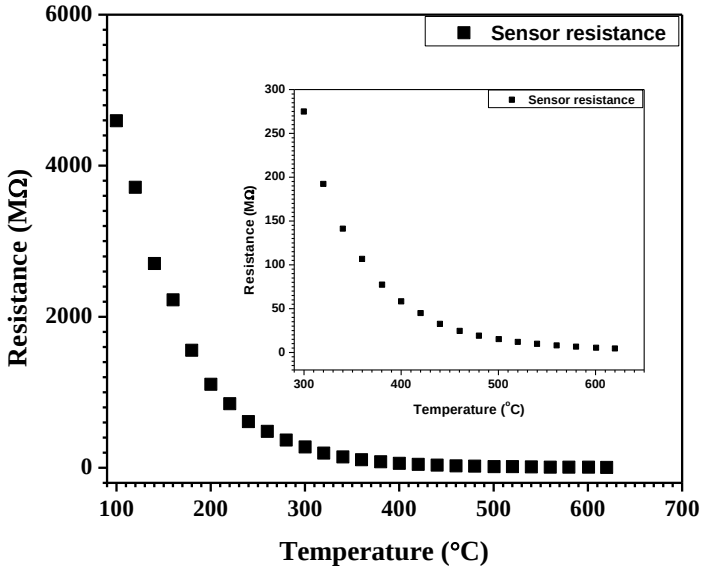

Figure 5.4 The sensor resistance changes with temperature (the imbedded plot shows the high temperature range).

The sensor resistance changes with temperature depicted in Figure 5.4. It was found that sensor resistance, in a fairly large range from 4592 MΩ to 4.42 MΩ, continues to decrease as temperature change from room temperature to 600 °C. Based on the previous results, the conducting mechanism is semiconducting band-gap model, which follows Arrhenius equation, shown in Eq. (5-3). Combining with Ohm's law ($R = \rho\frac{L}{S}$) and applying the natural logarithm, allows us to obtain Eq. (5-4); indicating that ln(1/R) VS (T^{-1}) should have a linear relationship and the result is plotted in Figure 5.5.

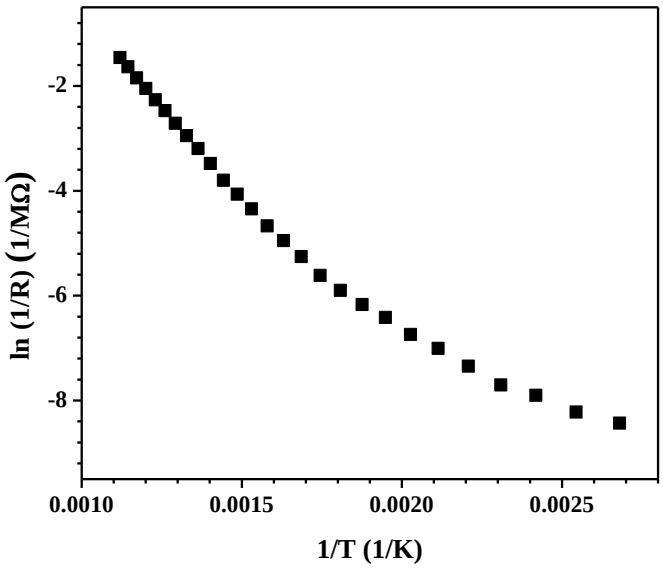

Figure 5.5 The plot of sensor resistance (ln(1/R) with inverse of the measured temperature (T^{-1}).

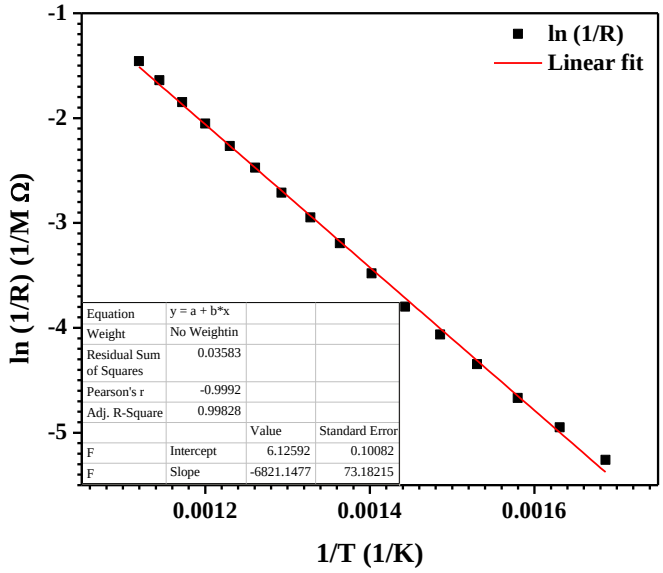

Figure 5.6 Linear fitting of sensor resistance (ln(1/R)) versus measured temperature (T^{-1}) at high temperature range.

A very good linear relationship at high temperature was observed which in turn proves the previous conclusion that the semiconducting band-gap conduction mechanism of SiAlCN ceramics holds true.

$$\sigma = \sigma_0 \exp\left[-\left(\frac{\Delta E}{kT}\right)\right] \quad \text{Eq. (5-3)}$$

$$\ln\frac{1}{R_x} = \ln\sigma_0' - \left(\frac{\Delta E}{kT}\right) \quad \text{Eq. (5-4)}$$

Where $\sigma_0' = \ln\sigma_0 - \ln\frac{l}{s}$, σ_0 is the coefficient, L and S are the length and electrode area of the ceramic sensor.

The high temperature range between 300 and 600°C is the target range of this study. The linear fitting result at this temperature range is shown in Figure 5.6. The slop and intercept are –6821.15 and 6.126, respectively. Then the Eq. (5-4) becomes Eq. (5-5). The dR/dT can be achieved considering the first deviation of Eq. (5-5), as shown in Eq. (5-6) and then the dR/dT is illustrated in Eq. (5-7).

$$\ln\frac{1}{R_x} = 6.126 - 6821.15\left(\frac{1}{T}\right) \quad \text{Eq. (5-5)}$$

$$\frac{dR_x}{dT} = \frac{-6821.15}{T^2}R_x \quad \text{Eq. (5-6)}$$

Combining with $R_x = \exp\left(\frac{6821.15}{T} - 6.126\right)$

We can get

$$\frac{dR_x}{dT} = \frac{6821.15}{T^2}\exp\left(\frac{6821.15}{T} - 6.126\right) \quad \text{Eq. (5-7)}$$

The result shown in Figure 5.7 is valid for the temperature range between 320~ 620°C. It can be seen that the dR/dT decreases with increasing temperature, which means the sensor sensitivity will decrease with increasing temperature and only if this

feature is taken into account. There is another part that will affect the sensor sensitivity shown in the first term of Eq. (5-2).

We assume the first part of Eq. (5-2) is a function of $F_{(R3)}$ as shown in Eq. (5-8)

$$F_{(R_3)} = \frac{R_3}{\left(R_3 + R_x\right)^2} \qquad \text{Eq. (5-8)}$$

The first derivave of $F_{(R3)}$ is shown in Eq. (5-9)

$$\frac{dF_{(R_3)}}{dR_3} = \frac{R_3 - R_x}{\left(R_3 + R_x\right)^3} \qquad \text{Eq. (5-9)}$$

From Eq. (5-9), we can see that when R_3=R_x, $F_{(R3)}$ has a maximum value, which means the sensor will have maximum sensitivity at this point (by considering this factor only). In another words, the sensor will get maximum sensitivity when balance resistance R_3 matched the senor resistance R_x. Four specific R_x values were selected as a example and plotted with the normalized R_3/R_x as shown in Figure 5.8. It was found at first, the $F_{(R3)}$ increased with increasing R_3/R_x and reached the maximum value at R_3/R_x=1 and then decreased afterwards. Results indicate that the maximum value of $F_{(R3)}$ increases with decreasing sensor resistance R_x. This means smaller sensor resistance will be helpful to achieve better sensitivity shown in Figure 5.9.

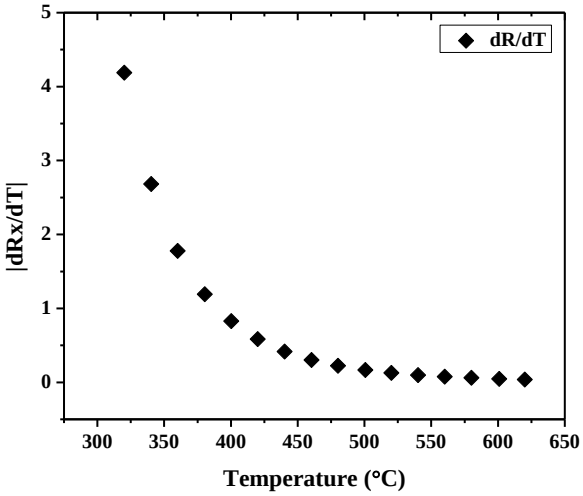

Figure 5.7 Plot of dR/dT VS test temperatures.

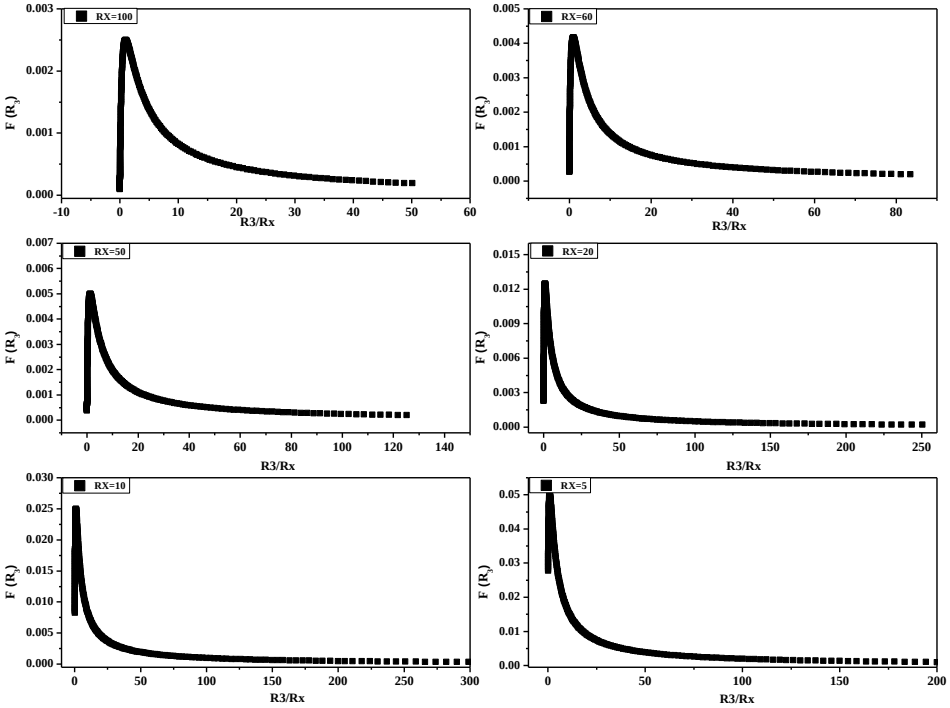

Figure 5.8 $F_{(R3)}$ changes with normalized R_3/R_x at different sensor resistance R_x.

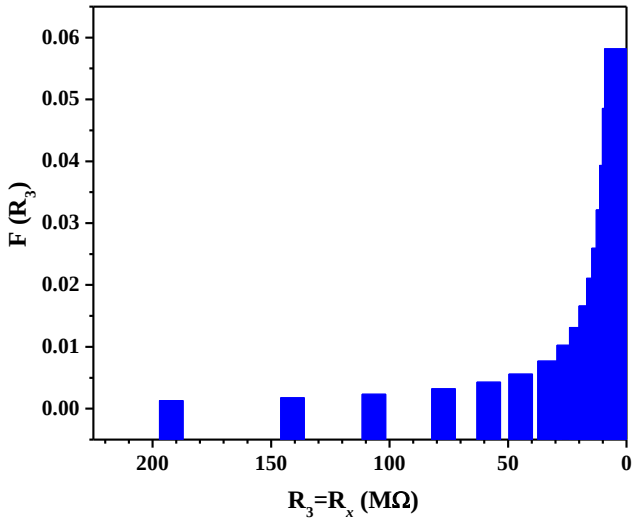

Figure 5.9 Maximum $F_{(R3)}$ change with different sensor resistances R_x.

Therefore, the maximum sensitivity dV/dT can be calculated using Eq. (5.2) with the input voltage of 5 V at each temperature point, as shown in Figure 5.10. The maximum sensitivities change from 27.5 mV/K to 11.3 mV/k in the temperature range between 320~ 620 °C, which are better than most reported ceramic temperature sensors.

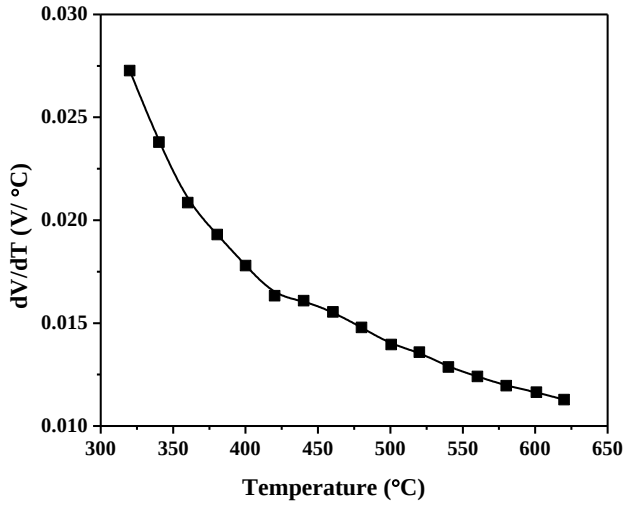

Figure 5.10 The maximum sensitivity dV/dT at different temperatures (V_{in} = 5 V).

By considering the whole temperature range, the balance resistor of R_3=30 MΩ was picked in order to match the sensor resistance R_x at the middle temperature. The simulated sensitivity, shown in Figure 5.11, first increases from the temperature between ~320 °C to ~440 °C and then decreases afterward. The maximum sensitivity appears around 440 °C of 15.5 mV/K, corresponding to the sensor resistance of 32MΩ. This result is in agreement with the previous conclusion: the closer R_3 and R_x, the higher sensitivity.

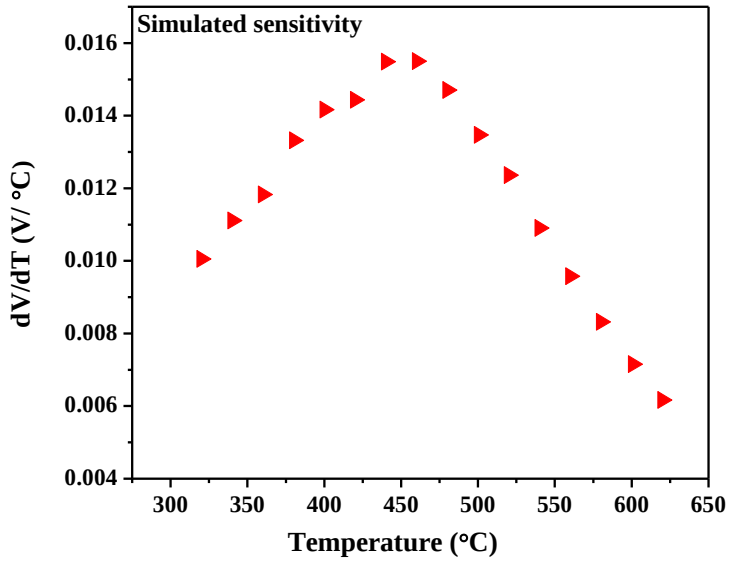

Figure 5.11 Simulated sensitivity dV/dT at various test temperatures (R_3=30 MΩ V_{in} = 5V).

The sensor output voltage is calculated by using the Eq. 5-1 and parameters of R_3=30 MΩ, V_{in}=5 V, R_1= R_2, the result is plotted in Figure 5.12. In this figure, we can see that the output voltage increase from –2.577 V to 1.159 V with the temperature range between 300 °C to 600 °C.

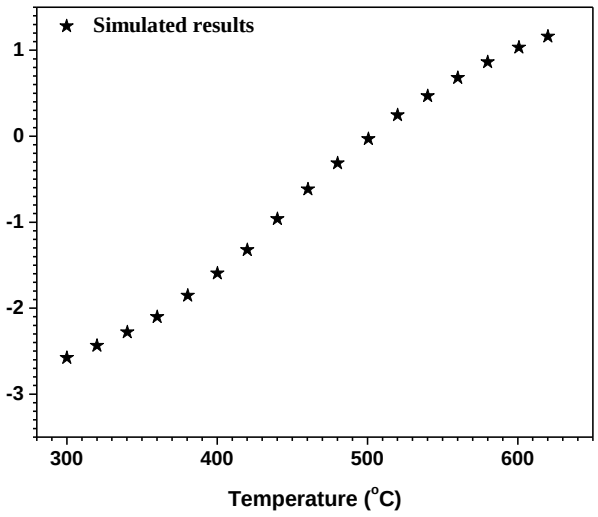

Figure 5.12 Calculated sensor output voltage versus temperature (R_3=30 MΩ, V_{in}= 5 V, R_1=R_2).

5.3 SiAlCN ceramic sensor test and results discussion

The as-received SiAlCN ceramic sensor was tested using the set up depicted in Figure 5.13. The set up composes of DC power supply (0-30V, HY 3002, RSR electronics, Inc, NJ), PXI* (National Instrument, Austin, TX), ADC (National Instrument, Austin, TX), tube furnace and a Wheatstone bridge circuit. The Wheatstone bridge circuit is connected as illustrated in Figure 5.3, where R_1= R_2= 22 MΩ, R_3= 30 MΩ, V_{in}= 5 V. A capacitor was put into the circuit considering as a low pass filter at the ends close to the output branch.

* PXI is a rugged PC-based platform for measurement and automation systems. PXI combines PCI electrical-bus features with the modular, Eurocard packaging of CompactPCI and then adds specialized synchronization buses and key software features. PXI is both a high-performance and low-cost deployment platform for applications such as manufacturing test, military and aerospace, machine monitoring, automotive, and industrial test [http://www.ni.com/pxi/whatis/].

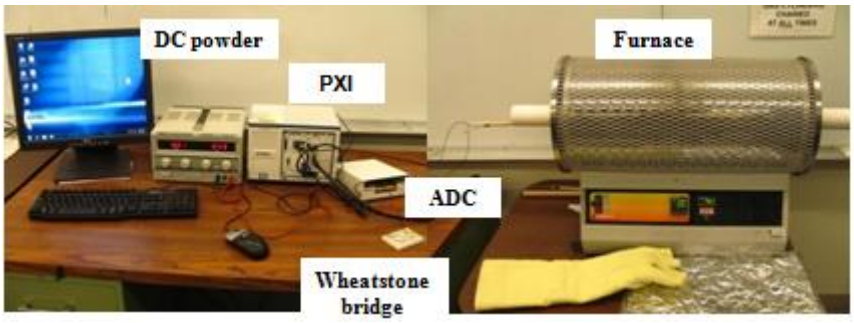

Figure5.13 SiAlCN sensor test set up and Wheatstone bridge circuit.

Before focusing on the sensor test, it is imperative to understand the effect of capacitor as a low pass filter. The capacitor filter is one of the most simple and common low pass filters commercially available. The relationship of the cutoff frequency, effect resistance of the circuit and capacitance are satisfied with the following equation of $\frac{1}{2\pi f} = R_{eff}C$, where f, R_{eff} and C are the cutoff frequency, effect resistance of the circuit and capacitance, respectively. It is clear that the larger capacitance the smaller cutoff frequency and the better signal to noise ratio. In this case the capacitance is selected of 1 μF. And a smooth and low noise single was achieved as the blue line shown in Figure 5.14.

The sensor performance was tested using the facilities mentioned above shown in Figure 5.14. It can be seen that output voltage increases with increasing temperature and the quality of the signal is rather smooth against very small noise. In order to show a direct relationship between test temperature and output voltage, the output voltage versus temperature is plotted in Figure 5.15. The results reveal that

output voltage increases nonlinearly with increasing temperature. This phenomenon is due to the intrinsic conducting mechanism of the SiAlCN ceramics. As discussed previously, the SiAlCN ceramic is an amorphous semiconductor with three possible conducting mechanisms, It was determined previously, that the resistance change with temperature should not linearly correlate and in turn implies that the output voltage here is also nonlinear. In Figure 5.15 it can be observed that the calculated output voltage, indicating by "*" , is agreement with the test results, approving a satisfactory sensor design has been obtained.

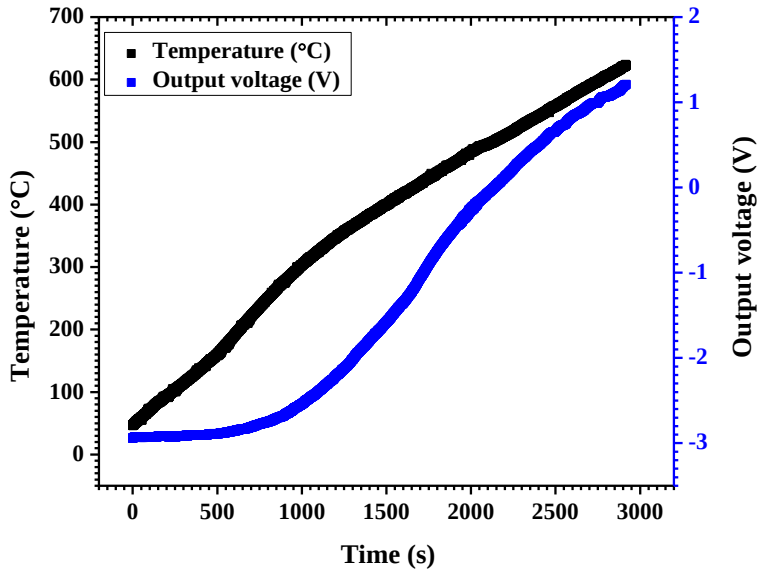

Figure5.14 SiAlCN ceramic sensor output voltage and thermal couple reading VS time.

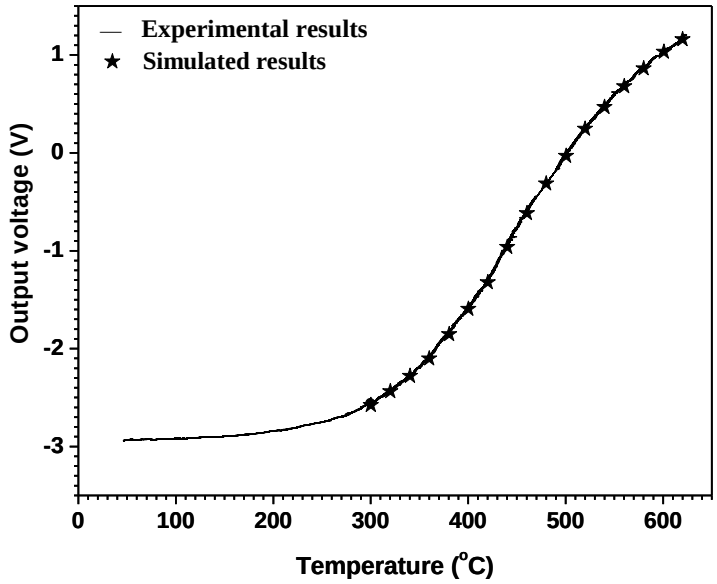

Figure 5.15 SiAlCN ceramic sensor output voltage (simulated and tested results).

The durability test of SiAlCN sensor was carried out by maintaining the temperature of the sensor constant at ~510 °C for more than 2 hours to observe the change in output voltage shown in Figure5.16. It was found that the output voltage remains constant until 30 min (V_{out}=1.00V) and then decreases gradually afterward by 0.02, 0.04 and 0.07 V for 1, 1.5 and 2 hours, respectively. This kind of drilling is common if using capacitor as a low pass filter. The possible reason is because the capacitor might be heated up during the test due to large current in the capacitor branch. The capacitance changed because of the increasing temperature of capacitor. A possible solution may include the use of a high quality capacitor or use of a low pass filter instead of the capacitor.

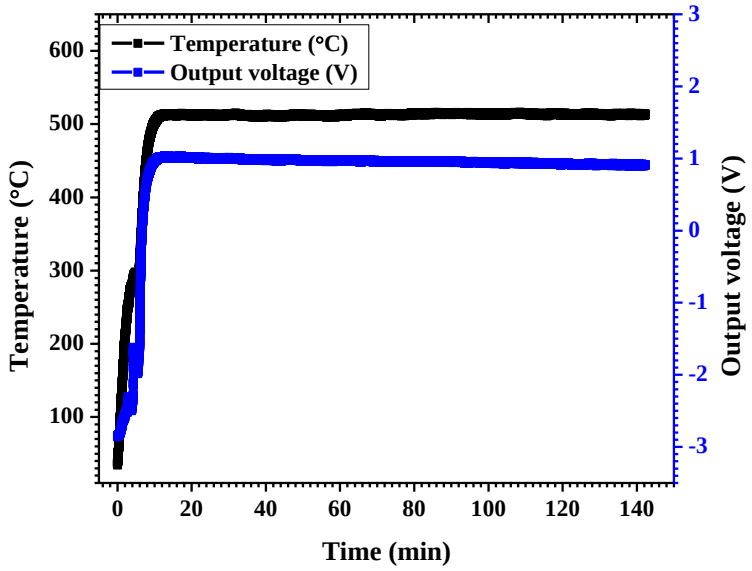

Figure5.16 Durability test of SiAlCN ceramic sensor.

References:

1. Salah, T.B., S. Khachroumi, and H. Morel, Characterization, Modeling and Design Parameters Identification of Silicon Carbide Junction Field Effect Transistor for Temperature Sensor Applications. Sensors, 2010. **10**(1): p. 388-399.
2. Yang, J., A Silicon Carbide Wireless Temperature Sensing System for High Temperature Applications. Sensors, 2013. **13**(2): p. 1884-1901.
3. Wieczorek, G., et al. SiC Based Pressure Sensor for High-Temperature Environments. in Sensors, 2007 IEEE. 2007.
4. Millan, J., et al. Electrical performance at high temperature and surge current of 1.2 kV power rectifiers: Comparison between Si PiN, 4H-SiC Schottky and JBS diodes. in Semiconductor Conference, 2008. CAS 2008. International. 2008.
5. O''Brien, H., et al. Evaluation of Si and SiC SGTOs for High Action Army Applications. in Electromagnetic Launch Technology, 2008 14th Symposium on. 2008.
6. Sheikh, M. and N.A. Riza, Direct measurement high resolution wide range extreme temperature optical sensor using an all-silicon carbide probe. Opt. Lett., 2009. **34**(9): p. 1402-1404.
7. Yonekubo, S., K. Kamimura, and Y. Onuma. Resistance-temperature Characteristics Of Polycrystalline Sic/diamond Structure. in Solid-State Sensors and Actuators, 1995 and Eurosensors IX.. Transducers '95. The 8th International Conference on. 1995.

8. Liew, L.A., et al., Fabrication of SiCN ceramic MEMS using injectable polymer-precursor technique. Sensors and Actuators a-Physical, 2001. **89**(1-2): p. 64-70.

9. Riedel, R., et al., A silicoboron carbonitride ceramic stable to 2,000 degrees C. Nature, 1996. **382**(6594): p. 796-798.

10. Wang, Z.C., F. Aldinger, and R. Riedel, Novel silicon-boron-carbon-nitrogen materials thermally stable up to 2200 degrees C. Journal of the American Ceramic Society, 2001. **84**(10): p. 2179-2183.

11. An, L.N., et al., Silicoaluminum carbonitride with anomalously high resistance to oxidation and hot corrosion. Advanced Engineering Materials, 2004. **6**(5): p. 337-340.

12. Wang, Y.G., et al., Polymer-derived SiAlCN ceramics resist oxidation at 1400 degrees C. Scripta Materialia, 2006. **55**(4): p. 295-297.

13. Wang, Y.G., et al., Oxidation of polymer-derived SiAlCN ceramics. Journal of the American Ceramic Society, 2005. **88**(11): p. 3075-3080.

14. Wang, Y.G., W.F. Fei, and L.N. An, Oxidation/corrosion of polymer-derived SiAlCN ceramics in water vapor. Journal of the American Ceramic Society, 2006. **89**(3): p. 1079-1082.

15. Bharadwaj, L., et al., Oxidation behavior of a fully dense polymer-derived amorphous silicon carbonitride ceramic. Journal of the American Ceramic Society, 2004. **87**(3): p. 483-486.

16. Zhang, L.G., et al., A silicon carbonitride ceramic with anomalously high piezoresistivity. Journal of the American Ceramic Society, 2008. **91**(4): p. 1346-1349.

17. Ramakrishnan, P.A., et al., Silicoboron-carbonitride ceramics: A class of high-temperature, dopable electronic materials. Applied Physics Letters, 2001. **78**(20): p. 3076-3078.

CHAPTER SIX: CONCLUSION

Based on the discussion aforementioned, the following conclusions can be noted:

1. SiAlCN ceramics were synthesized using liquid precursor of polysilazane (HTT1800) and aluminum-sec-tri-butoxide (ASB) as starting materials and dicumyl peroxide (DP) as thermal initiator. The amorphous structure of as-received ceramics is able to sustain to high temperatures (1500 °C) without large scale crystallization. The solid-state NMR indicates that SiAlCN ceramics have the SiN_4, SiO_4, $SiCN_3$, and AlN_5 units. The Raman spectra reveals that SiAlCN contains "free carbon" with the two specific peaks of "D" bond and "G" band at 1350 cm^{-1} and 1600 cm^{-1}, respectively. The "free carbon" becomes more and more ordered with the increasing pyrolysis temperature. The EPR results show that defects in the SiAlCN ceramic were related to carbon with a g-factor of 2.0016 ± 0.0006. Defect concentration decreases with increasing sintered temperature indicating that the degree of ordering of free carbon increases with increasing temperature, which is consistent with the Raman spectra.
2. The electric and dielectric properties of SiAlCN ceramics were characterized. The D.C. conductivity of SiAlCN ceramics increased with increasing sintered temperature and the activation energy was about 5.1 eV, higher than that of SiCN ceramics due to the presence of oxygen. The temperature dependent conductivity indicates that the conducting mechanism is semiconducting band-gap model and follows Arrhenius equation with two different sections of activation energy of

0.57 eVand 0.23 eV. The temperature dependent conductivity makes the SiAlCN ceramic suitable for high temperature sensor applications. The dielectric properties were carried out by using Agilent 4298A LRC meter. The results show the dielectric constant and loss increase with increasing temperature and the dielectric loss was dominated by the increasing of conductivity of SiAlCN ceramics at high sintered temperature.

3. The SiAlCN ceramic sensor was fabricated by using the micro-machining method. High temperature wired bonding issue was solved by the integrity embed method (IEM). It was found that the micro-machining method is promising and cost-effective way to fabricate PDC high temperature sensor and the IEM is satisfied to solve the high temperature wire bonding problem with clear bonding interface between the SiAlCN sensor head and the Pt wires. The Wheatstone bridge circuit was well designed by considering the resistance relationship between the matching resistor and the SiAlCN sensor resistor. It was found that the maximum sensitivity can be achieved when the resistance of matching resistor is equal to the SiAlCN sensor. The as-received SiAlCN ceramic sensor was tested up to 600 °C with the relative output voltage changing from -3.932 V to 1.153 V. The results indicated that the output voltage is nonlinear with the temperature change; the test sensor output voltage is consistent with simulated results. The durability test was carried out at 510 °C for more than two hours. It was found that the output voltage

remains constant for the first 30 min and then decreases gradually afterward by 0.02, 0.04 and 0.07 V for 1, 1.5 and 2 hours.

In summary, SiAlCN ceramics are synthesized with excellent thermomechanical properties, such as high thermal stability, high oxidation/corrosion resistance and high temperature multifunctionalities. SiAlCN ceramic high temperature sensors have been fabricated and characterized at high temperatures up to 600 °C. The results indicate that the SiAlCN ceramic sensor is suitable for high temperature and harsh environment application.

APPENDIX –A: CERAMIC NANOCOMPOSITES REINFORCED WITH HIGH VOLUME FRACTION OF CARBON NANOFIBERS

Carbon nanofiber (CNF) reinforced polymer-derived silicon carbonitride (SiCN) ceramic nanocomposite was fabricated by infiltrating CNF preform with liquid-phased polymeric preceramic precursor following by pyrolysis. The composite shows a very dense structure with a very high CNF concentration of 20 vol.%. The mechanical properties were investigated by a microindentation technique. It is found that the fracture mechanisms include crack branching, CNF bridging and CNF pullout, which lead to the increase in the fracture energy of the nanocomposite as compared to the monolithic SiCN. The indentation results also show that the indentation hardness of the CNF-reinforced SiCN-nanocomposite is smaller than that for the monolithic SiCN, indicating local softening of the nanocomposite.

1. **Introduction**

One-dimensional carbon nanostructures (e.g. nanotubes, nanowires and nanofibers) have attracted extensive attentions due to their unique and often superior properties as compared to bulk materials, thus promising for widespread applications. For example, it has been demonstrated that carbon nanotubes (CNTs) possess strength as high as 60 GPa [1, 2] and elastic modulus of the order of 1-5 TPa [3-6]. Depending on the diameters and orientations of their hexagons with respect to the tube axis, CNTs can be either semiconducting or metallic [7, 8]. The axial thermal conductivity of CNTs is even higher than that of diamond [9]. It has also been demonstrated that the strength and elastic modulus of silicon carbide (SiC) nanowires are also much higher than those measured from bulk SiC [10]. While previous studies on one-

dimensional nanostructures were primarily focused on using them for a verity of nano-devices, another equally important application of these materials is to make multifunctional nanocomposites. It is expected that this new class of nanocomposites could exhibit significantly improved mechanical as well as functional properties.

Application of one-dimensional nanostructures for ceramic matrix nanocomposites has been attempted in the last decade or so, with the focuses on using carbon nanotubes as the reinforcing phase. Majority of previous works synthesized the nanocomposites by sintering the mixtures of CNTs and ceramic powder [11-13] or ceramic powders with in-situ grown CNTs [14, 15]. The drawback of this technique is that the uniform dispersion of CNTs in ceramic matrix is difficult to achieve. More recently, CNT-ceramic nanocomposites were prepared by using polymer-derived ceramic processing, in which the CNTs were first mixed with liquid-phased pre-ceramic precursor followed by pyrolysis at elevated temperatures [16]. While the relatively uniform dispersion of CNTs has been achieved, this technique cannot be used to synthesize nanocomposites with high CNT concentrations.

In this work, we report a novel technique which can be used to synthesize ceramic matrix nanocomposites reinforced with high concentration and uniformly dispersed one-dimensional nanostructures. In this technique, one-dimensional

nanostructures were first made into a preform. The preform was then infiltrated with liquid-phased pre-ceramic precursor followed by pyrolysis. While carbon nanofibers (CNFs) are used as the reinforcing phase in this work, the technique developed can be used for other one-dimensional nanostructures.

2. Experimental Procedures

Commercially available carbon nanofiber (PR-19, Pyrograf Products, Inc. Cedarville, OH) with a diameter of ~100 nm and a length of 30-100 μm and a liquid-phased polysilazane (VL20, Kion, Huntingdon Valley, PA) were used as the starting materials; and poly (solium-4 styrene-sulfonate) (PS4SS, Sigma-Aldrich, Saint Louis, MO) was used as the surfactant for CNF dispersion. In a typical process, 100 mg CNFs and 200 mg PS4SS were mixed in 100 mL water by ultrasonication and magnetic stirring for 2 hrs at room temperature. The as-received CNFs suspension was poured onto a filter to remove the water with a vacuum to obtain a CNFs preform. The thickness of the preform can be tailored by changing of the amount of CNFs suspension. After drying at 120 ^{o}C for 8 hrs in vacuum, the CNFs preform was infiltrated by VL20 with 4 wt% of dicumyl peroxide (Acros Organics, Morris Plains, NJ) as the thermal initiator [17]. The infiltrated CNFs preform was solidified by heat-treatment at 100 ^{o}C for 24 hrs and then pyrolyzed at 1000 ^{o}C in N_2. For comparison, the monolithic SiCN ceramic were also prepared using the same conditions.

The pyrolysis behavior of the as-received infiltrated preform was characterized using thermal gravimetric analysis (TGA, SDT-Q600, TA Instruments, New Castle, DE). The density of both composites and the monolithic SiCN were measured using Archimedes' principle. The microstructures of the composites were observed using scanning electron microscopy (SEM, Zeiss ULTRA-55 FEG, Carl Zeiss SMT AG Company, Oberkochen, Germany).

The mechanical behavior of the nanocomposite and pure ceramic was tested using instrumented microindentation with Vickers indenter on a Micro-Combi Tester (CSM Instruments, Peseux, Switzerland). The test was carried out under the load-control mode with the indentation loads in the range of 1000 mN to 5000 mN. Prior to a full indentation, a pre-load of 5 mN was applied to the indenter in order to maintain intimate contact between the indenter and the surface of the sample and to avoid the effect of impact. Both the loading time and unloading time were set to be 30 s without intermediate holding at the peak indentation load. Five indents were made for each indentation load.

3. Results and Discussion

Figure 1a is an optical microscopy image of the prepared CNF preform, which is ~ 20 mm in length and ~ 1.5 mm in thickness. Figure 1b is a SEM image of the preform, showing the uniform dispersion of CNFs. The preforms were infiltrated with

VL20 under vacuum and cured at 100 ^{o}C to form precursor composites. Figure 1c shows a SEM image of the fracture surface of the precursor composite. It is seen that the CNFs are uniformly dispersed within the VL20 polymer matrix which contains no obvious pores/cracks.

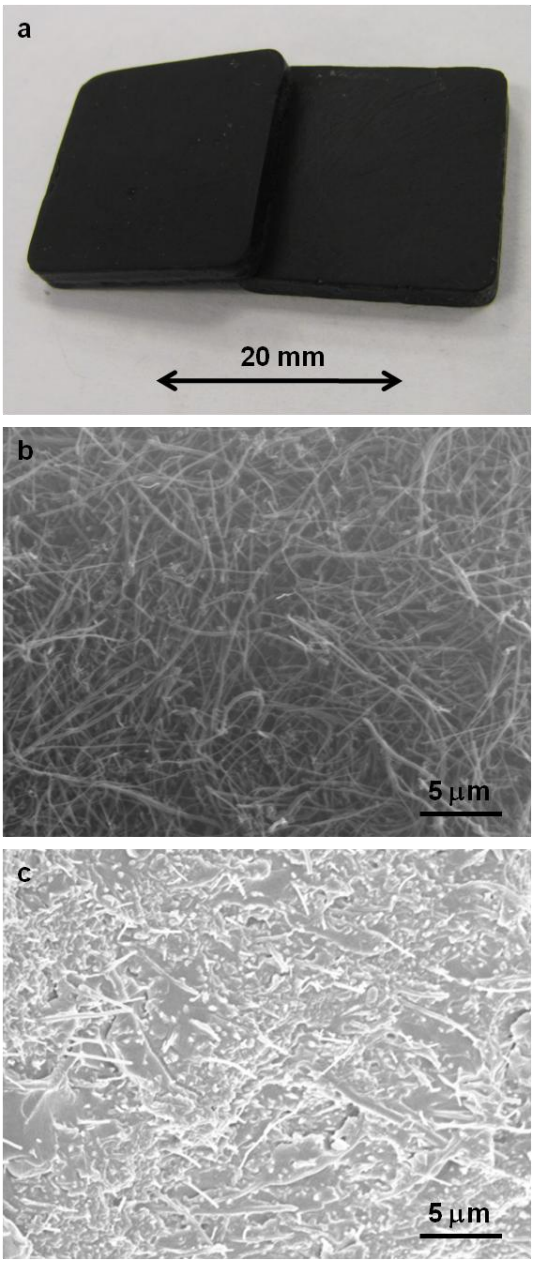

Figure 1: (a) Optical and (b) SEM images of the prepared CNF preform. (c) SEM image of the fracture surface of the infiltrated CNF preform.

The precursor composite was then pyrolyzed at 1000 ^{o}C in N_2. The pyrolysis caused ~ 20% weight loss and ~ 21% liner shrinkage which was similar along all directions, suggesting uniform shrinkage. We also found that pyrolysis of pure VL20, which formed amorphous silicon carbonitride (SiCN) with an apparent composition of $SiC_{0.99}N_{0.85}$ [17,18], had ~ 30% weight loss and 28 % linear shrinkage, similar to those previously reported [17,18]. The volume fraction, V_{CNF} of CNFs in the nanocomposite was calculated using the following equation:

$$V_{CNF} = \frac{w_{CNF}}{d_{CNF} V_{Comp}} \quad (1)$$

where w_{CNF} is the weight of the CNF preform; d_{CNF} is the density of the CNF, 1.95g/cm^3; and V_{Comp} is the volume of the ceramic nanocomposite measured by the Archimedes' principle. The result shows that the nanocomposite contained ~ 20 vol.% of carbon nanofibers. The above results suggest that CNFs exhibited little effect on the pyrolysis of VL20, which is likely due to that the CNFs within the preform can freely move relatively.

The microstructure of the obtained ceramic nanocomposite was analyzed using scanning electron microscopy. Figure 2a shows a SEM image of the polished surface of the nanocomposite. It is seen that the nanocomposite contains small amount of pores but no cracks, indicating the nanocomposite had a very dense structure. Further characterizing the fracture surface of the nanocomposite (Figure 2b) shows

that the carbon nanofibers are uniformly dispersed within the ceramic matrix, suggesting that the pyrolysis did not destroy the CNFs, neither disturb their distribution. The image also reveals substantial pullout of nanofibers from the ceramic matrix with the pullout length ranging from 1 to 5 micrometers. This result suggests that the nanocomposite may have good fracture toughness.

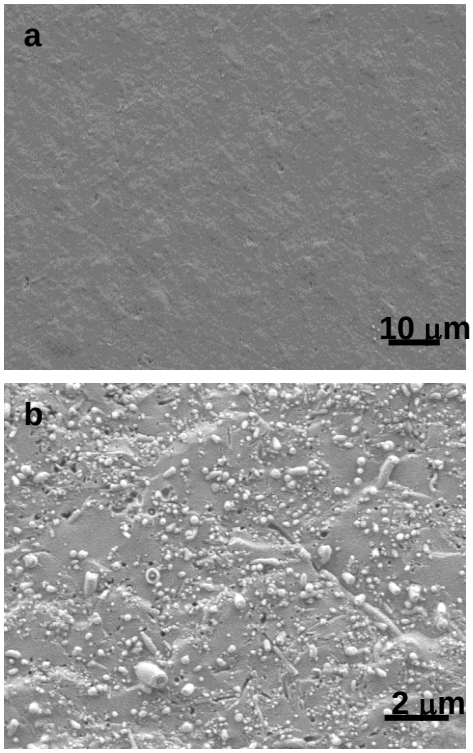

Figure 2: SEM images of (a) polished surface and (b) fracture surface of the ceramic nanocomposites.

Figure 3 shows typical indentation loading and unloading curves of the nanocomposite. The loading curves for different indentation loads overlap, suggesting that the loading rate has a negligible effect on the load–displacement relation. The microhardness, H_v, which is used to describe the plastic behavior of a material, is calculated as

$$H_v = \frac{1.85F}{d^2} \quad (2)$$

where d is the average diagonal length of the impression, and F is the indentation load. Using the measured diagonal lengths, one can calculate the microhardness by using Eq. (2). The variation of the microhardness of the nanocomposite with the indentation load is shown in Figure 4. For comparison, the corresponding microhardness of the monolithic SiCN is also included. The microhardness of the nanocomposite is 9.52 ± 0.86 GPa, which is less than 15.44 ± 0.97 GPa for the monolithic SiCN. This result suggests that the use of carbon nanofiber in SiCN caused softening in resisting local plastic deformation. It is known that CNFs have higher modulus in the axial direction, while they are very flexible in the transverse direction which provides less resistant to the deformation in the transverse direction. In general, it is impossible to make the CNF/SiCN nanocomposite with the CNFs' aligning in one direction by using the current technique. The CNFs form a fiber network with random distribution of the CNFs' direction. This is supported by the SEM micrograph (Figure 1b). The random distribution of the CNFs reduces the possible enhancement of the CNFs to the mechanical strength of the nanocomposite. In addition, the bonding strength between the CNFs and the SiCN matrix plays an important role in controlling the mechanical behavior of the CNF/SiCN nanocomposite. Quantitative assessment on the bonding strength is needed in order to understand the effect of CNFs on the mechanical strength of the nanocomposite and to interpret the microhardness behavior.

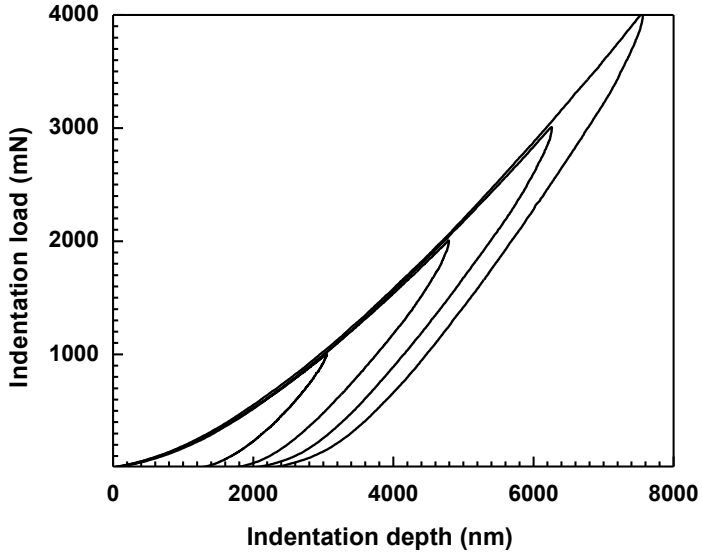

Figure 3: Typical indentation loading-unloading curves for the indentation of the 20% CNF/SiCN nanocomposite.

From the indentation loading-unloading curve, the total energy applied to the specimen, E_{total}, during the loading phase can be calculated as [19]

$$E_{total} = \int_0^{\delta_{max}} F d\delta \tag{3}$$

where δ_{max} is the indentation depth at the peak indentation load. The elastic recovery energy, $E_{elastic}$, can be calculated from the unloading phase as

$$E_{elastic} = \int_{\delta_r}^{\delta_{max}} F_{un} d\delta \tag{4}$$

where δ_r is the residual indentation depth and F_{un} is the indentation load for the unloading process. Thus the plastic energy dissipated in an indentation loading-unloading cycle, $E_{plastic}$, can be calculated from the total energy and the elastic recovery energy as

$$E_{plastic} = \int_0^{\delta_{max}} F d\delta - \int_{\delta_r}^{\delta_{max}} F_{un} d\delta \tag{5}$$

which represents the area enclosed by the indentation loading-unloading curve.

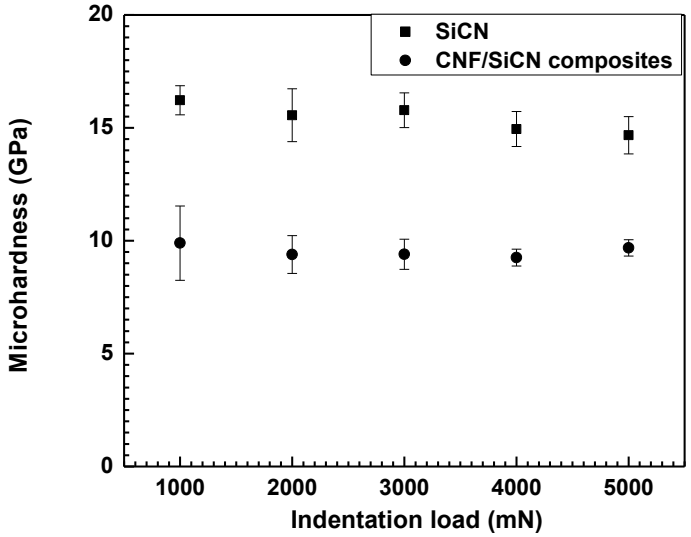

Figure 4: Variation of the microhardness with the indentation load.

Figure 5 shows the dependence of the dissipated plastic energy on the residual indentation load. It is seen that more energy is dissipated in the nanocomposite for the same indentation load. This is in accord with the low microhardness of the nanocomposite, which allows the indentation to produce more localized plastic deformation and absorb more external energy due to the small transverse compliance of CNFs. Using curve-fitting to fit the data points, one observes that the plastic energy is proportional to the 3/2 power of the indentation load, similar to the results for the indentation of aluminum [19, 20]. Even though the 3/2 power relation has been derived from the cavity model and dislocation mechanics for the indentation of crystalline metals [19], it is unclear why the indentation deformation of the monolithic SiCN and CNF/SiCN nanocomposite also followed the same relationship.

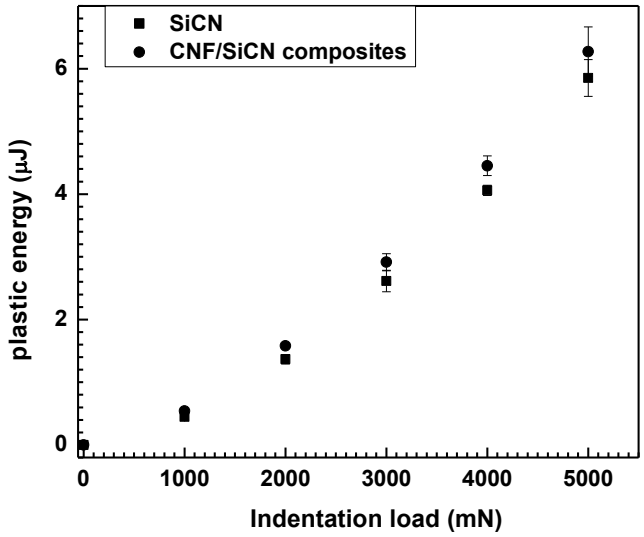

Figure 5: Dependence of the plastic energy dissipated in an indentation loading-unloading cycle on the indentation load.

Figure 6 shows the variation of the energy ratio, $E_{plastic} / E_{total}$, as a function of the indentation load for the monolithic SiCN and CNF/SiCN nanocomposite. The energy ratio decreases with the increase of the indentation load, suggesting that less portion of the indentation was dissipated in an indentation cycle for large indentation loads. For small indentation load, more portion of the indentation energy was dissipated in the nanocomposite than that in the monolithic SiCN. This implies that the CNF/SiCN nanocomposite has higher toughness for small indentation loads than the monolithic SiCN.

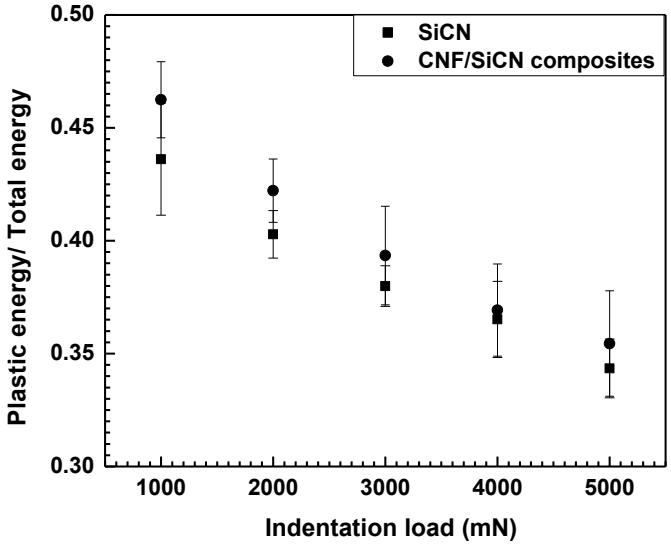

Figure 6: Dependence of the energy ratio, $E_{plastic} / E_{total}$, on the indentation load.

There are three obvious toughening mechanisms in the CNFs reinforced SiCN ceramic composites: CNFs bridging, CNFs pullout and crack branch, as shown in Figure 7. It is can be seen that an original crack source from the right hand side of Figure 7a caused a main crack growth. The main crack was branched to two sub-cracks. Furthermore, one of the sub-cracks was divided into other two sub-cracks. This is a clearly crack branch toughening mechanism, which will increase the toughness of the composites tremendously. The CNF bridging toughening mechanism is also observed in the composites as shown in Figure 7a. Another toughening mechanism of the CNFs pull out is coming out after the CNFs were broken shown in Figure 7b. If the bonding force between the CNFs and the ceramic matrix is less than the tensile strength of CNF, a debonding occurs at the interface of CNF and ceramic matrix. In result, the CNF pullout occurred at one side of the crack and left a hole in

the opposite side (Figure 2b). If the bonding force is larger than the tensile strength, the CNFs will be broken at the site of defects existed after the CNF bridging and both sides showed the CNF pullout, no holess appear. Defects and low tensile strength (compare to carbon nanotube) are the two main reasons of the short CNFs pullout length [16].

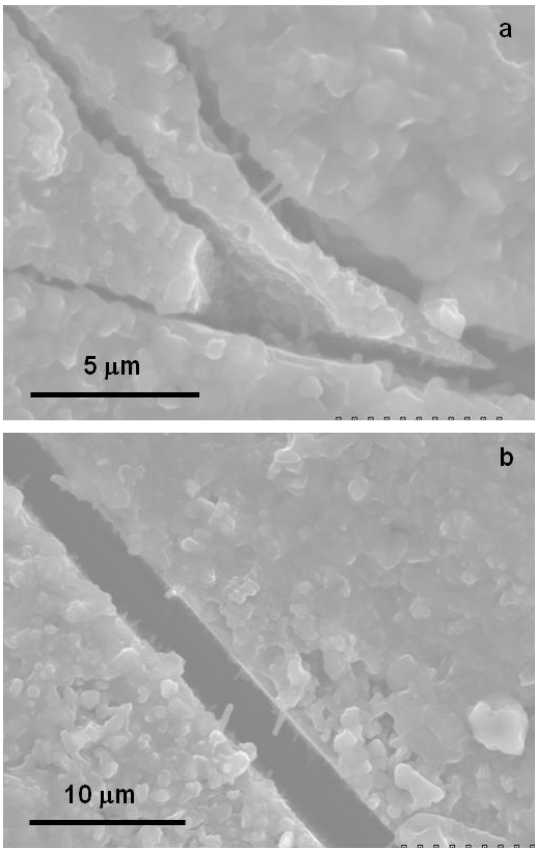

Figure 7: SEM images showing (a) CNF bridging and crack branch (b) CNFs pull out.

4. Summary

In this paper, we develop a simple and unique processing technique for making ceramic nanocomposites reinforced with high volume fraction of carbon nanofibers. In this technique, the CNFs are first made into a preform, which is then

infiltrated with liquid-phase polymeric preceramic precursor. The infiltrated preform is then pyrolyzed at 1000^{o}C to convert the precursor to silicon carbonitride ceramic. The obtained ceramic composite shows very high dense structure with small amount of pores, but no cracks. The mechanical behavior of the nanocomposite is characterized using instrumented microindentation. The results show that the hardness of the nanocomposites decreases as compared to the monolithic ceramic due to the flexibility of the carbon nanofibers. While the fracture energy of the nanocomposite increases as compared to the monolithic ceramic. The three toughening mechanisms are identified: CNFs bridging, CNFs pullout and crack branch. While the present work focuses on CNFs, the developed technique is suitable for other nano-scaled reinforcements.

References

1. M. Yu, O. Lourie, M.J. Dyer, K. Moloni, T. F. Kelly and R.S. Ruoff, ”Strength and breaking mechanism of multiwalled carbon nanotubes under tensile load,” *Science* 287, 637 (2000).
2. M. Yu, B.S. Files, S. Arepalli and R.S. Ruoff, “Tensile loading of ropes of single wall carbon nanotubes and their mechanical properties,” *Phys. Rev. Lett*. 84, 5552 (2000).
3. B.I. Yakobson, C.J. Brabec and J. Bernhole, “Nanomechanics of carbon tubes: instabilities beyond linear response,” *Phys. Rev. Lett*. 76, 2511 (1996).

4. G.V. Lier, C.V. Alsenoy, V.V. Doren and P. Geerlings, “Ab initio study of the elastic properties of single-walled carbon nanotubes and graphene,” *Chem. Phys. Lett.* 326, 181 (2000).
5. M.M.J. Treacy, T.W. Ebbesen and J.M. Gibson, “Exceptionally high Young’s modulus observed for individual carbon nanotubes,” *Nature (London)* 381, 678-80 (1996).
6. O. Lourie and H.D. Wagner, “Evaluation of Young's modulus of carbon nanotubes by micro-Raman spectroscopy,” *J. Mat. Res*. 13, 2418 (1998).
7. N. Hamada, S.I. Sawada and A. Oshiyama, “New one-dimensional conductors - graphitic microtubules,” *Phys. Rev. Lett*. 68, 1579 (1992).
8. H. Dai, J. Kong, C. Zhou, N. Franklin, T. Tombler, A. Cassell, S. Fan and M. Chapline, “Controlled chemical routes to nanotube architectures, physics, and devices,” *J. Phys. Chem. B* 103, 11246 (1996).
9. S. Berber, Y. Kwon and D. Tomanek, “Unusually high thermal conductivity of carbon nanotubes,” *Phys. Rev. Lett*. 84, 4613 (2000).
10. E.R. Wong, P.E. Sheehan and C.M. Lieber, “Nanobeam mechanics: elasticity, strength, and toughness of nanorods and nanotubes,” *Science,* 277[36], 1971-75 (1997).
11. R. Ma, J. Wu, B. Wei, J. Liang and D. Wu, “Processing and properties of carbon nanotubes-nano-SiC ceramic,” *J. Mat. Sci*. 33, 5243-46 (1998).

12. R.W. Siegel, S. Chang, B.J. Ash, J. Stone, P.M. Ajayan, R.W. Doremus and L.S. Schadler, "Mechanical behavior of polymer and ceramic matrix nanocomposites," *Scripta Mater*. 44, 2061-64 (2001).
13. G. Zhan, J.D. Kuntz, J. Wan and A.K. Mukherjee, "Single-wall carbon nanotubes as attractive toughening agents in alumina-based nanocomposites," *Nature Mat*. 2, 38 (2002).
14. A. Peigney, Ch. Laurent, O. Dumortier and A. Rousset, "Carbon nanotubes-Fe-alumina nanocomposites. Part I: Influence of the Fe content on the synthesis of powder," *J. Euro. Ceram. Soc*. 18, 1995-2004 (1998).
15. Ch. Laurent, A. Peigney, O. Dumortier and A. Rousset, "Carbon nanotubes-Fe-alumina nanocomposites. Part II: Microstructure and mechanical properties of the hot-pressed composites," *J. Euro. Ceram. Soc*. 18, 2005-13 (1998).
16. L. An, W. Xu, S. Rajagopalan, C. Wang, H. Wang, Y. Fan, L. Zhang, D. Jiang, J. Kapat, L. Chow, B. Guo, J. Liang and R. Vaidyanathan, "Carbon-nanotube-reinforced polymer-derived ceramic composites," *Adv. Mater.* 16, 2036-2040 (2004).
17. L. Bharadwaj, Y. Fan, L. Zhang, D. Jiang and L. An, "Oxidation behavior of a fully dense polymer-derived amorphous silicon carbonitride ceramic," *J. Am. Ceram. Soc.*, 87(3) 483-486 (2004).
18. A. Dhamne, W. Xu, B. Fookes, Y. Fan, L. Zhang, S. Burton, J. Hu, J. Ford and L. An, "Polymer-ceramic conversion of liquid polyaluminasilazanes for SiAlCN

ceramics," *J. Am. Ceram. Soc.*, 88[9], 2415-19 (2005).

19. F.Q. Yang, L.L. Peng and K. Okazaki, "Microindentation of aluminum," *Metallurgical and Materials Transactions A* 35, 3323-3328 (2004).
20. F.Q. Yang, L.L. Peng and K. Okazaki, "Microindentation of aluminum processed by equal channel angular extrusion," *J. Mater. Res.*19, 1243-1248 (2004).

APPENDIX- B: FABRICATION OF NANO-SCALED POLYMER DERIVED SIALCN CERAMIC COMPONENTS USING FOCUSED ION BEAM

Fully dense polymer-derived SiAlCN ceramics were synthesized from polysilazane as preceramic precursors followed by a thermal decomposition process. The nanofabrication of amorphous SiAlCN ceramics was implemented with a focused ion beam (FIB). FIB conditions such as the milling rate, the beam current, and the number of passes were considered. It was found that nanopatterns with a feature size of less than 100 nm could be fabricated onto polymer-derived ceramics (PDCs) precisely and quickly. Specific nanostructures of thin walls, nozzle, and gear have been fabricated as demonstrations that indicated the FIB technique was a promising method to realize nanostructures on PDCs, especially for microelectromechanical system (MEMS) and micro/nano sensor applications.

1. Introduction

Micro-sensors that can be operated in harsh environments are highly desired for gas turbines, nuclear reactors, space vehicles and many other high-temperature systems. Such sensors could be used to obtain useful information for monitoring the operation processes and the health of hot-section structural components, for improving the performance and safety of these systems. However, fabrication of such sensors faces a huge technical challenge. The major hurdle is that the sensors must survive harsh environments, including high temperatures, high stress, corrosive species and/or radiation. In addition, the sensor materials must maintain specific properties at high temperatures in order to provide means for sensing; and they must

do so in an easy-to-microfabricate way in order to lower costs. These requirements basically prevent the use of most available materials.

Recently, polymer-derived ceramics (PDCs) have been considered as suitable materials for making high-temperature microelectromechanical systems (MEMS)/micro-sensors.[1] Previous studies revealed that PDCs, synthesized from the thermal decomposition of polymeric precursors, exhibit excellent thermomechanical properties, such as high thermal stability,[2,3] high oxidation/corrosion resistance[4-8] and high temperature multifunctionalities.[9-12] In addition, the direct polymer-to-ceramic processing route of PDCs makes it much easier to be fabricated into various components/devices with complex shapes/structures. Several techniques have been developed for the fabrication of PDC-based MEMS and/or micro-sensors, such as microcasting, lithography, micromachining, and direct writing.[13-16] However, these techniques can only be used to fabricate micro-scaled components. Given the continuous demand for the downscaling of devices, it becomes crucially important to develop techniques that can make components/devices from PDCs in the nanometer scale.

In this paper, we report the fabrication of nanoscaled polymer-derived ceramic components by using a dual-beam focused ion beam (FIB). It has been demonstrated that FIB is a powerful tool for nanoscaled fabrications for many materials such as metal,[17] ferroelectrics,[18] quartz,[19] graphite,[20] polydimethylsiloxane,[21] glass fiber,[22] silicon, and germanium.[23] To the authors' knowledge, the use of FIB for

PDCs nanofabrication has not been reported yet. The FIB conditions, including the milling rate, the beam current, and the numbers of passes, were taken into account for precise and quick fabrication of PDCs on the nanoscale. The milling rate was calculated based on the beam dwell time and the number of passes, and the milling quality was monitored through a combination of scanning electron microscope (SEM). Several specific nanofeatures, including thin wall (s), nozzle, and gear, were demonstrated.

2. Experiments

In this study, polymer-derived amorphous silicoaluminum carbonitride (SiAlCN) ceramics were used as the model material for studying and demonstrating the feasibility of FIB-based nanofabrication of PDCs. Fully dense SiAlCN samples were synthesized using commercially available liquid phase polysilazane (HTT1800, Kion, Huntingdon Valley, PA) as the main precursor. Aluminum-tri-sec-butoxide (ASB, Sigma-Aldrich, St. Louis, MO) and poly (melamine-co-formaldehyde) acrylated solution (PVN, Sigma-Aldrich, St. Louis, MO) were used as the precursors for Al and N, respectively. Bis (2, 4, 6-trimethylbenzoyl)-phenylphosphineoxide (Irgacure 819, Ciba Specialty Chemicals Inc., Basal, Switzerland) was used as the photoinitiator. These starting chemicals were reacted together to form photocurable polyaluminasilazane using the following procedure. First, 7.8g HTT1800 and 1.0g

PVN were mixed together at 85^{o}C for 10 min under magnetic stirring. 0.5g ASB and 0.5g 819 were then added into the mixture by stirring for additional 30 min at the same temperature. The entire process was carried out using a standard Schlenk technique in an ultrahigh purity (UHP) N_2 environment instead of an atmosphere environment to decrease the likelihood of contamination. The resultant polyaluminasilazane was a clear, pale, yellow-colored liquid. The precursor was vacuumed for 60 minutes and photopolymerized under a UV light for 20 minutes. Afterwards, the SiAlCN ceramics were obtained by thermal decomposition set at 1000^{o}C for 4 hours in a tube furnace with the presence of UHP N_2 [24]. Finally, the finished SiAlCN ceramics were polished on one side using diamond paste with a particle size of 1 μm.

A dual-beam FIB instrument (FIB-SEM, Auriga series, Carl Zeiss) was employed to perform the nanofabrication of the SiAlCN ceramics. The instrument used a combination of SEM and FIB with two focused beams at a coincidence point. In addition to SEM imaging, the instrument could rapidly mill materials via ion sputtering or deposit material via chemical vapor deposition. The milling rate, beam current and number of passes are key FIB parameters to be considered in order to achieve the desired nanopatterns accurately and efficiently. The gallium ion energy was set to the standard 30 keV because the scattering effects were negligible in the cases described here. Depending on the nanopattern feature size, the beam spot diameter was controlled between 3 nm ~ 59 nm, which was achieved by varying the

beam current between 1 pA ~ 600 pA. The milling rates and the milling quality under different FIB conditions will be discussed in next section. Line scanning model and spiral scanning model were generally used on rectangular shapes and circular shapes, respectively. A 10 nm gold layer was coated onto SiAlCN ceramics in order to improve the conductivity and to provide superior resolution. The SEM mode was used to monitor the nanopattern features in situ with a 54 ° angle such that the feature size was measured with an angle compensation method.

3. Results and Discussion

The core principle of the FIB milling technology is to operate the FIB with the proper ion beam size and beam current to remove the required amount of material from a predefined location in a controllable manner to obtain high-precision structures. It is desired that the interaction between the incoming ions with the atoms near the target surface leads to a collision cascade, known as sputtering, of the atoms. During sputtering, a portion of the ejected atoms is frequently redeposited onto the sputtered region such that it is difficult to control the amount of material removed from sputtering. Both sputtering and redeposition are the governing effects in FIB milling efficiency and milling accuracy. In order to ensure the milling efficiency, the beam energy that is transferred from the ions to the target substrate should be high enough, which means that the beam current is critical to the sputtering yield. In order to ensure

the milling accuracy, controlling the number of passes is important to prevent severe redeposition.

To fully explore how the number of passes affects the milling quality (represented by the bottom slope) and milling rate, sample trapeziums were milled using different number of passes under the same FIB conditions. As shown in Figure 1 (a), (b), (c), and (d), the trapeziums were fabricated by the FIB using line scanning model from bottom to top with same area and total milling time but with different number of passes. The milled depth and bottom slope were calculated with an angle compensation method from these images, which were taken by the SEM with 54 °-tilt-view. It is found that the number of passes directly affected the milling rate and milling quality. It can be seen in Figure 1 (a) that there was a steep and rough bottom with a maximum depth of 1.97 μm at the end of the milling for 1 pass. It is believed that the material removed from the large milling depth was continuously redeposited at the milled region that resulted in the inclined and rough bottom. A flatter and smoother bottom with a small maximum milling depth of 0.53 μm was achieved when the number of passes increased to 4 as shown in Figure 1(b). The similar flat and smooth bottoms were observed with different maximum milling depth of 0.89 μm and 1.48 μm for 9 passes and 15 passes, as shown in Figure 1(c) and (d), respectively. It was found that a good milling quality can be achieved when there are no less than 4 passes. Therefore, 1 layer pass is suitable for high throughput milling that is less concerned about the quality of the bottom pattern. However, for high precision

milling of intricate patterns, the number of passes should preferably be no less than 4. It is noted that milling an inclined bottom is not always undesirable such that the number of passes can be used to adjust the bottom profile.

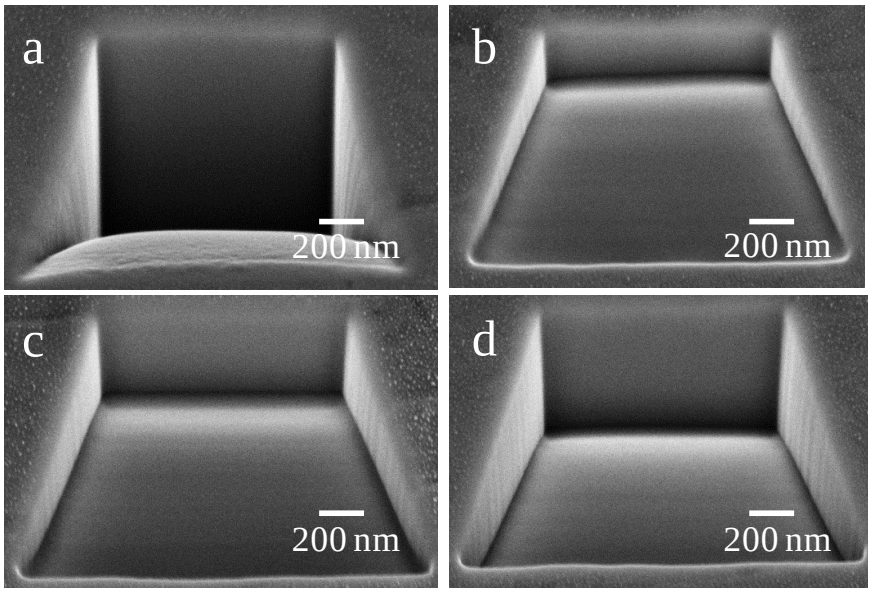

Figure 1: Typical trapeziums fabricated by FIB using different number of passes: (a) 1; (b) 4; (c) 9; (d) 15.

Another important parameter for FIB fabrication is milling rate, which can be calculated via dividing the milled volume by the ion beam current over the total milling time. In case of the trapezium fabrication, the milling area was 7.50 μm^2, the beam current and total milling time were 120 pA and 51 s, respectively, and the milling depth for the different number of passes were measured from the SEM images. The milling rates for the different number of passes were calculated based on the above parameters, shown in Figure 2. Figure 2 shows the trends of bottom slope and milling rate when the number of passes increased from 1 to 15. It can be seen that the milling rate decreased from 1.21 to 0.33 μm^3/nA s quickly when the number of passes

increased from 1 to 4, and continued to increase afterwards. The trend of the milling rate was nonlinear because removal of material in the milling process is mainly determined by both sputtering and redeposition, of which the effects behave nonlinearly when the number of passes is varied. Meanwhile, the bottom slope dramatically decreased from 0.65 to 0.18 corresponding to the number of passes from 1 to 4, and then kept at 0.18 afterwards which was similar to what was observed in Fig 1. The reason that the final slope was 0.18 and not 0 is due in large part to the alignment error from the substrate surface to the FIB aperture. We conclude that the number of passes should be no less than 4 in order to achieve sufficient milling quality, and the more passes that is undergone, the higher the milling rate. One thing should be mentioned here, there is a limit to the number of passes due to the minimum dwell time limit of each pixel for each pass, which means that for smaller feature sizes, they are limited by less number of passes.

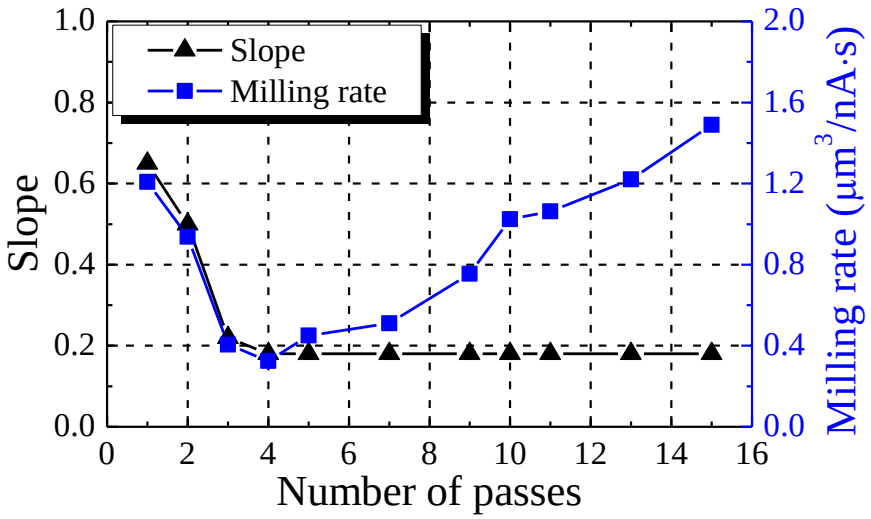

Figure 2: The trends of bottom slope and milling rate with different number of passes from 1 to 15.

The beam current must also be addressed because it is highly related to the milling quality and milling efficiency. A higher beam current is preferred for a higher milling rate. Nevertheless, higher beam current results in a coarser milled structure due to more debris being upheaved from the higher beam current and the larger beam spot diameter. Typically, beam currents at less than 5 pA are selected for high precision milling of nanoscale patterns, and beam currents at more than 600 pA are selected for high throughput milling of micro-scale patterns. The milling rates of the beam currents at 5 pA, 120 pA and 600 pA were measured with 1 pass, 4 passes, and 9 passes, as shown in Figure 3. With the same trend of the beam current at 120 pA, the milling rates of beam currents at 5 pA and 600 pA decreased first, and then increased when the number of passes increased from 4 to 9. The milling rate of the larger beam current was higher than the smaller beam current, but the differences were less than 30%, which indicated that the milling rates calculated before were valid and may be referred for future fabrication of various patterns.

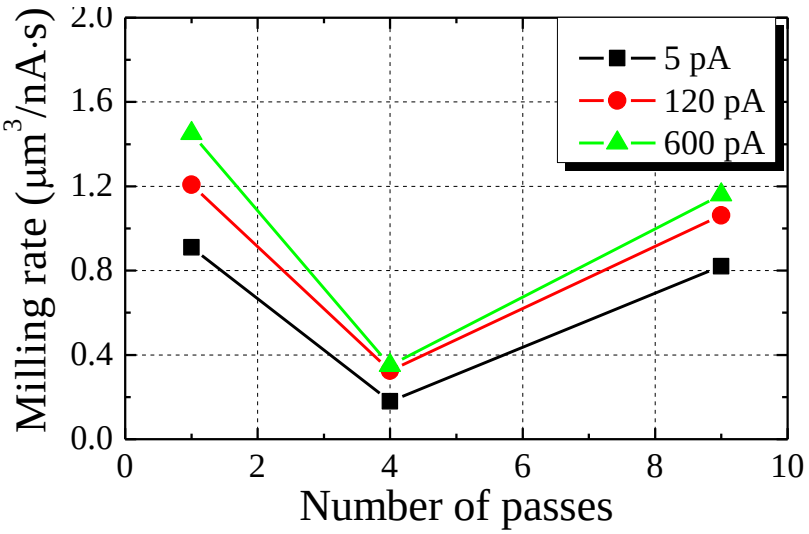

Figure 3: Comparison of milling rates by using different FIB beam currents.

Several specific nanostructures of thin wall(s), nozzle, and gear were fabricated onto SiAlCN ceramics using specially selected FIB conditions based on the feature size. The thin, nano-scaled wall structure was fabricated by milling two trapeziums to create a thin wall in between. The ion beam current of 600 pA with a corresponding beam spot diameter of 59 nm was used to roughly cut a thin wall, as shown in Figure 4(a). Since the bottom quality is less important in this case, the number of passes was set to 1 for high throughput. The thin wall dimension in Figure 4(a) was about 850 nm in width, 8.5 μm in length, and more than 2 μm in depth. Furthermore, a super-fine structure was achieved by precisely polishing the thin wall incrementally with a beam current of 120 pA and a beam spot diameter of 25 nm. The thickness of the thin wall was reduced to less than 100 nm, as shown in Figure 4(b). As a result, an extremely high aspect ratio (> 20) was achieved that indicated the process had great potential in nanosensor fabrication. A 1x13 thin wall array was fabricated using the similar method, as shown in Figure 5(a). The wall thicknesses and the spacing were between 200 nm ~ 350 nm. Figure 5(b) shows a close-up image of the array, where the widths of the two thin walls were 240 nm and 320 nm respectively.

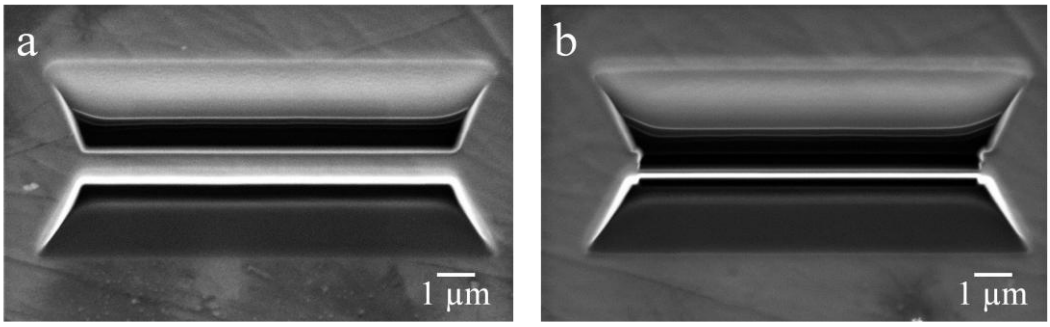

Figure 4: (a) Rough cut of a thin wall with the dimension of 850 nm in width, 8.5 µm in length, and more than 2 µm in depth; (b) Precise cut of a thin wall with the thickness less than 100nm.

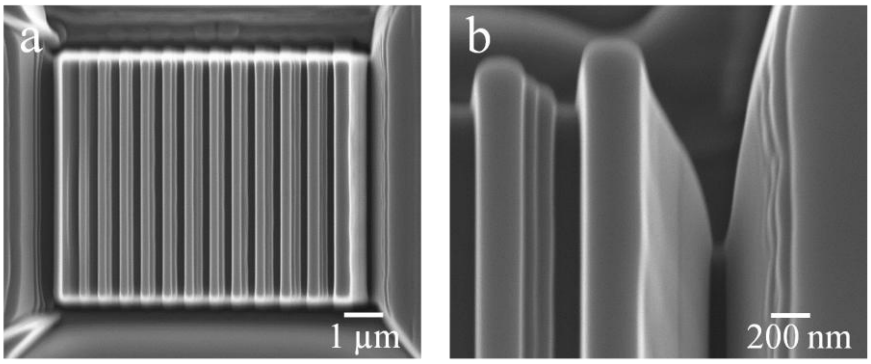

Figure 5: (a) Thin wall array; (b) Zoom-in thin wall array.

A nanonozzle was fabricated by using the spiral scanning model. As shown in Figure 6(a), a nozzle with a 900 nm inner diameter and a 2100 nm outer diameter was fabricated using a 600 pA beam current by milling away material to form a nozzle ring area. Accounting for a 54 ° observation angle, shown in Figure 2(a), the height can be calculated as 1.5 µm. A reverse nozzle with a 500 nm inside diameter and a 700 nm outside diameter was fabricated by using the same bitmap ring pattern and milling away the nozzle ring area, as shown in Figure 6(b). It can be seen that the patterns had an extremely smooth surface which affirmed the FIB technique as a good candidate for PDCs nanofabrication.

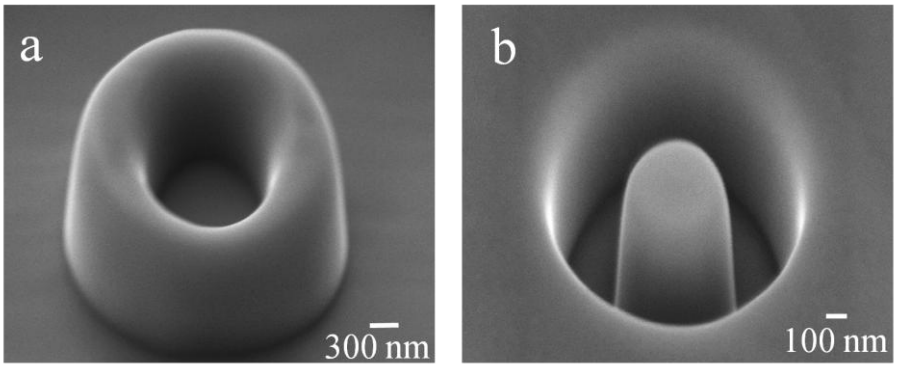

Figure 6: (a) Nano-nozzle observed at a 54 ºtilted angle; (b) Reversed nano-nozzle.

An intricate structure of a nanogear was fabricated to show the flexibility of FIB. Gear structures are a challenge from a fabrication point of view because it is a combination of circle wheel and rectangular teeth that are unlike a simple rectangular utilized in thin walls and simple circle utilized in nozzles, and especially for a FIB that is only capable to operate either the line scanning model or the spiral scanning model for each milling process. For this case, the line scanning model was used for each pattern scanning process due to the FIB limitation. The super-high FIB magnification was used to ensure the ion beam spot diameter was less than half of the bitmap pixel size in order to prevent discontinuity on the circle wheel surface. Figure 7(a) shows the fabricated nanogear with an extremely smooth surface and super accurate gear wheel of ~ 2.5 μm in diameter and gear teeth of ~ 300 nm in width. An even smaller feature size may be realized if a smaller beam current is applied instead of 600 pA in this case. Another nanopattern with an "UCF" (short of University of Central Florida) inscription was fabricated with a line width of less than 500 nm, as shown in Figure 7(b).

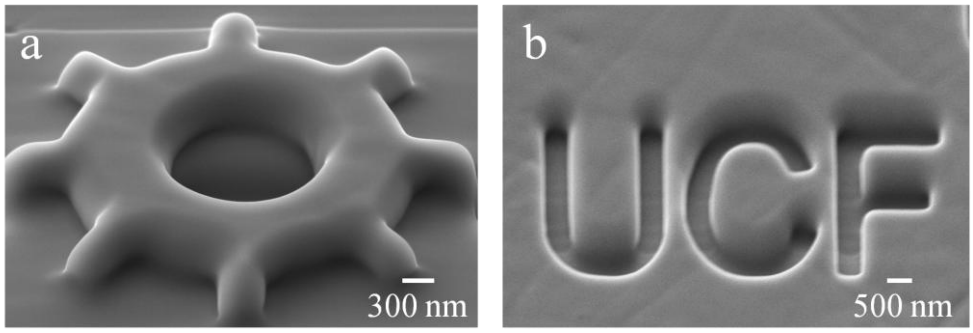

Figure 7: Intricate PDCs nanostructures. (a) Nano gear and (b) nano letters.

4. Conclusions

FIB technique was demonstrated as a promising fabrication method for PDCs on the nano scale and capable of extending existing applications, especially in MEMS and micro/nano-sensor field. FIB conditions including the milling rate, the beam current, and the number of passes were expressly selected for precise and efficient nanofabrication of PDCs. A good milling quality was achieved by controlling the number of passes to no less than 4, and the milling rate was observed to decrease first in 1 to 4 passes and then continually increase afterward. The observed milling rates under different FIB conditions may serve as reference for further fabrication of various nanostructures on PDCs. The milling quality of various concave and convex nanostructures was also illustrated. Several intricate PDC nanostructures such as thin wall(s), nozzle, and gear were demonstrated. The feature size of nano-patterns may be fabricated to less than 100 nm with an extremely smooth surface and super-high accuracy.

Acknowledgements

The authors would like to thank the funding support from National Science Foundation (MRI-R2: 0960022 and CMMI-0927441). The authors also appreciate Mr. Christopher Santeufemio at the Campus Materials Characterization Laboratory (CMCL) in the University of Massachusetts Lowell (UML) for his technical support of using FIB.

References

1. L. Liew, W. Zhang, V. M. Bright, L. An, M. L. Dunn, and R. Raj, "Fabrication of SiCN Ceramic MEMS Using Injectable Polymer-Precursor Technique," Sensors Actuators: A. Phys., 89 (1-2) 64-70 (2001).

2. R. Riedel, A. Kienzle, W. Dressler, L. Ruwisch, J. Bill, and F. Aldinger, "A Silicoboron Carbonitride Ceramic Stable to 2000C," Nature, 382, 796-8 (1996).

3. Z. C. Wang, F. Aldinger, and R. Riedel, "Novel Silicon-Boron-Carbon-Nitrogen Materials Thermally Stable up to 2200^{o}C," J. Am. Ceram. Soc., 84, 2179-83 (2001).

4. L. An, Y. Wang, L. Bharadwaj, Y. Fan, L. Zhang, D. Jiang, Y. Sohn, V. Desai, J. Kapat and L. Chow. Silicoaluminum carbonitride with anomalously high resistance to oxidation and hot corrosion. Adv. Eng. Mater., 6[5], 337-40 (2004).

5. Y. Wang, Y. Fan, L. Zhang, W. Zhang, and L. An, “Polymer-Derived SiAlCN Ceramics Resist Oxidation at 1400^{o}C,” Scr. Mater., 55, 295-7(2006).

6. Y. G. Wang, L. An, Y. Fan and L. G. Zhang, S. Burton, Z. H. Gan, “Oxidation of Polymer-Derived SiAlCN Ceramics,” J. Am. Ceram. Soc., 88 (11) 3075-3080 (2005).

7. Y. Wang, W. Fei, Y. Fan, L. Zhang, W. Zhang and L. An. A silicoaluminum carbonitride ceramic resist oxidation/corrosion in water vapor. J. Mater. Res., 21[7], 1625-1628 (2006).

8. L. Bharadwaj, Y. Fan, L. Zhang, D. Jiang and L. An. Oxidation behavior of a fully dense polymer-derived amorphous silicon carbonitride ceramic. J. Am. Ceram. Soc., 87(3) 483-486 (2004).

9. L. Zhang, Y. Wang, Y. Wei, W. Xu, D. Fang, L. Zhai, K. Lin, and L. An, “A Silicon Carbonitride Ceramic with Anomalously High Piezoresistivity,” J. Am. Ceram. Soc., 91, 1346-9 (2008).

10. P.A. Ramakrishnan, Y.T. Wang, D. Balzar, L. An, C. Haluschka, R. Riedel and A. Herman. Silicoboron-carbonitride ceramics: A class of high-temperature, dopable electronic materials. Appl. Phys. Lett., 78[20], 3076-78 (2001).

11. Hee- Yeon Ryu, Qi Wang and Rishi Raj. Ultrahigh-temperature semiconductors made from polymer-derived ceramics. Journal of the American ceramic society, vol. 93, no. 6, pp. 1668-1676, 2010.

12. K. Terauds, P. E. Sanchez-Jimenez, R. Raj, C. Vakifahmetoglu, P. Colombo. Giant piezoresistivity of polymer-derived ceramics at high temperatures. Journal of the European Ceramic Society, vol. 30, no. 11,pp. 2203-2207, 2010.

13. L. A. Liew, Y. Liu, R. Luo *et al.*, "Fabrication of SiCN MEMS by photopolymerization of pre-ceramic polymer," Sensors and Actuators A: Physical, vol. 95, no. 2–3, pp. 120-134, 2002.

14. L. Liew, W. Zhang, L. An *et al.*, "Ceramic MEMS new materials, innovative processing and future applications," American Ceramic Society bulletin. pp. 25-30, 2001.

15. Y. Liu, L. A. Liew, R. Luo *et al.*, "Application of microforging to SiCN MEMS fabrication," Sensors and Actuators A: Physical, vol. 95, no. 2, pp. 143-151, 2002.

16. H. Duan, C. Li, W. Yang, B. Lojewski, L. An and W. Deng. Near-field electrospray printing of polymer-derived ceramics for micro-sensor applications. Journal of Microelectromechanical Systems, accepted.

17. L. Ying-Yi, L. Jiunn-Der, J. Yu-Hung *et al.*, "Focused ion beam-fabricated Au micro/nanostructures used as a surface enhanced Raman scattering-active substrate for trace detection of molecules and influenza virus," Nanotechnology, vol. 22, no. 18, pp. 185308, 2011.

18. R. Vanga, X. Huang, and Z. Zhou, "Focused ion beam fabricated bragg grating filters in relaxor ferroelectrics," Nuclear Instruments and Methods in Physics

Research Section B: Beam Interactions with Materials and Atoms, vol. In Press, Corrected Proof, 2011.

19. L. D. Menard, and J. M. Ramsey, "Fabrication of Sub-5 nm Nanochannels in Insulating Substrates Using Focused Ion Beam Milling," Nano Letters, vol. 11, no. 2, pp. 512-517, 2011.

20. G. Venugopal, M.-H. Jung, M. Suemitsu *et al.*, "Fabrication of nanoscale three-dimensional graphite stacked-junctions by focused-ion-beam and observation of anomalous transport characteristics," Carbon, vol. 49, no. 8, pp. 2766-2772.

21. G. Li, and et al., "The nanofabrication of polydimethylsiloxane using a focused ion beam," Nanotechnology, vol. 20, no. 14, pp. 145301, 2009.

22. C. Victor, and et al., "Optimized fabrication of curved surfaces by a FIB for direct focusing with glass fibres," Journal of Micromechanics and Microengineering, vol. 19, no. 10, pp. 107003, 2009.

23. K. Miroslav, and et al., "Low energy focused ion beam milling of silicon and germanium nanostructures," Nanotechnology, vol. 22, no. 10, pp. 105304, 2011.

24. A. Dhamne, W. Xu, B. Fookes, Y. Fan, L. Zhang, S. Burton, J. Hu, J. Ford and L. An. Polymer-ceramic conversion of liquid polyaluminasilazanes for SiAlCN ceramics. J. Am. Ceram. Soc., 88[9], 2415-19 (2005).